2016

Enhancing Osseointegration of Orthopaedic Implants with Titania Nanotube Surfaces

Erin A. Baker
Michigan Technological University, eaburns@mtu.edu

ENHANCING OSSEOINTEGRATION OF ORTHOPAEDIC IMPLANTS WITH TITANIA NANOTUBE SURFACES

By

Erin A. Baker

A DISSERTATION

Submitted in partial fulfillment of the requirements for the degree of

DOCTOR OF PHILOSOPHY

In Mechanical Engineering-Engineering Mechanics

MICHIGAN TECHNOLOGICAL UNIVERSITY

2016

This dissertation has been approved in partial fulfillment of the requirements for the Degree of DOCTOR OF PHILOSOPHY in Mechanical Engineering-Engineering Mechanics.

Department of Mechanical Engineering-Engineering Mechanics

Dissertation Advisor: *Craig Friedrich, Ph.D., P.E.*

Committee Member: *Paul Fortin, M.D.*

Committee Member: *Gregory Odegard, Ph.D.*

Committee Member: *Tolou Shokuhfar, Ph.D.*

Department Chair: *William Predebon, PhD*

To my sons—
Everett Charles, Miles Anden and Hadden Stuart

Table of Contents

List of Figures

List of Tables

Preface

A substantial portion of this document contains text that is planned for journal submission. Text, figures, and tables from Chapters 1, 3, 4, and 5 have been compiled in a manuscript focused on *in vitro* and *in vivo* biocompatibility of titania nanotube surfaces. A separate manuscript focused on the *in vitro* and *in vivo* osseointegrative potential of titania nanotube surfaces was prepared from text, figures, and tables presented in Chapters 1, 3, 4, and 6. Selected text from Chapter 7, regarding local delivery of stromal cell-derived factor 1 (SDF-1β) via titania nanotube surfaces, was used in a previous grant submission, and will likely be used, in part, for a future manuscript submission. There were numerous co-authors on these two manuscripts. Their names and contributions, in alphabetical order, are:

Erin Baker, MS — PhD Candidate and Research Engineer in the Beaumont Research Laboratory, who planned as well as performed or assisted with all (three) experiments (one *in vitro*, two *in vivo*), including all characterization techniques, to assess two titania nanotube surface morphologies. "Planning" included the following activities: selection of number/type of samples (for each experiment) and characterization techniques, sample randomization, budget preparation, selection and follow-up correspondence with three off-site vendors, and preparation/submission/ maintenance IACUC protocol at both Beaumont and MTU. Erin was actively involved with data collection for all characterization techniques, except ICP-MS which was performed at an off-site vendor. Following experimentation and data collection, Erin analyzed all results, and

subsequently prepared abstracts and manuscripts. Regarding the future work section, Erin prepared a grant submission and subsequently received a Beaumont Health Seed Grant.

Kevin Baker, PhD — Research Engineer Scientist in the Beaumont Orthopaedic Research Laboratory, who assisted with all histologic grading. Kevin has experience (coursework and publications) with grading undecalcified histology, and taught the grading techniques, reviewed grading results, and assisted with the histologic methods and results portions of both manuscripts. He also assisted with study designs.

Mackenzie Fleischer, BS — Biologist and Research Assistant in the Beaumont Orthopaedic Research Laboratory, who assisted as a surgical assistant (dispensed wires, obtained radiographs) during all surgical procedures for both *in vivo* studies. Mackenzie also assisted with all endpoint dissections and biomechanical testing.

Paul Fortin, MD — Orthopaedic surgeon and member of PhD committee, who guided the *in vivo* studies with respect to surgical technique and postoperative care. Dr. Fortin also assisted with the surgical methods portion of both manuscripts.

Craig Friedrich, PhD — Full Professor and PhD advisor, who guided all research experimentation. Dr. Friedrich also prepared samples for *in vitro* and *in vivo* analyses as well as assisted with the sample fabrication methods portion of both manuscripts.

Meagan Salisbury, MS — Research Engineer in the Beaumont Orthopaedic Research Laboratory, who supported all *in vitro* work. Meagan also assisted with the *in vitro* studies-related methods portion of both manuscripts.

Tolou Shokuhfar, PhD — Associate Professor and member of PhD committee, who previously worked with Dr. Friedrich and developed the two titania nanotube morphologies analyzed in the *in vitro* and *in vivo* experiments.

Alexander Vara, MD — Orthopaedic resident, who performed all surgical procedures for both *in vivo* studies. Dr. Vara also assisted with the surgical methods portion of both manuscripts.

Acknowledgments

The process, and ultimately culmination, of this degree would not have been achieved without the encouragement, collaboration, and assistance of many people.

First and foremost, I would like to thank my advisor, Dr. Craig Friedrich, for his support and advocation of this research and my academic studies, especially with a 500-mile differential. I would be remiss if I did not also thank him for his patience and consideration, as he weathered my "life balance", including several surgeries and the birth of my third son. After mentoring me through a Masters program and now a Doctorate, I know that you are truly a model of professional integrity and success, and I hope to model my career accordingly. I have also appreciated your seasoned, longitudinal reports regarding parenting.

To my committee members, Drs. Fortin, Odegard, and Shokuhfar, I appreciate your dedication and commitment to my overseeing my research work. Specifically, Dr. Fortin, I appreciate your excellent, always timely feedback as well as guidance and training regarding surgical technique, despite your extremely busy clinical schedule. You always brought the experiments into a clinical focus, which was so crucial as we moved from *in vitro* to *in vivo* applications. Dr. Odegard, I was fortunate to be in your inaugural Continuum Mechanics course. I was and am so inspired by your teaching techniques. Dr. Shokuhfar, your excitement and motivation of this research platform has been infectious, and I appreciate your essential communication of experimental methods and results. The research would not have advanced in these new, exciting directions without your support.

I would also like to express my gratitude to the Department of Orthopaedic Surgery, especially former and current department chairmen, Drs. Harry N. Herkowitz

and Jeffrey Fischgrund, respectively. When returning to school was just a concept, Dr. Herkowitz was tremendously supportive. Prior to and since his passing three years ago, he has been a motivating influence. I often hear his declarations as I work through the evenings and early mornings on data analysis and writing—"Just get it done!" and "Was everything done appropriately?" He developed our department's research program, while setting the benchmark for high-quality, clinically-relevant work. I can only hope I am carrying that legacy "appropriately." To Dr. Fischgrund, thank you for continuing the department's commitment to my degree program and research. Without your support, guidance, and dedication, our laboratory may have imploded, but we are now on stable ground and fortunate to explore the intricacies of orthopaedic surgery, from bench to bedside. Thanks also to all of the surgeons in the department that have provided their support. Specifically, my gratitude to Dr. Rachel Rohde, who provides amazing examples of consistent achievement and professionalism.

An enormous "thank you" to my Beaumont Orthopaedic Research Laboratory colleagues. Thanks especially to Mackenzie Fleischer for your detailed documentation while assisting on all of the surgeries. I also appreciate the additional assistance with dissections and mechanical testing. Thanks also to Meagan Salisbury for your guidance and assistance with the *in vitro* experiments, Michael Newton and Dr. Tristan Maerz for providing guidance and training on the microcomputed tomography imaging techniques and data analysis tools as well as Richard Roberts for providing assistance with biomechanical fixture design and machining. I am also grateful for the diligent work, enduring support, and field knowledge of our Research Services team, especially Michele McGonagle, Essie Morrison, and Heather Brzezinski.

Finally, a massive debt of gratitude to my family and close friends. To Patricia and Richard Burns, my Mom and Dad, you always told me I could be anything, but that it started with a college degree. Without your unconditional love, sacrifices, and support, I would never have accomplished anything at all. I am so lucky to have you as my greatest role models in life. To Patricia and Richard Baker, my second Mom and Dad and in-laws, thank you so much for welcoming me into the family as well as all of your support over the last 11 years through my Masters, working, and now this degree program. I have always appreciated your honesty, hospitality, and work ethic. To all of my parents, thank you for being our "village" that has assisted with everything imaginable, including helping to raise our boys, working on our house, providing work accommodations and respite on the "East side", and much more. To my siblings—Meghan and Sean—we will always have an implicit devotion to one another. I love you both and am so proud of everything you've accomplished. And, Beth Podleski, my very best friend that I met at MTU 15 years ago, you are first class. These years of friendship have been such a exciting ride. Distance may separate us, but we will always be bonded.

Most importantly, to my husband, Kevin, thanks for being my ultimate teammate in work and life. Words cannot ever or adequately describe how important your friendship, conversation, love and support have been on this journey. I appreciate every single day. And, to my boys—Everett, Miles, and Hadden—you are the absolute joy in my life. Our little family is my most favorite thing Being in school together over the last few years has provided an interesting perspective, and I'm thrilled that we can all celebrate "graduations" this year. I will *always* be there for you, in any and every context, and look forward to your chapters unfolding.

Abstract

Introduction: As joint arthroplasty surgical procedures increase annually, the development of new strategies, including novel materials and surface modifications, to attain solid bone-implant fixation are needed to increase implant terms of service. In this study, we evaluate two morphologies of titania nanotubes in both *in vitro* and *in vivo* experiments to quantify osseointegrative potential and material-level biocompatibility.

Materials and Methods: Samples were prepared via an electrochemical etching process. Two different titania nanotube (TiNT) morphologies were produced, Aligned and Trabecular. For the *in vitro* experiment, Sprague Dawley (SD) rat marrow-derived bone marrow cells (BMC) were seeded on samples. Alkaline phosphatase (ALP) activity, osteocalcin (OC) expression, expression of relevant genes as well as cell attachment and morphology were assessed. In the first *in vivo* experiment, Kirschner wires were implanted unilaterally into SD rat femora with a TiNT-etched or unmodified (Control) implant. General health assessments and weekly body weights were recorded. At a 12-week endpoint, hematologic, systemic metal ion, and histologic analyses were performed. For the second *in vivo* experiment, Kirschner wires were implanted bilaterally into SD rat femora, with a TiNT-etched implant in one femora and unmodified (Control) implant as an internal control. At 4- and 12-week endpoints, femora were assessed via biomechanics, undecalcified histology, micro-computed tomography (μCT), and backscattered electron imaging (BEI) to characterize *de novo* bone formation.

Results: *In vitro* experiments demonstrated BMC attachment and differentiation into osteoblasts as well as greater ALP activity, OC expression, total cell counts, and gene expression (of Col1a1, IGF-1, and osteonectin) on TiNT surfaces versus Controls. Cells on TiNT-etched substrates were smaller in diameter and more eccentric than Controls. In the first *in vivo* experiment, there were significant differences in body weight between groups at Weeks 9 and 11. There were no significant differences in red or white blood cell function between TiNT groups and Control. Aluminum levels in the lungs were significantly greater in the Trabecular TiNT group compared to Control. Histologic analysis showed significantly fewer granulocytes and neutrophils in the distal region of Trabecular TiNT-implanted femora as well as significantly fewer foreign body giant/multinucleated cells and neutrophils in the midshaft region of Aligned TiNT-implanted femora versus Controls. In the second *in vivo* experiment, at 12 weeks, μCT analysis showed TiNT implants generated greater bone formation than Controls. Histologic analysis demonstrated 1.5 times greater bone-implant contact in TiNT groups than Controls at 12 weeks. TiNT groups exhibited 1.3 to 3.7 times greater strength of fixation than Controls during pull-out testing.

Discussion and Conclusions: *In vitro* data confirmed BMC attachment and differentiation into osteoblasts as well as osteoblastic phenotypic behavior. A clinically-relevant *in vivo* model of femoral intramedullary fixation, showed increased bone formation and quality in femora implanted with TiNT-etched implants versus Controls. A second *in vivo* study showed that TiNT surfaces do not generate systemic effects and may beneficially modulate the periprosthetic inflammatory environment.

Chapter 1:

Introduction

This work builds on the body of work of former and current researchers within the Multi-Scale Technologies Institute (MuSTI) group investigating titania nanotube (TiNT) arrays for biomedical applications. In this paper, orthopaedic applications of the material will be examined and discussed.

The total number of joint arthroplasty surgical procedures continues to increase year over year due to a confluence of factors, including population aging, obesity, increasing rates of arthritis, and bone metabolic disorders.[1-3] For implants requiring bony fixation, efficient, early-term osseointegration as well as a stable bone-implant interface are early indicators of clinical success. Long-term, implant performance, especially related to wear behavior, is one key factor in determining need for a revision procedure. Poor osseointegration may lead to implant subsidence and/or malalignment, which results in altered joint kinematics and accelerated wear and damage to components. Additionally, surface treatments and coatings applied to orthopaedic implants may dislodge during implantation or cyclic loading, leading to third-body wear and eventually the need for early revision surgery.

TiNT surfaces may provide both early- and long-term improvements in osseointegration as a result of increased osteoblast attachment and bone mineralization. Long-term implant performance may also be achieved via a reduction in TiNT particle shedding and a diminished inflammatory response to TiNT surfaces and debris compared

Material contained in this chapter is planned for journal submission.

to other orthopaedic implant materials.

The goal of the proposed experimentation discussed in this document, was to assess the osteoconductive and biocompatibility properties of Aligned and Trabecular TiNT surfaces via both *in vitro* and *in vivo* experimentation. Chapters 2 and 3 provide additional background about the principles of bone formation, orthopaedic implants, and TiNT surfaces. Specifically, Chapter 2 provides an overview of the process of bone tissue formation and cycle of regeneration, current orthopaedic implant technologies, and material-level requirements of metal alloys. Chapter 3 introduces TiNT surfaces, including advantages of the surface modification techniques and material processing.

In Chapter 4, preliminary *in vitro* experimentation performed to characterize the cellular response and behavior on TiNT surfaces, providing information regarding baseline biocompatibility with respect to cell survivability are described. Osteoblastic differentiation of marrow-derived stem cells cultured on TiNT surfaces was assessed by assaying osteogenic markers at both the protein- and mRNA-level, in order to generate information about TiNT performance in an environment simulating a marrow cavity.

Chapters 5 and 6 detail the translation of our *in vitro* results into *in vivo* models. *In vivo* biocompatibility was evaluated by assessing longitudinal animal weights, remote organ weights, metal ion levels in remote organs and whole blood, hematology, and undecalcified histology (Chapter 5). The ability of Aligned and Trabecular TiNT-modified implant surfaces to facilitate *in vivo* bone ingrowth and ongrowth was investigated in a rat femoral intramedullary implant model, using a combination of

biomechanics, undecalcified histology, microcomputed tomography (μCT) and backscattered electron imaging (BEI) characterization techniques (Chapter 6).

Three concepts of future directions for continued evaluation and modification of titania nanotube surfaces are presented in Chapter 7. The first concept focuses on local delivery of stromal cell-derived factor 1 (SDF-1β), which increases recruitment of stem cells that will subsequently stimulate bone formation, from titania nanotube surfaces. Second, a murine air pouch model of wear debris-induced osteolysis is proposed, to compare titania nanotube and conventional wear debris. Finally, a model of total hip arthroplasty in a goat is described, which will fulfill the prerequisite of *in vivo* testing in a higher phylogenic species, as required by the United States Food and Drug Administration.

Chapter 8 contains the conclusions of the experimentation and results presented in this document, based on our initial hypotheses that TiNT surfaces provide both early- and long-term improvements in osseointegration-related outcomes as a result of increased osteoblast attachment and bone mineralization as well as equivalent biocompatibility and toxicity, compared to unmodified titanium alloy surfaces.

Chapter 2:

Specific Considerations of Orthopaedic Implants for Osseointegration Applications

2.1 Introduction

In 2010, 719,000 primary total knee arthroplasty and 332,000 total hip arthroplasty (THA) surgeries were performed, according to the National Hospital Discharge Survey prepared by the Centers for Disease Control and Prevention.[4] Solid biologic fixation at the bone-implant interface provides long-term stability of arthroplasty and other orthopaedic implant components that require osseointegration. Poor osseointegration may lead to implant subsidence and/or malalignment, resulting in altered joint kinematics and accelerated wear and damage to components.

2.2 Bone Formation for Ingrowth and Ongrowth of Orthopaedic Implants

Bone is a multifaceted organ composed of osseous, nervous, fibrous, muscle, and epithelial tissues.[5] The 206-bone adult human skeletal system has various roles, including structural support of soft tissues and musculature, protection of delicate organs (e.g. brain, heart, uterus), sites of attachment for muscles and subsequent crosstalk, regulation of calcium and phosphorus levels as a dynamic reservoir as well as collection and quarantine of toxic materials (e.g. lead).[6-9]

Compared to other tissues in the body, bone tissue is less cellular. Bone is formed by a combination of several types of extracellular matrices, including mineralized bone extracellular matrix (ECM) as well as unmineralized osteoid and lacunar ECM. Primarily composed of mineralized bone ECM produced by osteoblast cells and considered a

composite material, bone tissue has many constituents, including minerals (e.g. magnesium, sodium), protein, water, salts (e.g. insoluble calcium and phosphorus as hydroxyapatite), lipids, glycoproteins, and proteoglycans. Osteoid and lacunar extracellular matrices also have important roles in bone tissue production and maintenance. Osteoid is unmineralized tissue that forms a temporary matrix, defining the regions that will eventually mineralize to form mature bone. The role of the unmineralized lacunar ECM, which surrounds osteocyte cells, is also related to regulating osteocyte function.[10]

There are two distinct structures of bone tissue, trabecular and cortical, which are formed through primary (woven) and secondary (lamellar) tissue organization. Trabecular bone has a sponge-like appearance with macroscale porosity. The most distinguishing characteristic of trabecular bone structure is the system of flat, thin plates and cylindrical rods that serve as mechanical struts. These struts are an indicator of bone disease, quality and overall health. In metabolic disease processes, such as osteoporosis, as strut thickness decreases, subsequently strut interconnectivity decreases and porosity increases, resulting in decreased mechanical strength and support. Bone marrow fills the negative space surrounding the struts. Located at the proximal and distal regions of long bones, trabecular bone effectively absorbs impact forces near joints. In contrast, cortical bone is extremely dense and compacted. Cortical bone surrounds the long bones. In the diaphyseal (midshaft), the cylindrical region of a long bone, cortical bone supports weight-/load-bearing and surrounds the intramedullary canal. Moving proximally or distally, the thickness of the cortical bone decreases in the metaphyses and epiphyses, forming a thin shell. Because these regions contain a significant amount of trabecular

bone, the cortical and trabecular bone effectively load-share, with the evenly-dispersed trabecular bone enduring most of the mechanical force.[10]

In total hip arthroplasty, the process of bone formation and subsequent osseointegration begin at the time of implantation with a process of injury and repair. During repair, intramembranous bone formation occurs at the bone-implant interface, which leads to osseointegration depending on implant material, implant surface morphology (e.g. pore size, surface chemistry), implant stability, and bony apposition.[10] In intramedullary canals, implants are in contact with bone marrow, containing stem and progenitor cell populations. The stem cell populations include hematopoietic stem cells (HSC) and nonhematopoietic mesenchymal stem cells (MSC). HSC may shift into various immune cell types, including erythrocytes (red blood cells), granulocytes (i.e. basophils, neutrophils, eosinophils, monocytes), and lymphocytes (i.e. dendritic cells, plasma cells, T cells, B cells, T natural killer cells).[11] Conversely, MSC may differentiate toward multiple mesodermal tissue lineages, including bone (i.e. osteoblast), muscle (i.e. myocyte), cartilage (i.e. chondrocyte), tendon or ligament (i.e. fibroblast), and adipose (i.e. adipocyte).[12-16] If conditions (e.g. implant-specific, gene-/protein-based regulators and markers) are appropriate and supportive, MSC will be induced to commit to an osteoblastic lineage, proliferate, build a mature bone matrix, and finally mineralize. The final stage of osteoblastic differentiation is transition into an osteocyte, which resides within the lacunae of mineralized tissue (Figure 2.1).

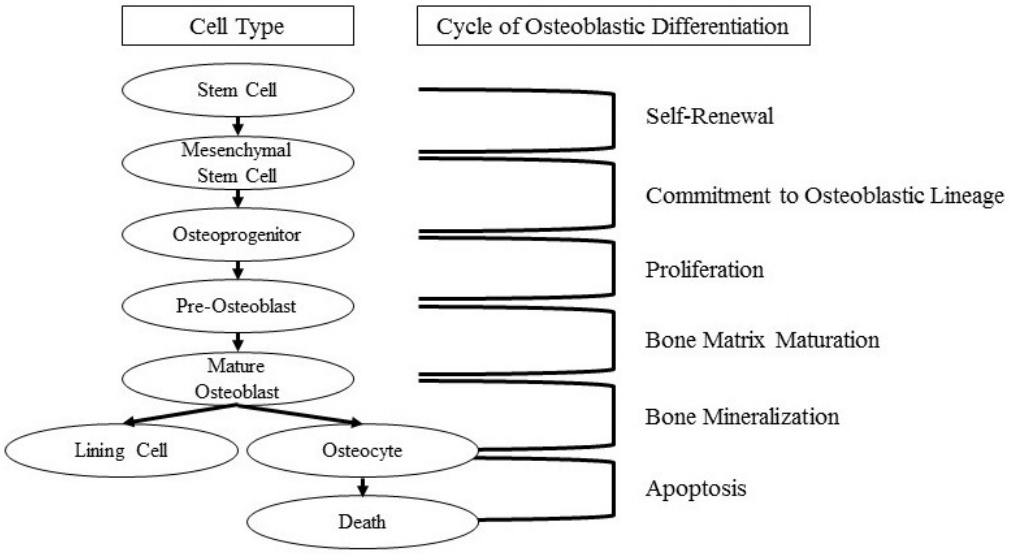

Figure 2.1. *Illustration of the cycle of osteoblatic differentiation at the cellular level. Figure adapted from Miller et al.[10]*

Protein- and molecular-level regulators guide each step in the cycle of osteoblastic differentiation. Numerous molecular signals, including transforming growth factor beta (TGF-β) superfamily proteins, push uncommitted stem cells toward a mesenchymal lineage.[10] Then, MSC are driven toward an osteoblastic phenotype by specific molecular cues, including growth factors such as platelet-derived growth factor (PDGF), insulin growth factor 1 (IGF-1), and bone morphogenetic protein 2 (BMP-2). At this stage, the protein runt-related transcription factor 2 (RUNX2) advances proliferation to the preosteoblast stage; however, if peroxisome proliferator-activated receptor gamma 2 (PPARγ2) is expressed instead, the stromal cells will progress to adipocyte (fat cell) lineage.[17, 18] To further promote osteoblast cell differentiation toward mature osteoblasts, glucocorticoid, Vitamin D, insulin growth factor 2 (IGF-2), and prostaglandin E2 (PGE-2) are required.[10]

In addition to osteoblastic differentiation and subsequent mineralization, there is a coupled process of bone remodeling between bone anabolism and bone catabolism. In normal bone remodeling, during the early stages of bone tissue mineralization, anabolism exceeds catabolism. As new bone tissue matures, osteoclasts, derived from HSC and composed of fused monocytes, resorb bone in order to contribute to the overall bone structure. Via the receptor activator of necrosis factor - κ B ligand/ receptor activator of necrosis factor - κ B/osteoprotegerin (RANKL/RANK/OPG) pathway, osteoclasts and osteoclast precursors express the RANK receptor on the surface of the cells, while osteoblasts express RANKL. RANKL then attaches to RANK, which promotes proliferation and differentiation of cells to form osteoclasts as well as prevent cell apoptosis. OPG, which is also produced by osteoblasts, modulates RANKL by impeding the attachment between RANKL and RANK.[19, 20] Systemically, many other hormones and genes also participate in the dynamic process of bone formation and remodeling. Estrogen hormones inhibit osteoclasts precursors, decrease the pro-inflammatory cytokine interleukin 6 (IL-6), and increase rates of osteoblast survival.[18, 21, 22] Parathyroid hormone (PTH) also stimulates osteoblast activity and acts in concert with RUNX2 to advance osteoprogenitor cells to preosteoblasts by increasing expression of RANKL.[18, 23] Insulin growth factor 1 (IGF-1) increases osteoblast function and cortisol causes osteoblast apoptosis.[18, 22, 24] Calcitonin inhibits osteoclastic activity, while thyroid hormone and Vitamin A stimulate osteoclasts.[18, 24] Locally, numerous endothelial, neurologic, and marrow-derived growth factors, such as fibroblast growth factor (FGF), TGF-β, and integration site-1 + wingless in Drosophila (Wnt), respectively.[17, 18] Damage to bone tissue, mechanical loading (e.g. exercise, body

weight, weightbearing status) as well as local release of cytokines and growth factors in response to systemic hormones (e.g. estrogen) all influence the bone remodeling process. Other factors may affect the process, but remain unknown.[25]

2.3 Material Selection of Orthopaedic Implants for Osseointegration

A limited number of metals are approved by the American Society for Testing and Materials (ASTM) and Food and Drug Administration (FDA) for implantation, including titanium, stainless steel, cobalt-chromium-molybdenum (Co-Cr-Mo), and some refractory (e.g. zirconium, tantalum) alloys. Titanium-6Aluminum-4Vanadium (Ti-6Al-4V) alloy is commonly used for THA femoral stem and TKA tibial tray components, due to its chemical inertness (biocompatibility) and corrosion resistance as well as torsional and axial stiffness moduli similar to bone. This match between mechanical properties of Ti-6Al-4V and bone results in a reduction of stress shielding, compared to other alloys. Titanium alloys also maintain a passive oxide layer (TiO_2), which promotes corrosion resistance. However, Ti-6Al-4V has lower hardness values, approximately 15% less than Co-Cr-Mo alloys, and decreased wear resistance, making Co-Cr-Mo alloys a superior material for articulation-based conditions.[26] Several seminal studies reported successful osseointegration of titanium implants, which has propelled continued research of the process.[27-29]

These approved metal alloys are also used to modify orthopaedic implant surfaces. Surface modification techniques, especially macroscale and microscale coatings, have historically been used to promote early and long-term osseointegration of non-articular joint replacement component surfaces. Current surface modification

techniques incorporate desired composition and surface chemistry, but lack nanoscale topographical features beneficial for cell attachment (Table 2.1).

Table 2.1. *Current surface modification techniques of orthopaedic implants.*

Coating/Modification	Material
Roughened	Titanium Alloys
Bead	Titanium and Cobalt-Chromium-Molybdenum Alloys
Wire/Fiber Mesh	Titanium Alloys
Plasma-Spray	Titanium Alloys
Bioactive Non-Metallics	Hydroxyapatite
Growth Factors	Transforming growth factor beta (TGF-β), Bone morphogenetic protein 2 (BMP-2)

These coatings, however, are subjected to shear loads during surgical implantation, contact with surgical tools, and eventually micromotion at the bone-implant interface during a patient's activities of daily living. As a result, these coatings may separate from the substrate, generating third-body wear debris that increases mechanical wear of bearing surfaces (Figure 2.2). Additionally, local phagocytic cells encountering this debris may initiate a biologic cascade leading to periprosthetic osteolysis. The body's immune response to wear debris, which is dependent on particulate composition, concentration, and morphology, results in osteoclastic bone resorption around the implant, component loosening, and ultimately revision surgery.[30]

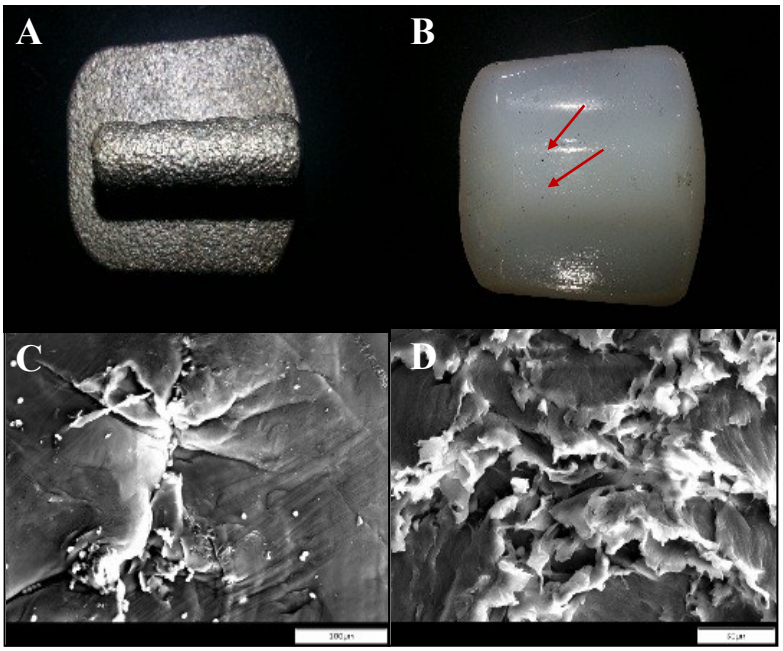

Figure 2.2. *Digital and scanning electron images of a retrieved total ankle arthroplasty prosthesis. Pictured are a (A) digital image of macroscale architecture on region of surface-modified titanium alloy for osseointegration of TAA titanium tibial component, (B) digital image of embedding damage of retrieved TAA polyethylene liner, (C) representative scanning electron micrograph demonstrating effect of embedding damage to polyethylene component (scale bar: 100 μm), (D) representative scanning electron micrograph showing severe polyethylene damage and sloughing of wear debris (scale bar: 50 μm).*

Chapter 3:

Titania Nanotube Surfaces for Orthopaedic Implant Applications

3.1 Introduction

When cells encounter implant surfaces, the structure/topography, roughness, mechanical properties (specifically, stiffness), phase structure, and surface chemistry all affect the rate and quality of cell attachment as well as the propensity for cells to differentiate to an osteoblastic phenotype.[31-36] These material properties are one factor determining whether fibrous or bone tissue are formed.[31] Nanoscale metals, with grains less than 100 nm in diameter, have been increasing evaluated for biomedical, and specifically orthopaedic, applications with the hypotheses that matching materials with nanoscale roughness relative to nanoscale bone tissue structures will increase osseointegration, decrease stress shielding, and decrease wear debris generation.[37-40] In comparison, "conventional" materials, currently in-use, are characteristically "micro-rough" (i.e. rough at the micron scale) and "nano-smooth" (i.e. smooth at the nanoscale).

Webster, *et al.* assessed osteoblast cell adhesion on nanophase and conventional titanium, Ti-6Al-4V, and Co-28Cr-6Mo surfaces. Osteoblast adhesion was observed on both the nanophase and conventional surfaces, preferentially at the particle boundaries; however, the nanophase surfaces demonstrated increased osteoblast adhesion, possibly due to the greater number of boundaries on the nanophase surfaces.[37] In a separate study Gutwein, *et al.* investigated osteoblast response between nanoscale and conventional (i.e. micron scale) titania particles at various concentrations and confirmed

Material contained in this chapter is planned for journal submission.

increased osteoblast apoptosis in the presence of conventional versus nanophase particulates.[41] Nanotextured metallic materials, with nanotopographical features, have also been developed using various techniques (e.g. oxidation-controlled, alkali-heat treatment, hydrothermal, laser ablation) and investigated, with respect to cell adhesion, differentiation, and proliferation.[42-48]

A novel surface treatment, titania nanotubes etched via an electrochemical anodization process from titanium alloy, represents a new, industrially-viable method to enhance osseointegration of orthopaedic implants.[49] The processing conditions and resultant material structure of titania nanotube surfaces prepared via anodic oxidation were first described in 2001.[50] The group used a 0.5-3.5 wt% hydrofluoric acid solution to etch aligned nanotubes. When voltage increased, the nanotube diameter also increased, producing tubes with diameters between 25 and 65 nm.[50]

Subsequent research has focused on modification of processing and post-processing conditions, such as reformulating the electrolyte solution, adjusting voltage as well as varying the etching time and temperature, to achieve distinct surface properties and features.[51-53] Recent work has also included the use of different titania alloys and integration other materials into the etching process, coating applications to the titania arrays for enhancing antibacterial or osseointegration as well as pharmacologic agents and small molecules to load nanotubes for augmenting and modifying biologic processes.[54-63]

3.1.1 Previous In Vitro Studies of Titania Nanotube Surfaces for Osseointegration Applications

Previous studies have demonstrated the biocompatible and osteoconductive properties of aligned, vertically-oriented titania nanotube arrays etched from Ti-6Al-4V alloy and unmodified by post-processing methods.

Nanotube diameter has been studied in the context of cellular response, using various cell lines. One study cultured human mesenchymal stem cells (hMSC; human umbilical cord-derived) onto titania nanotube surfaces with a range of diameters (15, 20, 30, 50, 70, and 100 nm), and showed that 15 nm-diameter surfaces generated greater mineralization (alizarin red staining) and osteocalcin expression than other groups, including unmodified control surfaces.[64] Park, *et al.* concluded that nanotubes less than 30 nm and greater than 50 nm impeded mesenchymal stem cell adhesion and spreading; [65] however, a separate study showed hMSC attachment on 30 nm diameter tubes, although subsequent differentiation did not transpire. When tube diameter was increased to 70-100 nm, there was a 10-fold increase in stem cell elongation as well as comparative increases in alkaline phosphatase (ALP), osteocalcin, and osteopontin activity.[66] For reference, hMSC (placental-derived, P6), on average, are approximately 26.5 μm in diameter (range, 15 to 50).[67] With rat-derived MSCs cultured onto 80 nm-diameter nanotubes, Popat, *et al.* also showed greater ALP activity as well as calcium and phosphorus deposition on titania nanotube surfaces compared to unmodified titanium.[68] After seeding human osteoprogenitor cells onto TiNT surfaces with 120 nm tube diameters, Das, *et al.* stained for alkaline phosphatase and showed increased cell counts with osteoblastic phenotype, and again documented filopodia attachment to

nanotubes.[69] Yu, *et al.* seeded mouse preosteoblast cells (MC3T3-E1) onto titania nanotube surfaces, and reported greater cell adhesion, ALP activity, and mineralization on titania nanotube arrays with diameters ranging from 20-70 nm versus 100-120 nm.[70] Large diameter, 150-470 nm, titania nanotube surfaces were seeded with mouse preosteoblast cells. The greatest cell elongation and cell attachment were observed on surfaces with 150 nm diameter and 470 nm diameter nanotubes, respectively. Maximum ALP activity was measured on 150 nm diameter surfaces, and ALP activity decreasing as diameter increased.[71]

The phases of titanium, amorphous, anatase or rutile (i.e. annealed or unannealed), have been the focus of several studies. In double-concentration simulated body fluid alone for 7 days, Fan, *et al.* showed that titania nanotube surfaces induced apatite formation, with greater calcium and phosphorus deposition on annealed versus unannealed titania nanotube surfaces.[72] Shin, *et al.* demonstrated the hydrophilicity of titania nanotube surfaces, due to the anodization process, compared to unmodified titanium. Surface hydrophilicity was increased additionally by subjecting samples to a post-anodization annealing process,[73] and a follow-up study showed that hydrophilic surfaces allowed greater mouse preosteoblast cell spreading.[74] Hamlekhan, *et al.* investigated aging of titania nanotube surfaces (i.e. conversion from anatase to rutile as indicated by loss of hydrophilicity), and confirmed crystallinity and morphology control hydrophilicity, with nanotube surfaces anodized at 60V and annealed at 600°C maintaining hydrophilic properties for 60 days. The authors further concluded an annealing temperature of at least 450°C maintains hydrophilicity for approximately 2 weeks.[75]

Numerous studies used cell lines with preosteoblastic or osteoblastic lineages to evaluate titania nanotube surfaces. In two studies, Oh, *et al.* measured mouse preosteoblast cell adhesion and spreading on TiNT surfaces, and observed increased cell counts, hydroxyapatite deposition, and cell filopodia attachment within nanotube pores.[76, 77] Shokuhfar, *et al.* assessed mouse preosteoblast cell attachment and density by seeding onto TiNT surfaces with nanotubes averaging 100 nm in diameter, and confirmed similar trends. Focused ion beam milling provided visualization of individual cell attachment via filopodia to nanotubes.[74] When comparing titania nanotubes ranging from 30 nm to 100 nm diameter cultured with mouse preosteoblast cells, ALP activity on titania nanotube surfaces (all diameters) significantly increased compared to controls, and increased proportionally with nanotube diameter.[78] Culturing fetal rat calvarial cells on TiNT surfaces demonstrated equivalent cell viability of TiNT and unmodified titania surfaces, yet TiNT surfaces exhibited increased ALP activity as well as bone sialoprotein, osteocalcin, and PGE-2 expression.[79, 80] A separate study that seeded titania nanotube surfaces with primary rat calvarial osteoblast cells also showed increased ALP activity, compared to smooth and acid-etched titania surfaces.[81]

Several studies investigated gene-level response to titania nanotube surfaces. Filova, *et al.* discussed the importance of the wall thickness of the nanotubes, and seeding human sarcoma osteogenic 2 cells (Saos-2) onto titania nanotube arrays with wall thicknesses from 14 to 19 nm, on average. After 7 days, greater activity of ALP, Type I collagen, and osteopontin were measured on samples with thinner walls.[82] Pozio, *et al.* conducted a gene-based analysis of TiNT surfaces seeded for 15 and 30 days with human osteoblasts and found selected genes related to osteoblast differentiation were

upregulated, including RUNX2.[83] Bacterial adhesion on titania nanotube surfaces as a function of nanotube diameter was investigated by Ercan, *et al.* Both Staphylococcus epidermis and Staphylococcus aureus were cultured on annealed and unannealed titania nanotube surfaces with 20, 40, 60, and 80 nm-diameter nanotubes as well as unmodified, conventional titanium for 1 hour. Compared to control, annealing the surfaces decreased the number of dead bacteria adhering to surfaces, which can increase attachment and proliferation of live bacteria, and nanotube surfaces with larger individual nanotube diameters decreased the number of live bacteria. Annealing and surfaces with larger diameter nanotubes, in combination, exhibited the least adhesion of any groups.[84]

3.1.2 Previous In Vivo Studies of Titania Nanotube Surfaces for Osseointegration Applications

In vivo studies provide an opportunity for translation of *in vitro* methods and results. Numerous studies have used animal-based models to evaluate osseointegration of aligned TiNT surfaces. This section will focus on TiNT surfaces etched from Ti-6Al-4V alloy, which are otherwise unmodified.

Implantation in a rodent model, to assess of biocompatibility of titania nanotube surfaces, was performed with two Lewis strain rats with a 4-week endpoint. Samples were implanted within a pocket between skin and muscle layers. Hematoxylin and eosin (H&E) showed a lack of fibrous tissue.[68] In a rabbit model, grit-blasted and TiNT-etched (~90-108 nm diameter nanotubes; 3.75 mm diameter implant) screw implants were placed in femoral condyles for 6 weeks. Woven bone was observed in the periosteal region, while toluidine blue staining confirmed new bone formation in the endosteal

region. Quantifying bone formation around implants with backscattered electron imaging showed significantly greater bone formation around TiNT implants. Removal torque, a measurement of the bone-implant interfacial shear strength, was also significantly greater for the TiNT implants.[85] Bjursten, *et al.* implanted titania disks with titania nanotube and grit-blasted morphologies transversely onto rabbit tibiae. After a 4-week endpoint, samples were subjected to tensile testing, with titania nanotube-etched implants exhibiting significantly greater pull-out forces than grit-blasted implants. H&E staining demonstrated greater bone-implant contact, bone formation, and presence of calcium in tissue surrounding titania nanotube implants.[86]

Large animal species were used in several studies. Fan, *et al.* inserted cylindrical implants with three surfaces, annealed titania nanotubes, unannealed titania nanotubes, and porous titanium (control), transversely into canine femora for 3 months. Both the annealed and unannealed titania nanotube surfaces showed significantly greater biomechanical push-out strength. H&E staining showed *de novo* bone tissue formation on both titania nanotube surfaces.[72] In a minipig model, four implant types (unmodified as well as 30, 70, and 100 nm-diameter nanotube surfaces) were inserted into the front bone (skull) for endpoints at 3, 5, and 8 weeks. Gene expression analysis showed osterix (OSX), ALP, Type I collagen were significantly greater for 30, 70, and 100 nm-diameter nanotube surfaces, compared to control. Harvested implants were embedded and stained with methylene blue-basic fuchsin, which indicated significantly greater bone-implant contact for all titania nanotube surfaces at all timepoints, with the 70 nm-diameter nanotube surfaces demonstrating the most bone-implant contact.[87] Using a porcine (adult domestic) model, von Wilmowsky, *et al.* implanted TiNT-etched rods (30 nm

diameter nanotubes; 4.2 mm diameter implants) into the skull. Immunohistochemical analysis showed significantly increased Type I Collagen of TiNT implants versus Controls at Days 7, 14, and 30 postoperative, indicating positive effects of TiNT surfaces on bone formation. Imaging via scanning electron microscopy confirmed that nanotubes were intact, confirming that nanotube surfaces survived shear forces during implantation.[88] von Wilmowsky, *et al.* used the same model to investigate the effect of nanotube diameter on osseointegration. Titania nanotube surfaces with 15, 30, 50, 70, and 100 nm diameters as well as unmodified controls were implanted. After harvesting implants *in situ*, implants were embedded, sectioned, and stained with toluidine blue, which showed significantly greater bone-implant contact for 50, 70, and 100 nm-diameter nanotube surfaces, compared to control. Additional immunohistochemical analysis showed greater stained areas of bone morphogenetic protein 2 (BMP-2) on 50, 70, and 100 nm-diameter surfaces as well as osteocalcin on 70 nm-diameter surfaces, compared to control.[89]

3.2 Titania Nanotube Surface Morphologies

In the present study, two morphologies of titania nanotube surfaces, termed Aligned Titania Nanotubes (Aligned TiNT) and Trabecular Titania Nanotubes (Trabecular TiNT) were evaluated *in vitro* and *in vivo* (Figure 3.1). Aligned TiNT surfaces are characterized by vertically-oriented, hollow, tubular structures in parallel, resulting from post-anodization sonication. The Aligned TiNT arrays in this work contained nanotubes that were approximately 50 nm inside diameter and 1 μm in length. Trabecular TiNT surfaces exhibit a disordered morphology similar to trabecular bone.

The pore sizes in this morphology are highly variable, however larger pores are approximately 1 µm in diameter (Figure 3.1C). Also, some nanotubes were observed buried within the porous structure. While these nanotubes could not be measured with acceptable resolution, we anticipate these are similarly-sized to the nanotubes on the Aligned TiNT surfaces due to identical etching methods, as described in Section 3.3.

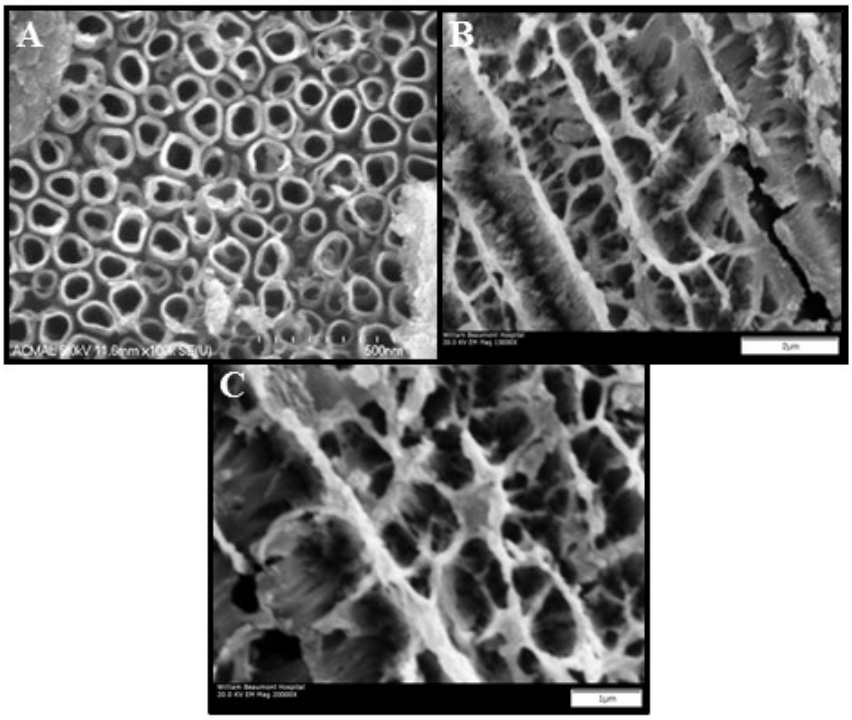

Figure 3.1. *Scanning electron micrographs of titania nanotube surfaces. (A) Aligned TiNT and (B,C) Trabecular TiNT surfaces. (A) Scale Bar: 500nm, (B) Scale Bar: 2 µm, (C) Scale Bar: 1 µm*

3.3 Material Processing of Titania Nanotube Surfaces

The samples for *in vitro* and *in vivo* studies were fabricated with titanium alloy (Ti-6Al-4V) sheet and Kirschner wires (Ti-6Al-4V ELI K-wire), respectively. As-received sheet and wire material were polished with 600 grit abrasive sheet and deionized (DI) water, followed by a DI water rinse and air-drying. Acetone was applied to the

surfaces just prior to etching, and then air-dried. Etching was prevented on the trocar tip of the K-wires with a temporary coating of cyanoacrylate that was removed with acetone after anodization.

In a glass beaker, the samples (sheet or K-wires) were suspended on one side and connected to a variable DC power supply, as the anode. Diametrically opposed to the titanium sample, a small diameter graphite rod was also suspended in the beaker and connected to ground, as the cathode. The electrolyte solution contained 98 vol% ethylene glycol, 2 vol% deionized water, and 0.6 wt% NH_4F. The NH_4F was first dissolved in the DI water and then this solution was added to the ethylene glycol. The electrolyte was added to the beaker at a level just below the electrical connections. Before combining the NH_4F and ethylene glycol, the NH_4F was dissolved in DI water. With all materials and solutions in place, the power supply was engaged (+60 VDC) and etching continued for 40 minutes.

After the etching period, the power supply was disengaged, samples were removed from the solution and subjected to a 1-minute rinse under water, and then air-dried. Aligned TiNT surfaces resulted from ultrasonication in DI water for 2 minutes, however Trabecular TiNT surfaces received no additional ultrasonication. Sheet samples were sectioned into 10 mm x 10 mm coupons. The coating on the trocar tip of each K-wire was removed, however no sectioning was required. Using a programmable annealing oven, with temperature increasing at 7.5°C per minute to a steady-state of 450°C for a total heating time of 3 hours, samples were heat-treated to convert the amorphous titanium to crystalline anatase, which enhanced the hydrophilicity of the TiNT surfaces. After completely cooling the oven over approximately 5 hours, samples

were removed.[73] Control samples were prepared only by rinsing in DI water and air-drying (Figure 3.2).

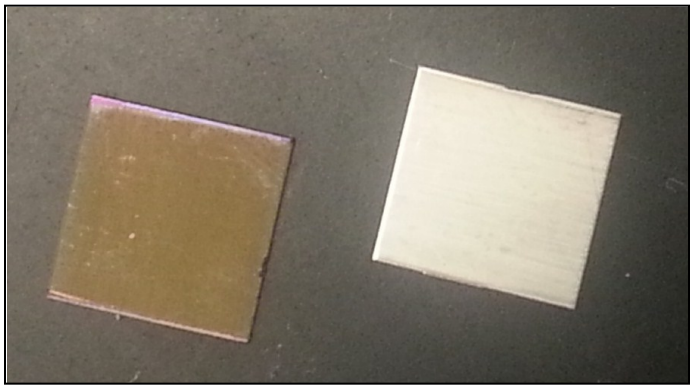

Figure 3.2. *Digital photograph showing the final appearance of coupon samples. (Left) TiNT-etched surfaces appear gold and smooth, compared to (right) unmodified control surfaces.*

Chapter 4:

In Vitro Assessment of Bone Marrow-derived Cells on Titania Nanotube Surfaces

4.1 Introduction

Titania nanotube surfaces, both Aligned TiNT and/or Trabecular TiNT, may provide enhanced conditions for cell attachment compared to unetched titanium (Control) surfaces.[47] If initial cell attachment is increased through nanoscale topographical surface features, cell proliferation, cytoskeleton organization, and cell differentiation may be subsequently enhanced.[90]

For all *in vitro* experiments, cells were isolated from the bone marrow cavities of the femora and tibiae of Sprague Dawley rats, the same rat strain used in subsequent *in vivo* experiments. Using these plastic-adherent bone marrow cells (BMC), an enriched source of mesenchymal stem cells that can differentiate towards numerous cell types, provides another possible translation between *in vitro* and *in vivo* experiments, as the femoral marrow cavity is the same location of implant placement. Therefore, the implants are in contact with the same "cell environment" used in the *in vitro* experiment. Additionally, the selection of BMC for the *in vitro* experiment also challenges the material, as the cells are not obligated to differentiate into osteoblasts and will only differentiate into osteoblasts under specific conditions.

Material contained in this chapter is planned for journal submission.

4.2 Experimental Methods

4.2.1 Bone Marrow Isolation

Bone marrow was harvested from the long bones of 14-week old female Sprague Dawley rats (SD; Charles River Laboratories, Wilmington, MA) for subsequent cell isolation. After euthanizing rats via CO_2 asphyxiation, femora and tibiae were aseptically harvested and proximal and distal ends of the long bones were removed. Warm, sterile phosphate-buffered saline was flushed into the cavities. Whole bone marrow was then plated in T-25 culture flasks and cultured at 37°C and 5% CO_2 in a sterile, copper-lined CO_2 incubator. After a 24-hour incubation, non-adherent cells were removed by rinsing with warm, sterile saline. The BMC, an enriched source of mesenchymal stem cells (MSC) which may differentiate toward numerous cell types, was collected and used for all subsequent experiments.

4.2.2 Bone Marrow Cell-Seeding

To increase attachment potential, all sample coupons were soaked in fetal bovine serum (FBS) for 30 minutes prior to seeding. To seed samples, 40,000 BMC (P2-3) were suspended in 50 µL of media (DMEM; Dulbecco's Modified Eagle Medium), then drop-seeded on samples and incubated for 6 hours before adding the remaining 950 µL of media and incubating for 20 hours to ensure attachment. 'Time zero' commenced after final incubation.

4.2.3 Cell Attachment and Morphology

Early cell attachment and morphology were compared between Aligned TiNT, Trabecular TiNT, and Control surfaces, using three samples per group per timepoint. [47] Timepoints were defined as 0.5, 2, and 4 hours. At each timepoint, cells were fixed on samples with 4% glutaraldehyde, incubated for 30 minutes, then permeabilized with methanol and suspended in phosphate buffered saline before staining with either Actin Green (Actin Green 488 ReadyProbes Reagent, Life Technologies, Carlsbad, CA) for cytoskeleton visualization and morphology (1 drop stain; 40 min incubation) or 4', 6-Diamidino-2-Phenylindole, Dihydrochloride (DAPI; Life Technologies, Carlsbad, CA) for nucleus visualization (0.5 mL stain; 20 min incubation). Following incubation, fluorescence imaging (IX71, Olympus America, Center Valley, PA) at 13 standardized regions of interest per coupon was performed, followed by subsequent quantification of the total number of adherent cells, cell equivalent diameter, and cell eccentricity (Figure 4.1).

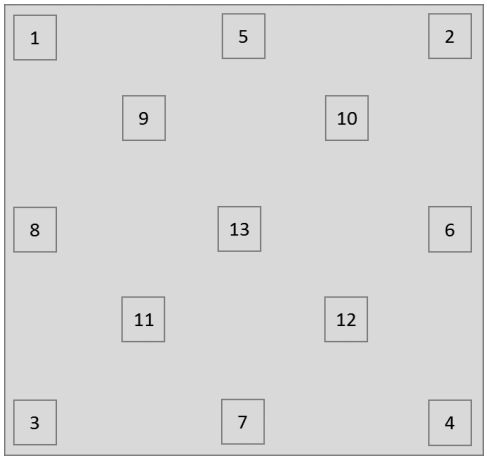

Figure 4.1. *Imaging convention for each coupon in the experiment. Regions were chosen to reflect the corners (1-4), edges (5-8), central area (9-12), and absolute center (13) of each sample.*

Because all non-adherent cells were removed prior to imaging, Actin Green and DAPI also demonstrated cell adhesion of the surfaces. Environmental scanning electron microscopy (SEM; Vega3XMU, Tescan USA, Warrendale, PA) was used to further document cell morphology. Total cell number, cell equivalent diameter, and cell eccentricity were statistically compared using a one-way analysis of variance (ANOVA) model, with a Tukey post-hoc test and α=0.05.

4.2.4 Cell Proliferation and Differentiation

Alkaline phosphatase (ALP) and osteocalcin (OC), molecular markers characteristic of an osteoblastic phenotype, were assayed to evaluate the propensity of BMC cultured on TiNT surfaces to differentiate into osteoblasts. Mature osteoblasts and several osteoblast precursor cells abundantly express ALP; however, ALP is also expressed by other, non-osteoblast cell types. Therefore, a cell on the bone surface must stain positive for ALP to be confirmed as an osteoblast. OC, only expressed in mature osteoblasts, has the highest specificity of any marker defining osteoblastic phenotype.[10]

ALP activity was measured using a commercially-available colorimetric assay (ALP Assay, BioVision, Milpitas, CA). Briefly, after plating in duplicate technical replicates, 50 µL of p-nitrophenyl phosphate (pNPP) was added to each well before mixing and incubating (60 minutes at 25°C) protected from light. Absorbance was measured at 405 nm, relative to pNPP concentration. For experimental samples, background absorbance (absorbance of zero standard) was subtracted before calculating p-nitrophenol (pNP) concentration, and subsequently, ALP activity, using the equation

$$ALP\ Activity\ (U/mL) = A/V/T \qquad Eq.\ 1$$

where A=amount of pNP generated (μmol), V=volume of sample added in the assay well (mL), T=reaction time (min). OC expression was measured via sandwich enzyme-linked immunosorbent assay (Rat Osteocalcin ELISA, Abbexa, Cambridge, UK). Standards, sample, and control (zero) wells, with 50 μL of volume each, were positioned in duplicate technical replicates. After incubation (30 min at 37°C), the plate was washed and horseradish peroxidase (HRP) conjugated anti-osteocalcin antibody was added to each well and incubated (30 minutes at 37°C), before again washing. Tetramethylbenzidine (TMB) substrates, 50 μL each, were then added to each well and incubated (15 minutes at 37°C; protected from light), and absorbance was read at 450 nm. Background absorbance (absorbance of zero standard) were subtracted from experimental sample results and OC concentration was obtained. ALP activity and OC expression in cell culture supernatant was assayed at four time points (3, 7, 14 and 21 days) on six samples per group per time point. Statistical significance was assessed using a two-way analysis of variance (ANOVA, Factor A: group, Factor B: timepoint) with α=0.05, with a Bonferroni post-hoc correction for pairwise comparisons.

Quantitative real-time polymerase chain reaction (qPCR) was used to quantify messenger RNA-level expression of collagen, type 1, alpha-helix 1 (Col1a1), insulin-like growth factor-1 (IGF-1), and osteonectin (ON) gene expression by rat BMC cultured on TiNT (Aligned and Trabecular) and Control surfaces. Expression of each gene (e.g. up- or down-regulation) via transcription results in protein production through a translation process, and these proteins are subsequently transported to the extracellular matrix

(ECM). Protein constituency in the ECM is a dynamic process, which then allows the ECM of neighboring cells to continuously communicate and adapt.[91] Just as in the ALP and OC experiments, qPCR further documents the progression toward osteoblastic phenotype and propensity to produce organic matrix leading to bone formation. These three genes were selected due to their role in bone formation. Col1a1 is a protein that strengthens and supports bone tissue, which is commonly-assayed to quantify Type I Collagen, the primary organic constituent of bone. IGF-1 is a protein molecularly-similar to insulin that stimulates cell growth and proliferation of many cell types, including osteoblasts, while inhibiting apoptosis (cell death). Osteonectin production is a phenotypic characteristic of osteoblasts. This protein binds calcium and is secreted by osteoblasts during matrix mineralization. All gene expression was normalized to B-Actin (ACTB), which was used in data analysis to normalize variations encountered throughout the qPCR process, including sample preparation, RNA isolation, and PCR reaction. At each timepoint (3, 7, 14 and 21 days), six samples per group were prepared in triplicate technical replicates for each group, according to the previously described methods. At experiment endpoint, complementary DNA (cDNA) was synthesized from each sample by reverse transcription from each sample (SuperScript 5X VILO Reaction Mix, Life Technologies, Carlsbad, CA), followed by preamplification (TaqMan PreAmp Master Mix Kit, Life Technologies, Carlsbad, CA, and pooled assay mix) due to the limited quantity of cDNA. The preamplification concluded by thermocycling the samples by: (1) hold at 95°C, (2) cycle (n=14) at 95°C for 15 seconds, and (3) cycle (n=14) at 60°C for 4 minutes. For qPCR analysis, a microcentrifuge tube was prepared for each sample, containing primer, cDNA template, gene expression mix, and nuclease free water

(TaqMan Gene Expression Master Mix, Life Technologies, Carlsbad, CA). Samples were run in triplicate technical replicates and loaded into the qPCR system (Realplex Mastercycler System, Eppendorf, Hauppauge, NY) to obtain cycle threshold (C_T) for each sample, with thermal cycler set to: (1) hold at 50°C for 2 minutes, (2) hold at 95° for 10 minutes, (3) cycle (n=40) at 95°C for 15 seconds, and (4) cycle (n=40) at 60°C for 1 minute. The C_T is the number of cycles required for the generated fluorescent signal to cross the fluorescent threshold, a level significantly above background fluorescence. The resultant C_T value is inversely proportional to the target nucleic acid in the sample. For each sample, the three C_T values obtained for each gene will be averaged. The average C_T value of ACTB will then be subtracted from the average C_T value of each gene to obtain ΔC_T. The transformed ΔC_T was calculated by

$$\textit{Transformed } \Delta C_T \textit{ of sample for specified gene} = 2^{(-\Delta CT)} \qquad \textit{Eq. 2}$$

where the transformed ΔC_T indicates the up- or down-regulation of the specified gene compared to the housekeeping gene, ACTB, on each sample. For each sample, the transformed ΔC_T of ACTB was subtracted from the transformed ΔC_T to obtain the $\Delta\Delta C_T$. The fold change over Control was calculated by

$$\textit{Fold change of sample for specified gene} = 2^{(-\Delta\Delta CT)} \qquad \textit{Eq. 3}$$

Fold change over Control, representing gene expression of TiNT samples normalized to gene expression of Control samples, was averaged for each gene for each

group at each timepoint.[92] The fold change over Control was compared between groups using a two-way analysis of variance (ANOVA, Factor A: group, Factor B: timepoint) with α=0.05, with a Bonferroni post-hoc correction for pairwise comparisons.

4.3 Results

4.3.1 Cell Attachment and Morphology

DAPI staining indicated that cells were viable and adhered on both the TiNT and Control surfaces at the three early timepoints, 0.5, 2, and 4 hours (Figure 4.2). The total number of adherent cells was significantly greater on the TiNT surfaces than Control surfaces, demonstrating faster cell attachment on both TiNT surfaces compared to Control (Figure 4.3). Specifically, total adherent cells on Trabecular TiNT and Aligned TiNT surfaces were significantly greater than Control at 0.5 hours ($p=0.014$ and $p=0.018$, respectively) and four hours ($p=0.008$ and $p=0.044$). Over the 3.5-hour period, the number of cells increased on all surfaces, and the total number of adherent cells was equivalent or slightly greater on Trabecular TiNT surfaces compared to Aligned TiNT surfaces. Analysis of total cell count was unfeasible at later timepoints (3, 7, 14, 21 days) due to cell coalescence or superimposition.

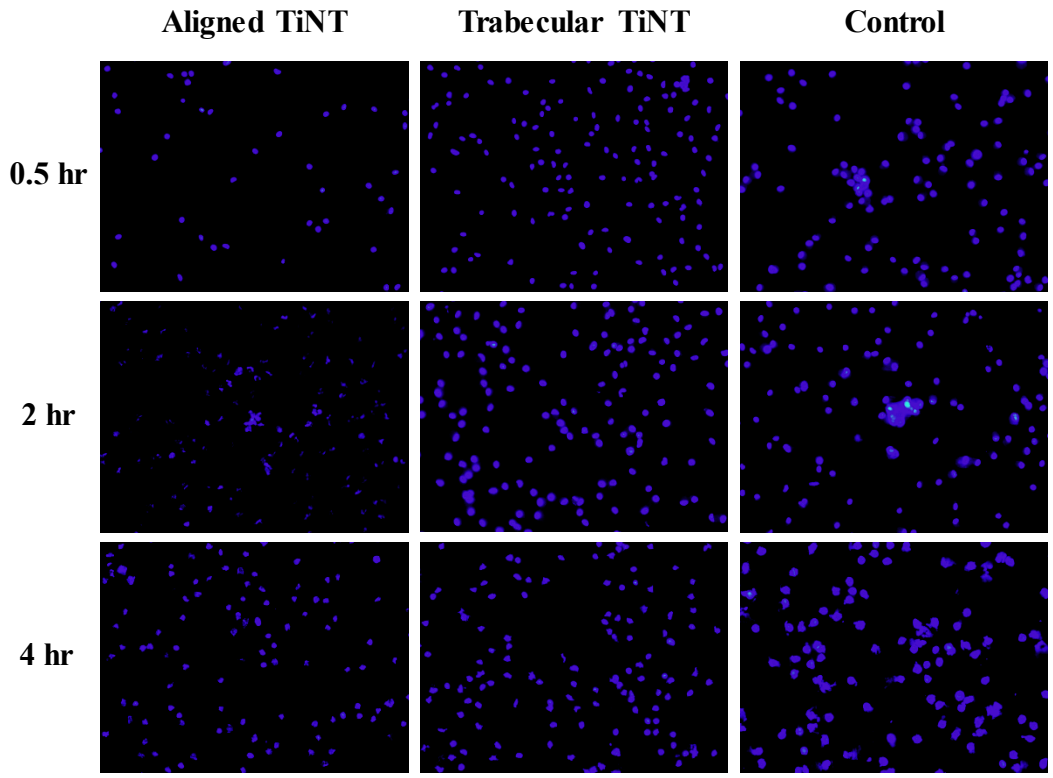

Figure 4.2. *Representative fluorescent images of DAPI-stained surfaces. Aligned TiNT, Trabecular TiNT, and Control surfaces at three early timepoints are shown. Timepoints were 0.5, 1, and 2 hours. For each substrate, the images are the same sample coupon and coupon position (Coupon #2; Position #13—center for all).*

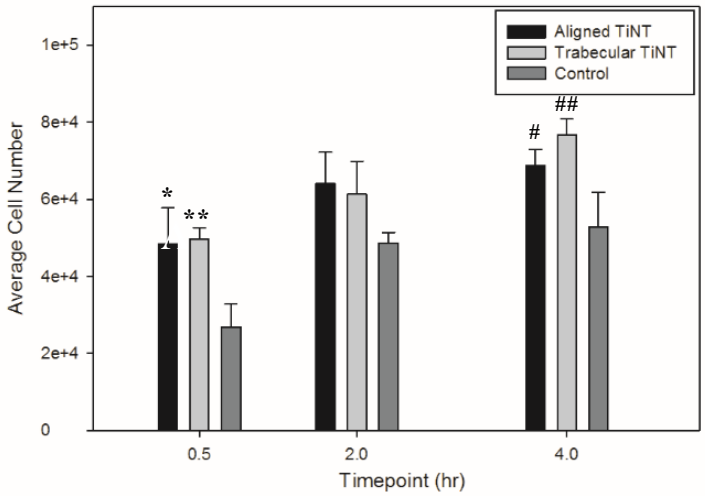

Figure 4.3. *Average total cell number on sample surfaces. Total cell number was assessed at three early timepoints on TiNT and Control samples. Timepoints: 0.5, 2, and 4 hours. *Trabecular TiNT vs. Control, p=0.014; **Aligned TiNT vs. Control, p=0.018; #Trabecular TiNT vs. Control, p=0.008; ##Aligned TiNT vs. Control, p=0.044.*

Actin Green staining showed active cell spreading on TiNT and Control surfaces at all timepoints (Figure 4.4). At the 2- and 4-hour timepoints, increased spreading was observed on TiNT surfaces compared to Control surfaces. Additional imaging via SEM showed differential cell morphology patterns as a function of sample topography (Figure 4.5). On the TiNT surfaces, cells exhibited a globular shape, compared to the elongated, fibrillar cell morphology on Control surfaces.

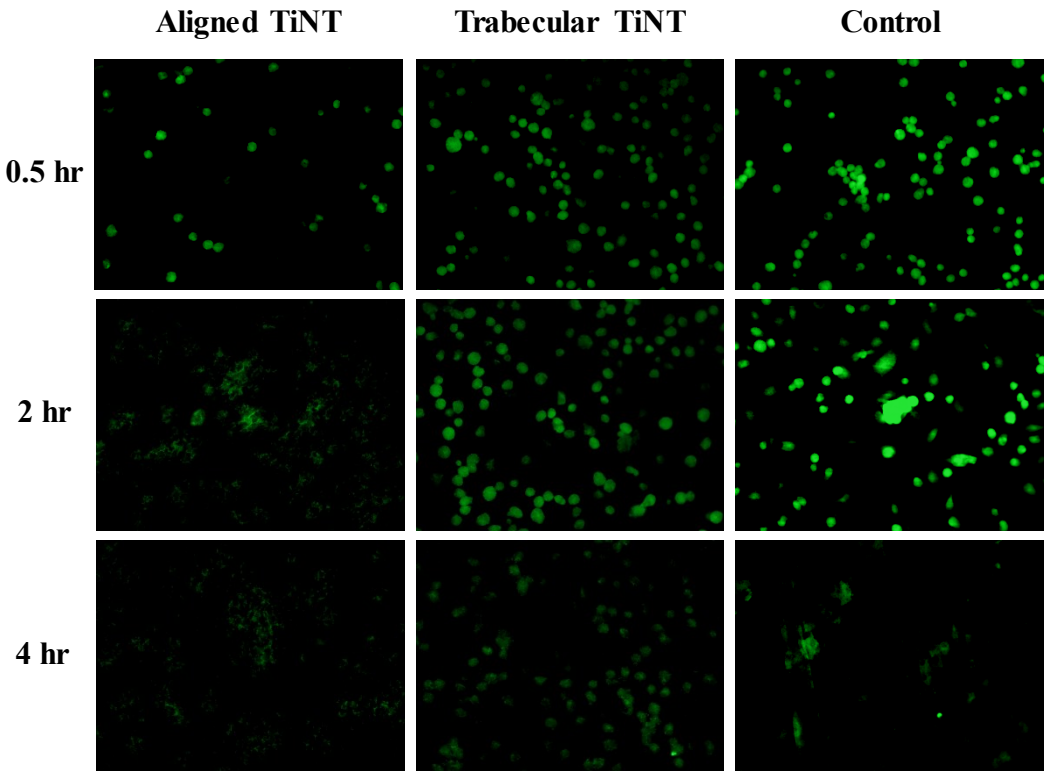

Figure 4.4. *Representative fluorescent images of Actin Green-stained surfaces. Aligned TiNT, Trabecular TiNT, and Control surfaces at three early timepoints are shown. Timepoints were 0.5, 1, 2 hours. For each substrate, the images are the same sample coupon and coupon position (Coupon #2; Position #13 for all).*

.

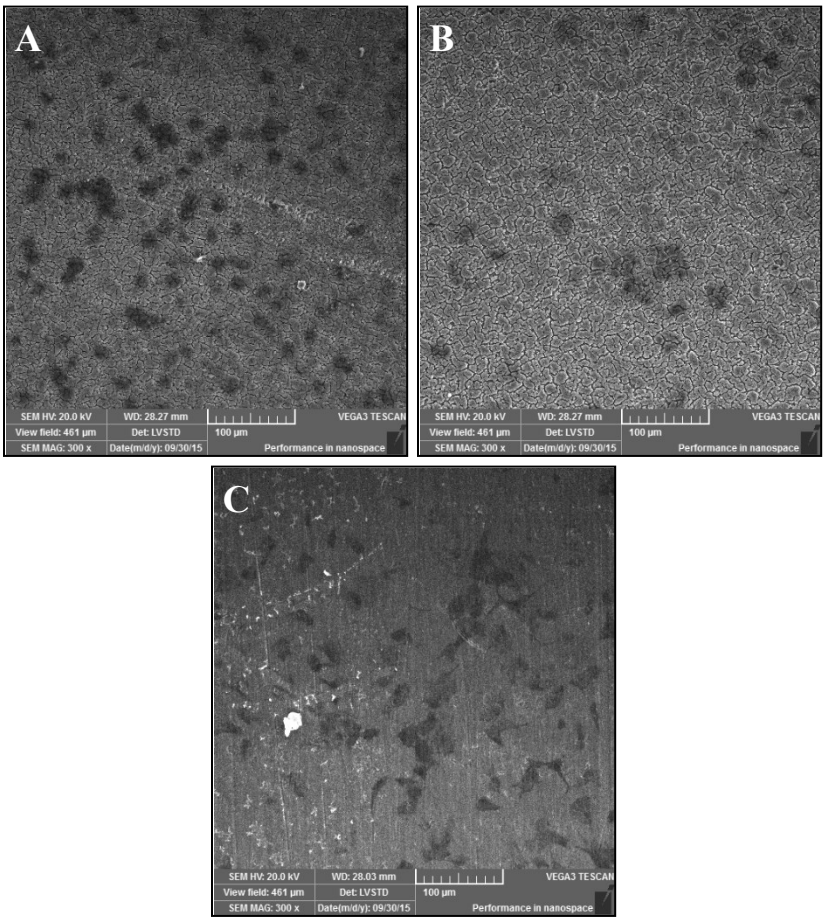

Figure 4.5. *Representative scanning electron micrographs of sample surfaces. Differential cell spreading patterns via extracellular matrix aggregates are illustrated on TiNT and Control samples. Pictured are representative images of (A) Aligned TiNT, (B) Trabecular TiNT, and (C) surfaces at the 3-day attachment timepoint.*

Subsequent analysis of cell morphology images yielded cell equivalent diameter and eccentricity (Figure 4.6). Quantification of the cell equivalent diameter indicated that BMC on the TiNT surfaces were smaller (in diameter) than BMC on Control surfaces. The discrepancy in cell diameter was significant between Trabecular TiNT and Aligned TiNT surfaces versus Control at 0.5 hours ($p=0.031$ and $p=0.048$, respectively). At the 2-hour timepoint, there was a significant difference in diameter between only the Aligned TiNT and Control surfaces ($p=0.008$). At 4 hours, the difference in diameter was

significant for both Trabecular TiNT and Aligned TiNT, compared to Control (both p=0.003).

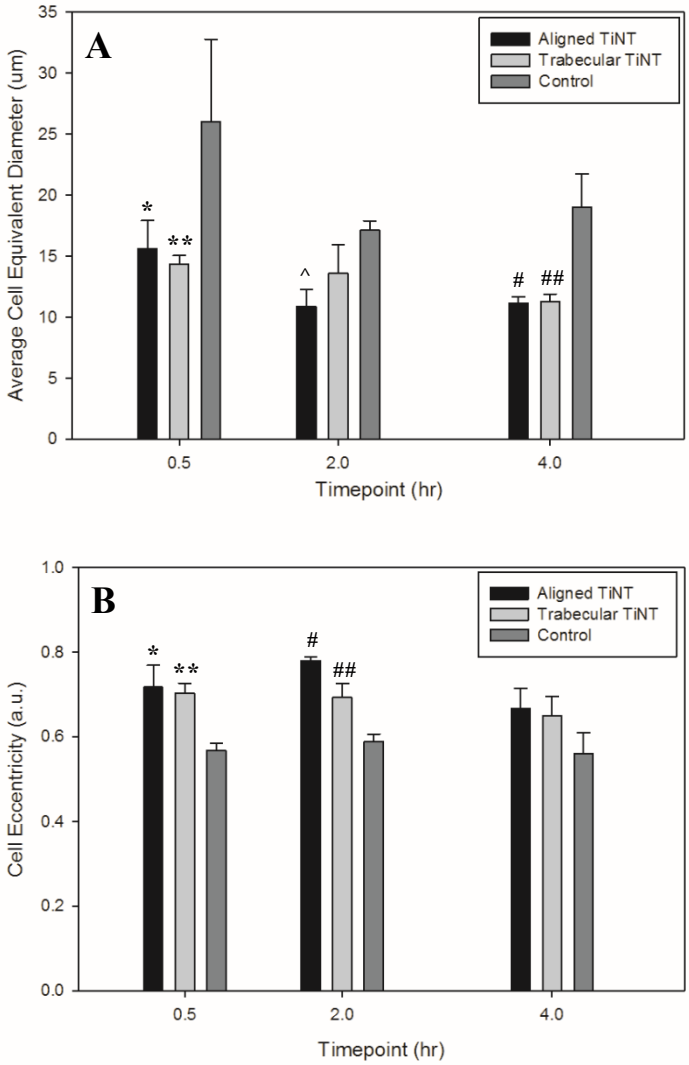

Figure 4.6. *Average cell equivalent diameter and eccentricity on samples surfaces. Average cell equivalent diameter and cell eccentricity were assessed at three early timepoints on TiNT and Control samples. Timepoints: 0.5, 2, and 4 hours. For (A) Cell Diameter: *Aligned TiNT vs. Control, p=0.048; **Trabecular TiNT vs. Control, p=0.031; ^Aligned TiNT vs. Control, p=0.008; #Aligned TiNT vs. Control, p=0.003; ##Trabecular TiNT vs. Control, p=0.003. Cell For (B) Cell Eccentricity: *Aligned TiNT vs. Control, p=0.004; **Trabecular TiNT vs. Control, p=0.007; #Aligned TiNT vs. Control, p<0.001; ##Trabecular TiNT vs. Control, p=0.003.*

Cells on the TiNT surfaces had significantly greater eccentricity than on the Control surfaces, with cells on Aligned TiNT demonstrating the greatest eccentricity. At 0.5 hours, there was a significant difference in eccentricity between the Trabecular TiNT and Aligned TiNT, compared to Control ($p=0.007$ and $p=0.004$, respectively). There was a significant difference between both the Trabecular TiNT and Aligned TiNT groups versus Control again at 2 hours ($p=0.003$ and $p<0.001$, respectively). There were no significant differences in eccentricity between groups at the 4-hour timepoint.

4.3.2 Cell Proliferation and Differentiation

Aligned TiNT, Trabecular TiNT, and Control surfaces were compared to one another and Control samples with respect to ALP activity and OC expression by cultured rat marrow-derived BMC (Figure 4.7). ALP and osteocalcin were expressed throughout the experiment, demonstrating the differentiation of the BMC to osteoblastic phenotype. After a large, initial secretion of ALP and OC at Day 3, expression on the Aligned TiNT was approximately constant for the remainder of the timepoints, yet always greater than Control. Trabecular TiNT surfaces exhibited greater ALP activity and OC expression than Control at Day 3, then decreased expression at Day 7 before progressively increasing for the remainder of the experiment.

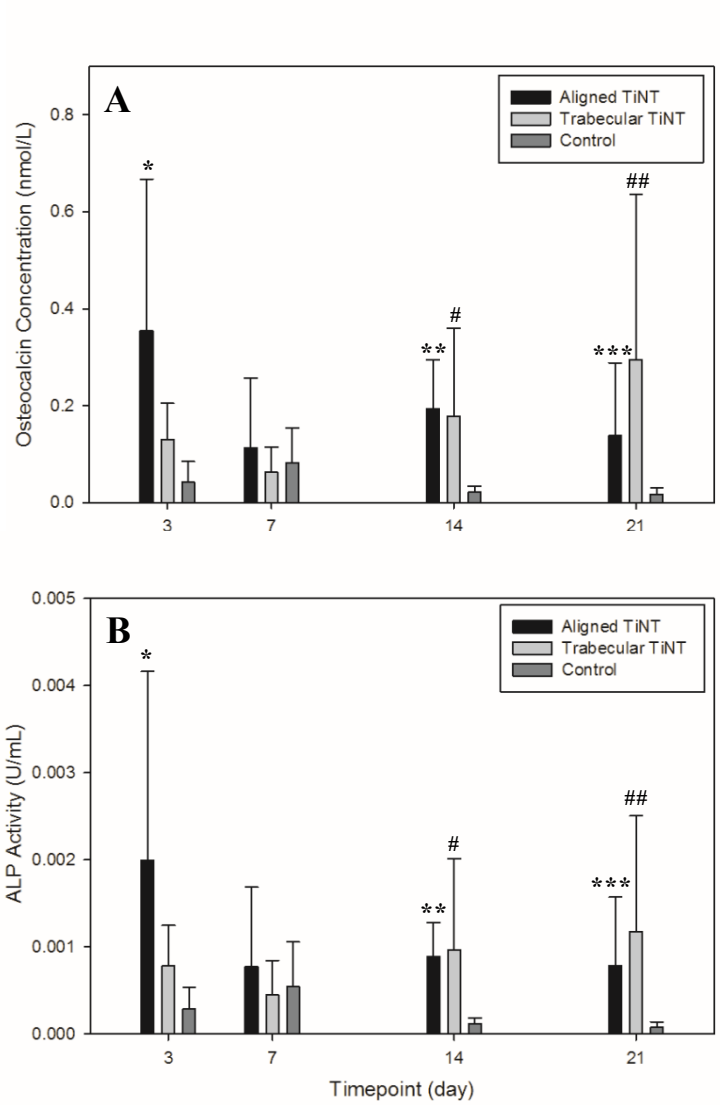

Figure 4.7. *Osteocalcin expression and alkaline phosphatase (ALP) activity on sample surfaces. Presented are Aligned TiNT, Trabecular TiNT, and Control surfaces at four timepoints. Timepoints: 3, 7, 14, and 21 days. For (A) osteocalcin, n=6/group; *p=0.005 vs. Control, ** p=0.003 vs. Control, # p=0.039 vs. Control, *** p=0.009 vs. Control, ## p<0.001 vs. Control. For (B) alkaline phosphatase, n=6/group; *p=0.014 vs. Control, ** p=0.004 vs. Control, #p=0.037 vs. Control, ***p=0.001 vs. Control, ##p<0.001 vs. Control.*

After statistically comparing OC expression between groups via two-way ANOVA, significance was found between Aligned TiNT vs, Control at Day 3 (p=0.005), Aligned TiNT vs. Control and Trabecular TiNT vs. Control at Day 14 (p=0.003 and

p=0.039, respectively) as well as Aligned TiNT vs. Control and Trabecular TiNT vs. Control at Day 21 (p=0.009 and p<0.001, respectively). Statistical analysis of ALP activity between groups using a two-way ANOVA mirrored the osteocalcin analysis, showing significance of Aligned TiNT vs. Control at Day 3 (p=0.014), Aligned TiNT vs. Control and Trabecular TiNT vs. Control at Day 14 (p=0.004 and p=0.037, respectively) as well as Aligned TiNT vs. Control and Trabecular TiNT vs. Control at Day 21 (p=0.001 and p<0.001, respectively).

qPCR was performed to quantify Col1a1, IGF-1, ON gene expression of BMC cultured on Aligned TiNT, Trabecular TiNT, and Control surfaces at the same four timepoints. For each sample, three C_T values were obtained for each gene and averaged and all gene expression was normalized to the ACTB housekeeping gene (Figure 4.8). Data was log-transformed, and groups were then statistically compared using a two-way ANOVA to assess fold change over Control data. No significant differences were found between the TiNT groups at each timepoint for any of the genes. For Col1a1, there were significant differences between fold change of Trabecular TiNT surfaces over Control between the 3-day and 1-week timepoints (p=0.004) as well as between the 1-week and 3-week timepoints (p=0.004). For osteonectin, there was a significant difference between fold change of Trabecular TiNT surfaces over Control between the 3-day and 1-week timepoints (p=0.046).

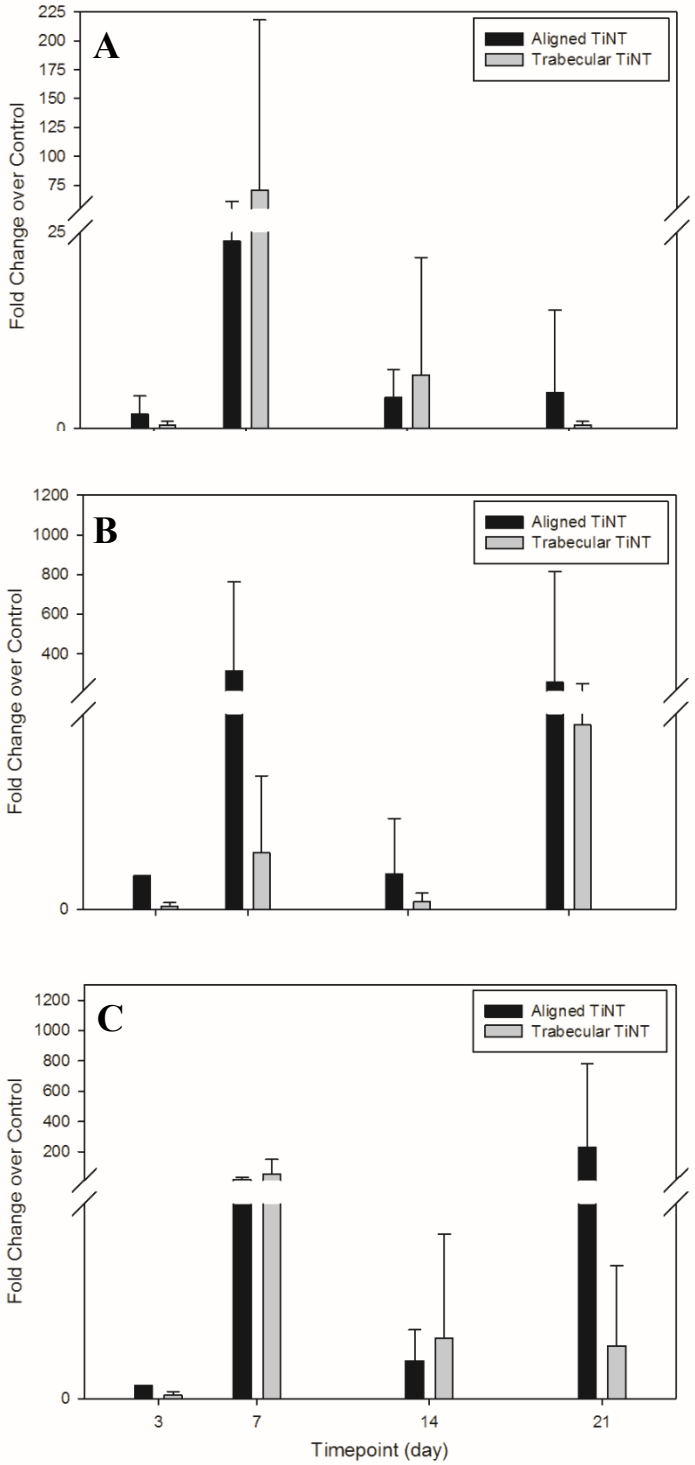

Figure 4.8. *Gene expression on TiNT and Control surfaces. Gene expression is presented as a function of fold change of Aligned TiNT and Trabecular TiNT over Control at four timepoints. Genes assayed were (A) Col1a1, (B) IGF-1, and (C) osteonectin.*

4.4 Discussion and Conclusions

We evaluated the biocompatibility of Aligned and Trabecular TiNT surface via an *in vitro* study focused on cell morphological and attachment behavior as well as osteoconductive properties focused on the characterization of osteoblastic differentiation of BMC cultured on TiNT surfaces by assaying ALP activity, OC expression, and gene expression.

In vitro testing, using widely-used analysis techniques, of BMC seeded on TiNT and Control surfaces was performed.[47, 81, 93] DAPI and Actin Green staining demonstrated cell attachment and spreading from 0.5 hours through 21 days on all surfaces, an indication of the suitable environment of both TiNT surfaces and Control. Total cell counts were greater on TiNT surfaces compared to unetched Controls at the three early timepoints, which corresponds with current trends in the literature.[36, 68, 94] We also observed that the diameter of BMC on TiNT surfaces was smaller compared to cells seeded onto Controls, and cells on TiNT surfaces were more eccentric than cells on Controls. These data correspond with SEM imaging of attached BMC, which showed rounded cell morphology on TiNT surfaces and fibrillar-shaped cells on Control surfaces. The diameter, eccentricity, and imaging findings may be an indication that the cells are developing in different planes on the TiNT surfaces compared to Controls. Shokuhfar sectioned TiNT arrays seeded with osteoblasts (MC3T3-E1; mouse preosteoblasts) and observed cell attachment on nanotube arrays as well as cell filopodia stretching downward into the hollow portion of individual nanotubes.[74] Therefore, these differences in cell morphologic behavior between groups may be explained by the BMC

interaction with TiNT surfaces, as the BMC extend into nanotubes and voids within the array, instead of across the top of the surface.

ALP and OC assays, indicators of activity signaling a shift of BMC toward an osteoblastic phenotype, showed that both ALP activity and OC expression were signficantly greater on TiNT surfaces at multiple timepoints, compared to Control as well as indirectly indicated cell viability. These results corresponded with a study by Popat, *et al*. that showed increased ALP activity of titania nanotube surfaces seeded with MSC compared to unmodified titanium, which was indicative of cell adhesion, proliferation, and differentiation to an osteoblastic phenotype.[68] Zhao, *et al*. described increased ALP activity in titania nanotube surfaces etched at two different voltages (5V and 20V), compared to smooth and acid-etched microstructured surfaces, after seeding samples with primary rat calvarial osteoblast cells.[81] When comparing titania nanotubes ranging from 30 nm to 100 nm diameter cultured with mouse preosteoblast cells (MC3T3-E1), Brammer, *et al*. measured significantly increased ALP activity on all titania nanotube surfaces, compared to flat titanium control samples, which increased proportionally with nanotube diameter.[78] Differential ALP activity and OC expression patterns were found between the Aligned TiNT and Trabecular TiNT surfaces. ALP activity and OC expression was approximately constant on the Aligned TiNT surfaces after Day 3, yet progressively increased on Trabecular TiNT surfaces from Days 7 through 21. This may indicate that the cells require additional time to attach and proliferate on Trabecular TiNT, compared to Aligned TiNT surfaces, through the bone-like morphology of Trabecular TiNT may promote differentiation as OC expression and ALP activity increased throughout the later timepoints. Brammer, *et al*. discussed the limited

adherence of osteoblasts on titania nanotubes with 100 nm diameter, compared to the abundant cell adhesion on 30 nm-diameter nanotubes. As a result of the empty pores between the larger diameter arrays, osteoblasts initially attached to the top walls/features and then must extend filopodia to protein-deposited surfaces, resulting in greater cell elongation on larger diameter nanotube surfaces; however, over time, the surfaces with 100 nm diameter nanotubes produced the greatest ALP activity.[78] Gene expression analysis, focusing on three specific genes related to bone formation, demonstrated increased fold-change of TiNT surfaces over Control at multiple timepoints. Pozio, *et al.* also observed an upregulation of Col1a1 after a 14-day culture of human osteoblasts on titania nanotube surfaces, which later downregulated at a 30-day timepoint.[95]

Our study limitations involved difficulties with staining the TiNT surfaces, especially at timepoints greater than 4 hours. Because of the nanotopography and voids, which were ideal for cell attachment, stain penetration of the cells was complicated and incomplete. Also, in the qPCR analysis, we encountered difficulty removing the BMC seeded on TiNT samples. Despite adding additional time for Trypsin penetration and scraping samples, we were unable to effectively remove the cells, which subsequently required additional pre-amplification and introduced variability.

BMC were harvested from the intramedullary canals of long bones, including femora, of the same SD rat strain used in the *in vivo* study. In effect, the implant in our subsequent *in vivo* studies was then placed in the same location and environment as the cell harvest (Chapters 5 and 6). The titania nanotube surfaces were also challenged via the selection of BMC for the *in vitro* experiment, as the cells are not obligated to differentiate into osteoblasts and will only differentiate into osteoblasts under specific

conditions. Additionally, SD rats, an outbred rat strain was used to approximate the differential osseointegrative potential experienced in the human population. Our results indicate inherent cell attachment, cell viability, cell differentiation to an osteoblastic phenotype by 3 days, and cell proliferation over the course of the 21-day experiment. The *in vitro* results provided justification to pursue an *in vivo* study.

Chapter 5:

In Vivo Assessment of Biocompatibility Titania Nanotube Surfaces in a Rat Model of Intramedullary Fixation

5.1 Introduction

Using a clinically-relevant model of long-term femoral intramedullary implant in a rat to simulate joint arthroplasty, TiNT-etched implants were compared to unetched controls by assessing longitudinal animal weights, remote organ weights, metal ion levels in remote organs and whole blood, hematology, and undecalcified histology.[96] We hypothesize that TiNT surfaces will demonstrate equivalent biocompatible and non-toxic results, equivalent to unmodified titanium alloy substrate surfaces.

5.2 Experimental Methods

After preparing titanium alloy Kirschner wires (K-wire; Modern Grinding, Port Washington, WI; material=Ti-6Al-4V ELI Hard, diameter=1.25 mm, single trocar tip for insertion) according to the methods in Chapter 3, Aligned TiNT-etched, Trabecular TiNT-etched, or unetched titanium K-wire implants (n=6 per group) were inserted retrograde into the femoral intramedullary canals of SD rats for a single, long-term endpoint of 12 weeks.[97-99] Three naïve/nonoperative animals were housed for the same duration, in order to establish baseline characteristics. SD rats, an outbred strain, were selected to approximate differential outcomes in the human population. Throughout the study, the rats received daily veterinary care to identify complications and were

Material contained in this chapter is planned for journal submission.

weighed weekly. At endpoint, hematologic, metal ion, and histologic analyses were performed.

5.2.1 Implantation Procedure

Under an IACUC-approved protocol (Beaumont AL-14-04; MTU 680637), 14-week old, female SD rats were anesthetized [induction: intraperitoneal injection of ketamine (75-100 mg/kg) and xylazine (3-5 mg/kg); maintenance: inhaled isoflurane (1-2%)] and placed supine on a sterile, heated operating table. Each animal received unilateral femoral implants via retrograde insertion. Placing the knee in 45 degrees of flexion, a lateral parapatellar skin incision was created. Returning the limb to extension, the incision was extended over the femorotibial (knee) joint. The dissection was carried down through retinaculum and joint capsule, which were incised in line with the skin incision, allowed access to the distal femur. Adequate soft tissue off the patella was left to facilitate capsular repair. With the limb again in maximum flexion, the patella was retracted medially, and a shallow pilot hole was drilled in the intercondylar groove. Subsequently, the K-wire was inserted at the center of the intercondylar notch. With the aid of fluoroscopy, the K-wire was advanced to the distal end of the greater trochanter. The distal end of the K-wire was cut and tamped to avoid a proud implant (Figure 5.1). TiNT morphology was randomized just prior to surgery by nonoperative staff.

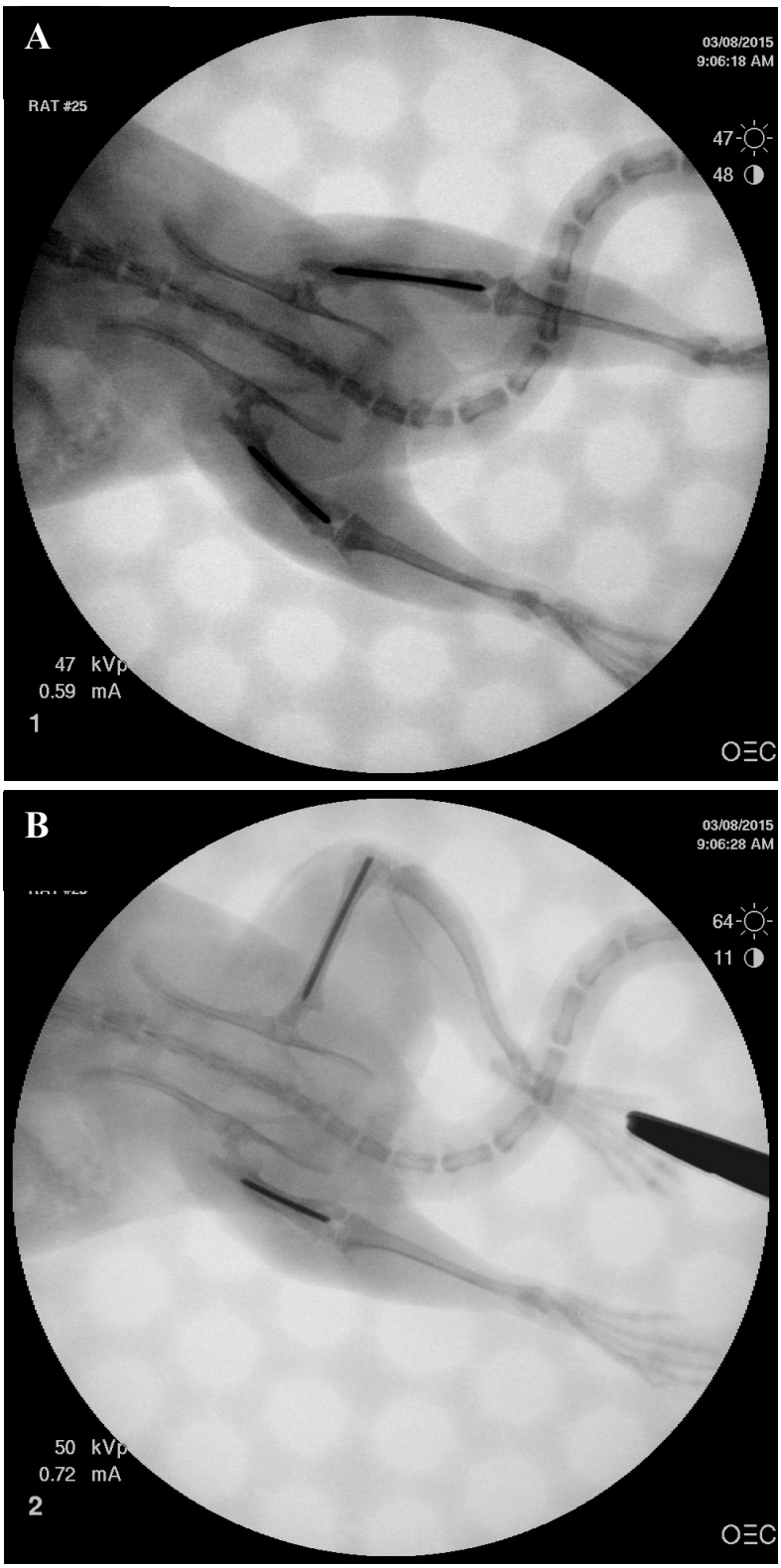

Figure 5.1. *Radiographs following bilateral Kirschner wire implantation. Representative (A) anteroposterior (A) and lateral (B) views from Rat 25 are shown.*

5.2.2 General Health Assessment

All rats were evaluated daily for clinical signs of complications and overall health, including pain level, activity level, and food/water consumption. Rats were weighed preoperatively and weekly throughout the experiment. At endpoint, remote organs (i.e. spleen, liver, lungs, kidneys, brain) were collected and weighed, as another assessment of animal health. A one-way ANOVA model was used to compare longitudinal animal weights and endpoint organ weights between treatment groups, with α=0.05.

5.2.3 Hematologic Analysis

At endpoint, each anesthetized rat underwent antemortem cardiac puncture to collect blood for hematologic analyses to quantify the following thirteen parameters associated with either systemic inflammation/infection or anemia status: white blood cell count (WBC), lymphocyte concentration (Lymph), monocyte concentration (Mono), granulocyte concentration (Gran), hematocrit (HCT), mean cell volume of red blood cells (MCV), red blood cell distribution width (RDWa), hemoglobin concentration (Hgb), mean cell hemoglobin concentration (MCHC), mean cell hemoglobin (MCH), red blood cell count (RBC), total platelet count (PLT), mean and platelet volume (MPV) (HemaTrue Hematology Analyzer, Heska, Loveland, CO). Blood was collected in vacutainer tubes with EDTA and immediately processed. A one-way ANOVA model was used to compare hematologic parameters between treatment groups, with α=0.05.

5.2.4 Metal Ion Analysis

Inductively coupled plasma mass spectrometry (ICP-MS; HP 4500 Series, Agilent Technologies, Santa Clara, CA) was used to measure the titanium, aluminum, and vanadium concentrations in each remote organ and a whole blood sample from each animal. ICP-MS calibration was performed using both ASTM standards of each target element as well as non-implanted samples of the K-wires from each testing condition. After the animals were euthanized, the remote organs (i.e. spleen, liver, lungs, kidneys, brain) were harvested, weighed, and then stored in ultra-low leachable sample tubes at 4°C. To dissolve any metal present in the organ tissues into an aqueous solution, samples were digested by adding a purified solution of HNO_3, HCl, H_2O_2, and water directly into sample tubes. Sample tubes were then heated at 95°C for 2 hours. After setting the final digested tissue volume at 40 mL per sample, the homogenized samples were diluted 10-fold and analyzed for titanium, aluminum, and vanadium concentration (ng of metal/g of sample). Samples were analyzed in tandem with a laboratory reagent blank and duplicate laboratory fortified blanks to quantify background metal levels as well as procedure accuracy and precision, respectively. A one-way ANOVA model was used to compare metal ion levels between treatment groups, with α=0.05.

5.2.5 Undecalcified Histologic Analysis

At study endpoint, implanted femora were also harvested for undecalcified histologic analysis. Femora from each animal were stripped of soft tissues and placed in formalin for 96 hours, followed by three rinses in phosphate buffered saline, and ethanol storage to prepare for histologic processing. Femora were subsequently embedded in methyl

methacrylate, then ground and polished longitudinally to the approximate center of the implant, followed by cutting and applying one 5 µm thick section to a slide. Each slide was stained with Stevenel's Blue and van Gieson picrofuchsin (SBVG) for visualization of fibrous and mineralized tissue as well as the presence of immune-related cellular activity. SBVG is a widely-used stain to assess bone formation, due to visualization of both mature bone and osteoid as well as fibrous tissue, which may signify inferior osseointegration and/or increased inflammatory response, especially at the bone-implant interface.[100-102] Stained sections were manually scanned at a magnification of 20x (90i, Nikon Instruments, Inc., Melville, NY) to facilitate both high-magnification and whole-mount analyses. Three 20x regions of interest (ROI) per location (i.e. distal, midshaft, proximal) per section were captured. Within each ROI, five cell types were identified: foreign body giant (FBG)/multinucleated cell, granulocyte (non-neutrophilic, including eosinophils and basophils), neutrophil, monocyte, and lymphocyte. Cell constituents within each ROI were then graded on a scale of 0 to 2, with 0=no cells, 1=cells comprising ≥25% of field, and 2=cells comprising ≥50% of field. For FBG/multinucleated or granulocyte, a Grade 2 was defined as three or more cells per field. Grades were statistically compared between TiNT groups and Control, using a Mann-Whitney Rank Sum Test, with α=0.05.

5.3 Results

Over the 12-week study, animals gained an average of 148 g, with Control animals gaining the most weight on average (179 g) and Trabecular TiNT animals gaining the least on average (118 g) (Figure 5.2A). No animals lost more than 10% body

weight, our institutional trigger for intervention. At Week 9, the Aligned TiNT group weighed significantly more than the Trabecular TiNT group (p=0.013), and at Week 11, the Control group weighed significant more than the Trabecular TiNT group (p=0.023). There were no significant differences at any other weekly time points. Mass of the spleen, brain, kidneys, lungs, and liver were obtained, and there were no significant differences between any groups for the specimens (Figure 5.2B).

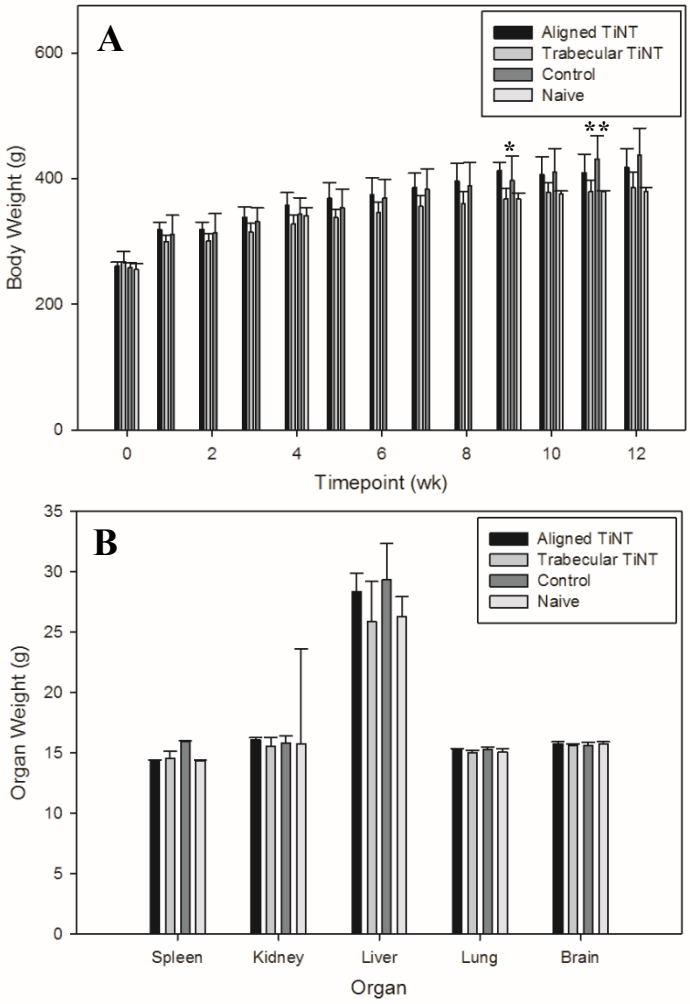

Figure 5.2. *Animal body (weekly) and remote organ weights (endpoint) were measured. These weights are one means to assess general health. Average animal (A) body weight and (B) organ weight per group over the 12-week study are presented.*Week 9: Aligned TiNT vs. Trabecular TiNT, p=0.013; **Week 13: Trabecular TiNT vs. Control, p=0.023.*

Hematologic analysis was performed, and no significant associations were found between any groups for any parameters (Tables 5.1 and 5.2).

Table 5.1. *Hematologic analysis of white blood cell function at endpoint. Average values are shown for each treatment group.**

Group	WBC	Lymph	Mono	Gran	Lymph%	Mono%	Gran%
Aligned TiNT	9.5 (2.7)	7.3 (1.8)	0.4 (0.2)	1.7 (0.7)	77.9 (2.7)	3.9 (1.3)	18.2 (2.6)
Trabecular TiNT	8.02 (3.5)	6.2 (2.7)	0.3 (0.1)	1.5 (0.8)	77.9 (3.9)	3.3 (1.6)	18.8 (2.9)
Control	8.9 (2.2)	7.0 (1.6)	0.3 (0.1)	1.5 (0.6)	79.7 (2.5)	3.1 (0.8)	17.3 (2.2)
Naïve	11.0 (6.1)	8.4 (3.9)	0.5 (0.4)	2.1 (1.8)	79.1 (6.1)	3.1 (0.8)	17.8 (5.3)

* Standard deviation listed in parentheses; WBC=white blood cell count, Lymph=lymphocyte concentration, Mono=monocyte concentration, Gran= granulocyte concentration

Table 5.2. *Hematologic analysis of red blood cell function at endpoint. Average values are shown for each treatment group.**

Group	HCT	MCV	RDWa	RDW%	Hgb	MCHC	MCH	RBC	PLT	MPV
Aligned TiNT	40.1 (3.2)	49.7 (1.1)	32.8 (1.0)	16.4 (0.5)	15.3 (1.2)	38.3 (0.5)	19.0 (0.3)	8.1 (0.6)	318.7 (149.4)	6.4 (0.8)
Trabecular TiNT	38.3 (1.5)	50.0 (0.9)	32.9 (0.7)	16.4 (0.6)	14.6 (0.4)	38.3 (0.6)	19.1 (0.5)	7.7 (0.4)	275.8 (151.6)	6.7 (0.6)
Control	40.1 (3.5)	50.9 (1.2)	34.0 (1.6)	16.4 (0.4)	15.1 (1.2)	37.7 (0.5)	19.1 (0.4)	7.9 (0.6)	335.0 (89.7)	6.4 (0.5)
Naïve	41.4 (2.8)	50.6 (0.8)	33.7 (0.2)	16.5 (0.4)	15.6 (1.1)	37.7 (0.2)	19.1 (0.3)	8.2 (0.5)	305.7 (93.5)	6.1 (0.8)

* Standard deviation listed in parentheses; HCT=hematocrit, MCV=mean cell volume of red blood cells, RDWa=red blood cell distribution width, Hgb=hemoglobin concentration, MCHC=mean cell hemoglobin concentration, MCH=mean cell hemoglobin, RBC=red blood cell count, PLT=total platelet count, MPV=mean and platelet volume

Titanium, aluminum, and vanadium levels of each implant type (e.g. Aligned TiNT, Trabecular TiNT, Control) were analyzed to quantify the effect of the etching process on chemistry (Table 5.3). Compared to Control, Aligned TiNT and Trabecular TiNT demonstrated greater aluminum and vanadium content and lower titanium content, by wt%.

Table 5.3. *Comparison of alloy composition between groups. Data was quantified via inductively coupled plasma mass spectrometry.*

Group	Element	Composition (wt%)
Aligned TiNT	Titanium	86.036
	Aluminum	7.032
	Vanadium	6.933
Trabecular TiNT	Titanium	86.744
	Aluminum	6.958
	Vanadium	6.298
Control	Titanium	89.238
	Aluminum	6.455
	Vanadium	4.308

After weighing each organ, metal concentration in each organ and whole blood were assessed. Aluminum levels in the lungs were significantly greater in the Trabecular TiNT group compared to Control ($p=0.022$). No other organs exhibited significantly increased titanium, aluminum, or vanadium levels compared to Control (Figure 5.3).

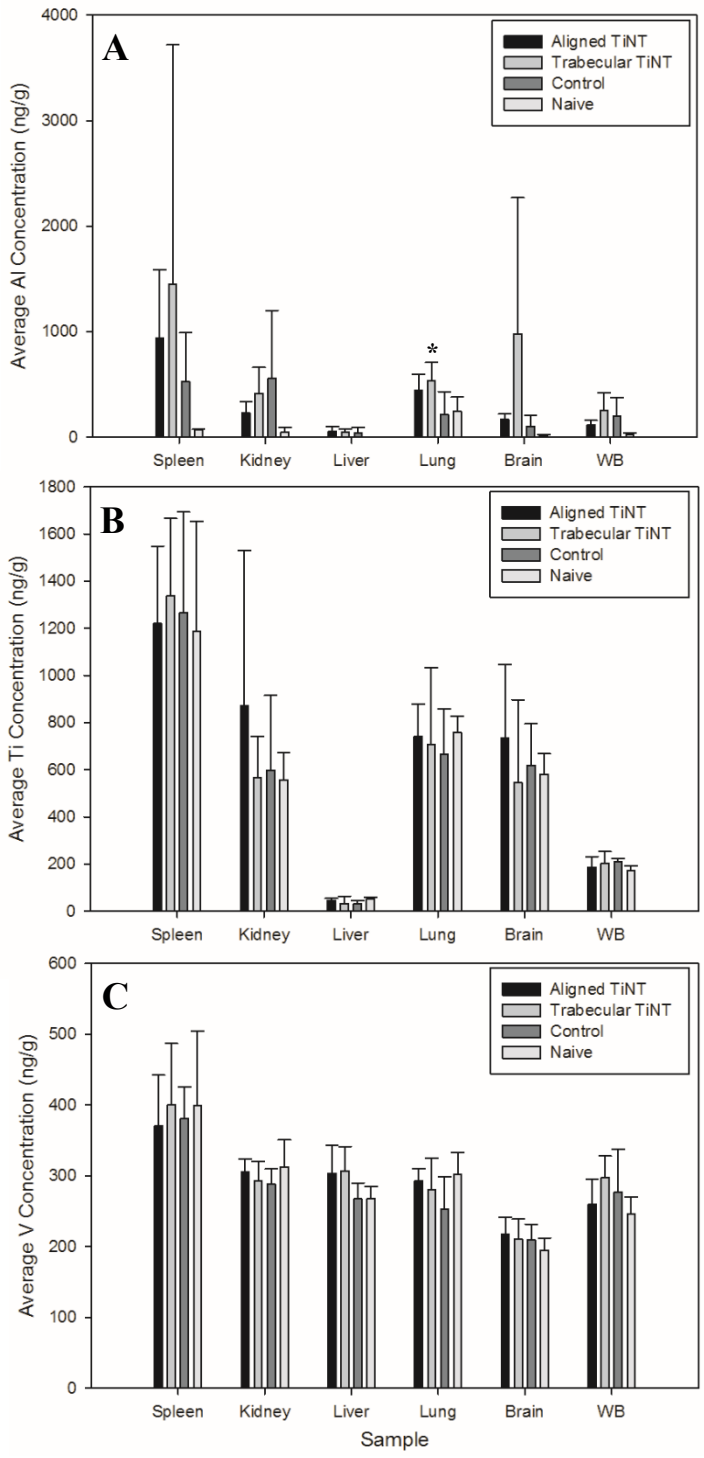

Figure 5.3. *Metal ion concentration in remote organs and whole blood for each group. of The three metals assayed were (A) aluminum, (B) titanium, and (C) vanadium, the constituents of the alloy used throughout the study. (WB=whole blood). *Aluminum: Trabecular TiNT vs. Control, p=0.022.*

Histologic analysis demonstrated a lack of inflammatory infiltrate in proximity to the nails within the intramedullary space, for all groups (Table 5.4). There were significantly less eosinophils/basophils and neutrophils in the Distal ROI of the femora implanted with Trabecular TiNT-etched implants ($p=0.040$ and $p=0.019$, respectively). In the Midshaft ROI, there were significantly less foreign body giant/multinucleated cells and neutrophils in the Aligned TiNT group ($p=0.039$ and $p=0.019$, respectively). There were no observed necrotic or cytotoxic events observed within the marrow cavity of any of the animals (Figure 5.4).

Table 5.4. *Average histologic grade for three regions of interest in each group.**

ROI	Group	Foreign Body Giant/ Multinucleated	Granulocyte	Neutrophil	Monocyte	Lymphocyte
Distal	Trabecular TiNT	0.833 (1.0)	**0.056 (0.0)**	**0.722 (1.0)**	0.778 (1.0)	1.111 (1.0)
	Aligned TiNT	0.722 (1.0)	0.222 (0.0)	1.056 (1.0)	0.778 (1.0)	1.056 (1.0)
	Control	0.556 (0.5)	0.333 (0.0)	1.000 (1.0)	0.722 (1.0)	1.222 (1.0)
Midshaft	Trabecular TiNT	0.500 (0.5)	0.611 (1.0)	1.000 (1.0)	0.556 (1.0)	1.222 (1.0)
	Aligned TiNT	**0.389 (0.0)**	0.833 (1.0)	**0.722 (1.0)**	0.667 (1.0)	1.056 (1.0)
	Control	0.778 (1.0)	0.722 (1.0)	1.000 (1.0)	0.722 (1.0)	1.222 (1.0)
Proximal	Trabecular TiNT	0.833 (1.0)	0.611 (1.0)	0.944 (1.0)	0.778 (1.0)	1.389 (1.0)
	Aligned TiNT	0.722 (1.0)	0.444 (0.0)	1.056 (1.0)	0.889 (1.0)	1.278 (1.0)
	Control	0.722 (1.0)	0.722 (1.0)	1.000 (1.0)	0.833 (1.0)	1.444 (1.0)

*Median values listed in parentheses; Statistically significant values bolded. Cell constituents within each ROI were then graded on a scale of 0 to 2, with 0=no cells, 1=cells comprising ≥25% of field, and 2=cells comprising ≥50% of field. For FBG/multinucleated or granulocyte, a Grade 2 was defined as three or more cells per field.

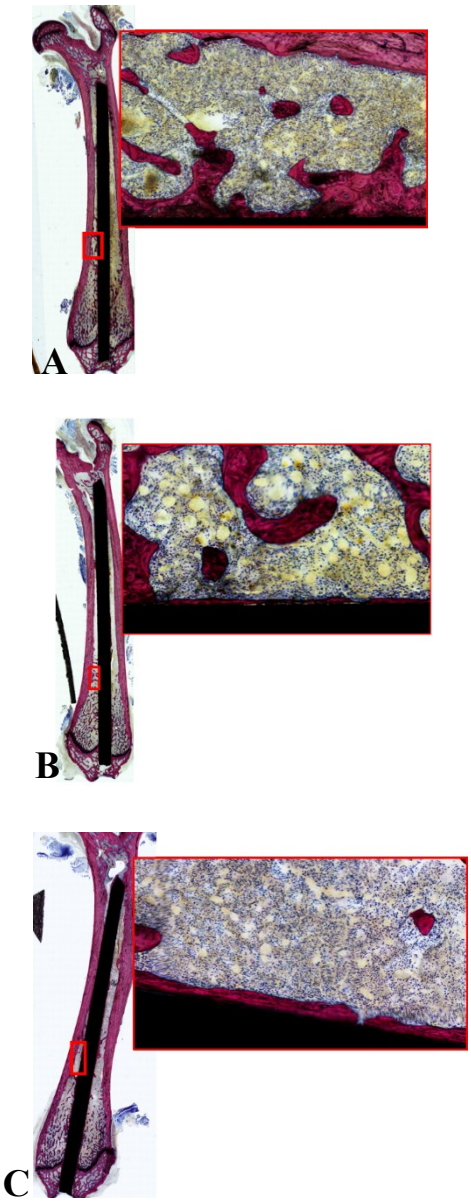

Figure 5.4. *Histologic sections and regions of interest of representative femora. Representative images from longitudinal histologic sections of Aligned TiNT (A), and Trabecular TiNT (B), and Control (C) groups are illustrated.*

5.4 Discussion and Conclusions

We evaluated the biocompatibility of Aligned and Trabecular TiNT surfaces via a clinically-relevant *in vivo* study of biologic response to implant materials. The *in vivo* study included multiple characterization methods, including a general health assessment (e.g. body weight) as well as hematologic, metal ion, and histologic analyses.

In this study, no interventions were required for disease or weight loss (institutional policy allows ≤20% weight loss, based on initial body weight), throughout the experiment. There were several significant differences in body weight between groups at two weeks during the experiment, however, the body weights recovered and were not an established trend. At endpoint, remote organ masses were compared between groups, and these also showed no significant difference.

When metal ion concentration was assessed in remote organ and whole blood samples, aluminum levels were significantly increased in the lungs of the rats implanted with Trabecular TiNT-etched K-wires compared to Controls. No other organs or whole blood samples showed significantly elevated metal levels, when the experimental groups were compared to Control. A study of intraarticular injection of TiO_2 nanoparticles (45 nm average diameter; 0.2, 2, 20 mg/kg TiO_2 in suspension) into rat knee joints showed nanoparticle migration to remote organs as well as pathologic changes in the heart, lung, liver, and knee at 7 days post-injection.[103] Although our study showed metal particle concentration in remote organs via ICP-MS and did not histologically-assess remote organs, we theorize that the amount of TiO_2 particulate debris shed in the rat femora was less than 0.2 mg/kg.

At study endpoint, no hematologic markers of white and red blood cell function, which would signal systemic inflammation-, infection-, or anemia-related complications, were significantly elevated in the experimental groups compared to Control. Histologic analysis showed several significant differences in cell populations between the TiNT groups and Control, with less foreign body giant/multinucleated, eosinophil/basophil, and neutrophil cell activity in TiNT-implanted femora than Control. There were no significant differences in monocyte and lymphocyte activity between the TiNT groups and Control.

In *in vitro* and *in vivo* studies of vascular toxicity, Bayat, *et al.* established that titania nanotubes with 30nm diameter as well as ultra-small TiO_2 nanoparticles (1-3 nm) were not cytotoxic and nanoparticles did not possess oxidative potential.[104] *In vivo* studies in rat models have also shown that TiO_2 nanoparticles are not genotoxic.[105, 106] Neacsu, *et al.* showed that after seeding murine macrophages onto TiNT and unetched titania surfaces under pro-inflammatory and standard conditions, inflammatory activity related to cytokine and chemokine gene expression, foreign body giant cell production, and nitric oxide release all decreased on TiNT surfaces but not on unetched controls. The authors suggested that the TiNT surfaces may regulate macrophage response thereby diminishing the overall inflammatory cascade,[107] a comparable finding in a study where leukocytes were seeded on TiNT surfaces.[108] Another study showed increased adsorption of blood serum protein, platelet adhesion and activation, and clotting of whole blood as well as no evidence of monocyte activation and cytokine secretion on TiNT surfaces versus control.[109]

Previous reports have demonstrated the biocompatibility of TiNT surfaces and correspond with our findings that TiNT surfaces do not initiate systemic effects in a

clinically-relevant, *in vivo* model of simulated joint arthroplasty, which would impact body and organ weights, hematologic parameters, and result in observable deficits and/or complications in the study animals.

Chapter 6:

In Vivo Assessment of Osseointegration of Titania Nanotube Surfaces in a Rat Model of Intramedullary Fixation

6.1 Introduction

Titanium alloy Kirschner wires (K-wire; Modern Grinding, Port Washington, WI; material=Ti-6Al-4V ELI Hard, diameter=1.25 mm, single trocar tip for insertion) were etched with Aligned or Trabecular TiNT and inserted retrograde into the femoral intramedullary canals of SD rats.[97-99] This outbred strain was selected to approximate differential osseointegrative capabilities and outcomes in the human population. Two endpoints, 4 weeks and 12 weeks, were included to compare the rate of periprosthetic bone formation and osseointegration. Multiple characterization methods, including biomechanical testing, microcomputed tomography (μCT), backscattered electron imaging (BEI), and undecalcified histology, were performed. For all data, the ratio between the experimental (Aligned TiNT or Trabecular TiNT) and Control femora were calculated for each bilateral pair and averaged for each morphology at each endpoint.

6.2 Experimental Methods

6.2.1 Implantation Procedure

Under an IACUC-approved protocol (Beaumont AL-14-04; MTU 680637), K-wire implants were implanted, as described in Chapter 5. One limb received an unetched titanium K-wire, while the other limb received either an Aligned TiNT- or Trabecular

Material contained in this chapter is planned for journal submission.

TiNT-etched K-wire. TiNT morphology was randomized just prior to surgery by nonoperative staff, with eight animals per morphology per endpoint. Following surgeries, animals were randomized to endpoint and characterization cohorts. Characterization cohorts were "Imaging" (μCT, backscattered imaging, and histology; three animals per morphology per endpoint) and "Biomechanics" (five animals per morphology per endpoint).

6.2.2 Imaging Analysis

For animals randomized to the Imaging cohort (μCT, BEI, and histology), femora were harvested at each endpoint, stripped of extraneous tissues, and placed in 10% neutral buffered formalin for a minimum of 96 hours to allow for formalin penetration and tissue fixation (n=3 paired femora per group per timepoint).

6.2.2.1 Microcomputed Tomography Analysis

After 96 hours, each femur was rinsed with saline three times in a 24-hour period, then wrapped in saline-soaked towel and placed in a "wet" sample tube for μCT scanning (μCT-40, Scanco USA, Wayne, PA). Scans were performed using a voltage of 70 kVp, current of 114 μA and a 300 ms integration time, yielding a 16 μm isotropic voxel size. Two scan regions, 190 slices of the midshaft (i.e. Midshaft volume of interest) and 127 slices just proximal to the physis (i.e. Distal volume of interest) were selected. All analyses were performed with the Scanco onboard evaluation software.[98, 110, 111] Alignment of each sample in the z-axis using the center of the implant as a reference was performed, followed by reimporting of revised stacks. Contours were generated for each

volume of interest (VOI) by applying contours to the first and last valid slices and interpolating between these slices, with correction as needed. For the Midshaft VOI, a freeform outline was applied circumferentially to the interface of the cortical shell and intramedullary canal, and then iterated forward from first to last slice. For the Distal VOI, an ellipse (110 pixels x 110 pixels) was applied to each slice. A segmentation process was performed to determine lower thresholds for the implant and bone as well as dilation distance, using four specimens per endpoint (n=2 with TiNT morphology, n=2 Control) (Figure 6.1).

The average of the lower threshold values determined in the segmentation process as well as the dilation distance that minimized beam hardening artifact were applied to all specimens in the final evaluation process.[110] Total bone volume (TBV) and bone volume per total volume (BV/TV; bone volume fraction) per slice and per VOI were obtained. Histomorphometric parameters, quantitative measures of *de novo* bone quality, were also collected, including connectivity density (Conn.D; measure of trabeculae connectivity normalized by total volume, $1/mm^3$), structure model index (SMI; descriptor of trabeculae structure and presented as absolute value in this data set, 0=parallel plates and 3=cylindrical rods), trabecular number (Tb.N; average number of trabeculae per length, 1/mm), trabecular thickness (Tb.Th; average thickness of trabeculae, mm), trabecular separation (Tb.Sp; average distance between trabeculae, mm), volume mineral density (VMD; mineralization density of bone tissue only, mg/cm^3 of hydroxyapatite), and bone mineral density (BMD; mineralization density of entire volume, both bone and non-bone tissue, mg/cm^3 of hydroxyapatite).[110]

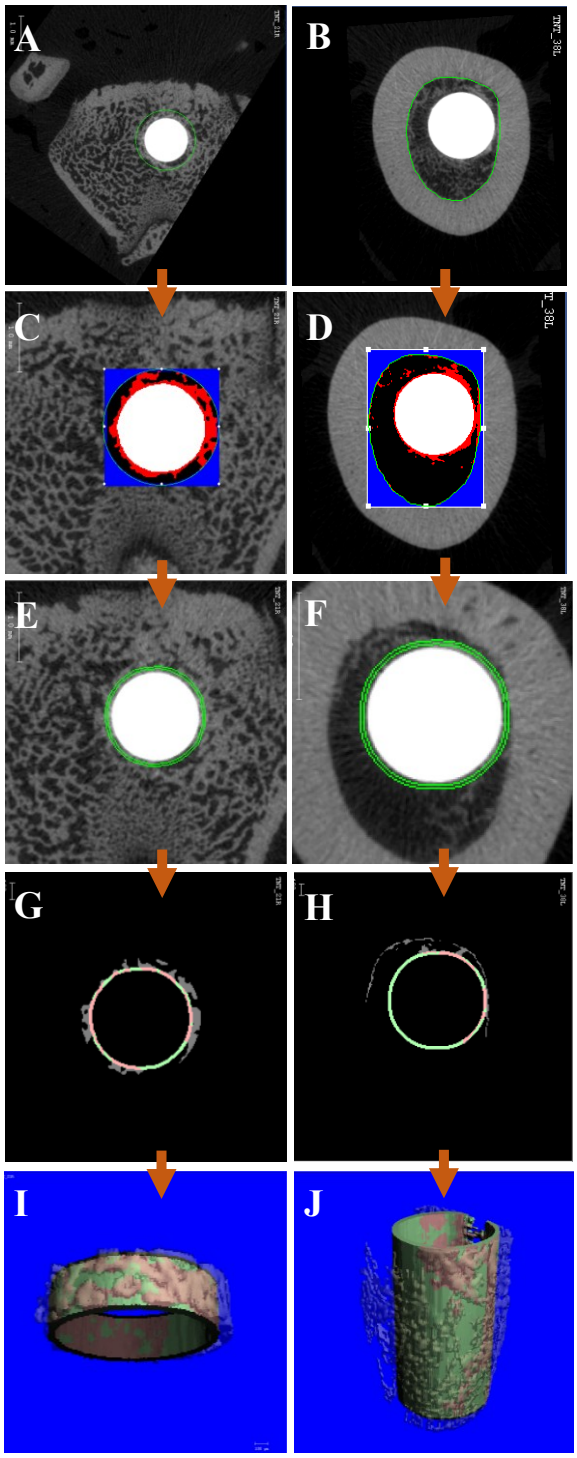

Figure 6.1. *Image processing of μCT scans for Distal and Midshaft volumes of interest (VOIs). Distal and Midshaft VOIs are presented in the left and right columns, respectively. (A,B) Contouring, (C,D) segmentation of implant and bone, (E,F) assigning dilation distance, (G,H) two-dimensional visualization of bone-implant contact, and (I,J) three-dimensional reconstruction with bone-implant contact are shown. Femora 21R and 38L were used for Distal and Midshaft VOIs, respectively.*

6.2.2.2 Backscattered Electron Analysis

After μCT, specimens were placed in 70% ethanol for BEI and histologic analysis.[112] Femora were subsequently embedded in methyl methacrylate, then ground and polished longitudinally to the approximate center of the implant. These longitudinal sections were marked at 5 mm and 15 mm proximal to the femoral notch to guide Distal and Midshaft region of interest (ROI) selection, respectively, for imaging in an environmental scanning electron microscope (SEM; Vega3XMU, Tescan USA, Warrendale, PA) using a lanthanum hexaboride (LaB6) filament and the onboard backscattered electron detector. Imaging was performed with a 20 kV accelerating voltage and 15 mm working distance, under low pressure (10 Pa) to minimize sample charging. Identical magnification, contrast/brightness and beam intensity were used to ensure consistency in field of view size and grayscale values between specimens. Images were then imported into evaluation software (ImageJ, National Institutes of Health, Bethesda, MD) for quantification of bone at the implant interface. For the Midshaft ROI, quantification of bone contact at the interface furthest from the cortical shell was obtained, while the Distal ROI was quantified on both interfaces of the implant. A segmentation process using four specimens per endpoint (n=2 with each TiNT morphology, n=2 Control) was completed to establish minimum and maximum thresholds for bone. The average of these respective threshold values was applied to all specimens in the final imaging analysis. In the Midshaft ROI, three zones were defined in the portion of the intramedullary canal furthest from the cortical shell at one, two, and three pixels away from the implant. Six zones were placed in the Distal ROI at one, two, and three pixels from the implant interface, with three zones on each side of the implant

interface. After entering threshold values, the particle (bone) count, average particle (bone) size, total particle (bone) area, and percentage of particle (bone) area for each zone was obtained. Additionally, the fraction of bone-implant contact across the entire image was calculated from line profiles for each ROI at one, two, and three pixels from the implant interface. The ratio between the paired experimental and Control femora of each parameter was calculated for each bilateral pair and averaged for each morphology at each endpoint.

6.2.3 Undecalcified Histologic Analysis

At the conclusion of BEI, the blocks were prepared for final undecalcified histologic processing. Each block was gently ground and polished, before cutting and applying one 5 μm thick section to a slide. Each slide was then stained with Stevenel's Blue and van Gieson picrofuchsin (SBVG) for visualization of mature bone (red), osteoid (green or gray/green), and collagen/fibrous tissue (blue) at the bone-implant interface. SBVG is a widely-used stain to assess bone formation, due to visualization of both mature bone and osteoid as well as fibrous tissue, which may signify biocompatibility issues, inferior osseointegration, and/or increased inflammatory response, especially at the bone-implant interface.[100-102] Stained sections were manually scanned at a magnification of 20x (90i, Nikon Instruments, Inc., Melville, NY) to facilitate both high-magnification and whole-mount analyses. Manual analysis was performed to quantify periprosthetic bone formation by measuring and then dividing the length of each segment of bone-implant contact along the entire length of the implant and the entire length of the implant to calculate the bone-implant contact fraction. Ratios between the experimental

and Control femora of bone-implant contact fraction were calculated, and averaged for each morphology at each endpoint.

6.2.4 Biomechanical Analysis

At experiment endpoint, the femora of animals randomized to biomechanical testing were dissected from each limb, stripped of extraneous soft tissues, wrapped in saline-soaked gauze, and stored at -20°C until testing. Femora were thawed overnight at 2 to 4°C, then immersed in phosphate buffered saline for 2 hours to rehydrate. After towel-drying the femora, a rotary tool fitted with a grinding attachment (Dremel, Mount Prospect, IL) was used to remove the proximal third of the femora to expose 4 to 5 mm of the K-wire. Using an electromechanically-actuated materials testing system (Insight 150, MTS, Eden Prairie, MN) with a custom-designed and fabricated fixture, bone-implant strength was assessed via a wire pull-out test. For each femur, the K-wire was secured in a drill chuck, which was anchored to the fixture and testing frame, while the distal portion of the femora was fixed in polyester resin (Bondo, 3M, St. Paul, Minnesota) within the fixture and attached to the base of the frame (Figure 6.2).

Figure 6.2. *Custom-designed and fabricated fixture for biomechanical testing. Photograph was obtained just prior to wire pull-out.*

For each test, the program ramped to 10 N at 0.25 mm/s, held for 20 s (pre-load), and then loaded to failure at 2 mm/min and the force required to remove the implant from the bone was recorded. Data collected during the test, at a sampling rate of 100 Hz, was used to create axial force-displacement curves. From the resultant curves, strength of fixation was calculated according to the equation

$$\sigma_u = \frac{F_{max}}{\pi \cdot D \cdot H} \qquad \textit{Eq. 4}$$

where σ_u=strength of fixation (MPa), F_{max}=maximum pull-out force (to loosen implant) (N), D=implant diameter (mm), and H=bone length after dissection (mm). This equation accounted for individual post-dissection bone length (H), which therefore addressed differences in pull-out force due to bone-implant fixation as a function of the length of

each bone.[99] Maximum failure load and strength of fixation data were compared between groups using a two-way analysis of variance (ANOVA, Factor A: group, Factor B: endpoint), with a Tukey post-hoc correction and α=0.05. Several K-wires were imaged after biomechanical testing to document bone ongrowth.

6.3 Results

To assess intramedullary fixation, K-wires etched with Aligned TiNT or Trabecular TiNT were compared to an internal Control, an unetched K-wire.

μCT, backscattered electron imaging, and histology were performed on each femora after harvesting at the specified endpoint for animals randomized to the Imaging cohort. For μCT, a segmentation process was performed to determine lower thresholds for the implant and bone as well as dilation distances, using four specimens per endpoint. The lower thresholds obtained during the segmentation process were averaged and used in the final evaluations. For the Distal VOI, the implant threshold was 722 Hounsfield units and the bone threshold was 363 Hounsfield units. For the Midshaft VOI, the implant threshold was 791 Hounsfield units and the bone threshold was 347 Hounsfield units. Hounsfield units are a measure of the radiodensity, or X-ray attenuation, of the implant and bone tissue relative to water. Materials and tissues that absorb more X-rays than water, including bone, have greater Hounsfield units.[113] Optimal dilation distance of 3 to 6 voxels from the outside diameter of the K-wire was determined, after using a post-processing algorithm to minimize beam hardening artifacts.[112, 114]

After segmentation, the onboard bone-implant contact program was used to calculate the total bone volume and bone volume fraction in each two-dimensional slice,

and subsequently per VOI. The ratio between the experimental (Aligned TiNT or Trabecular TiNT) and Control femora were calculated for each bilateral pair, and averaged for each morphology at each endpoint (Figures 6.3 and 6.4). Histomorphometric analysis was also performed to assess bone quality characteristics of the periprosthetic bone (Table 6.1).

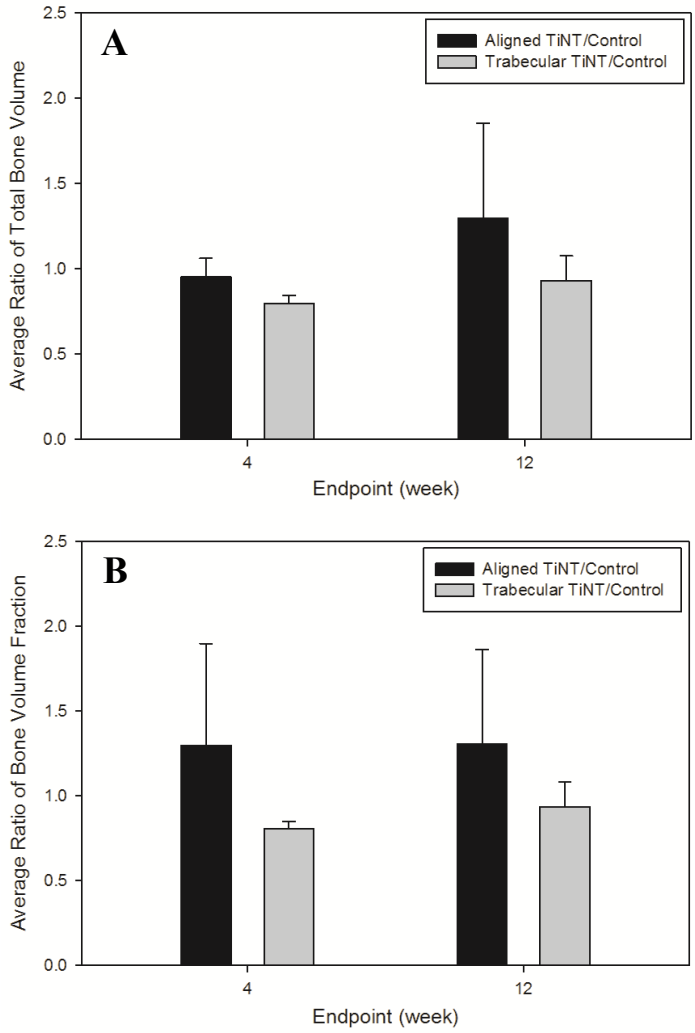

Figure 6.3. *Average total bone volume and bone volume fraction in the Distal volume of interest (VOI). Data was collected and processed via μCT. The (A) total bone volume and (B) bone volume fraction of the Distal volume of interest are presented as ratios between TiNT morphology and Control.*

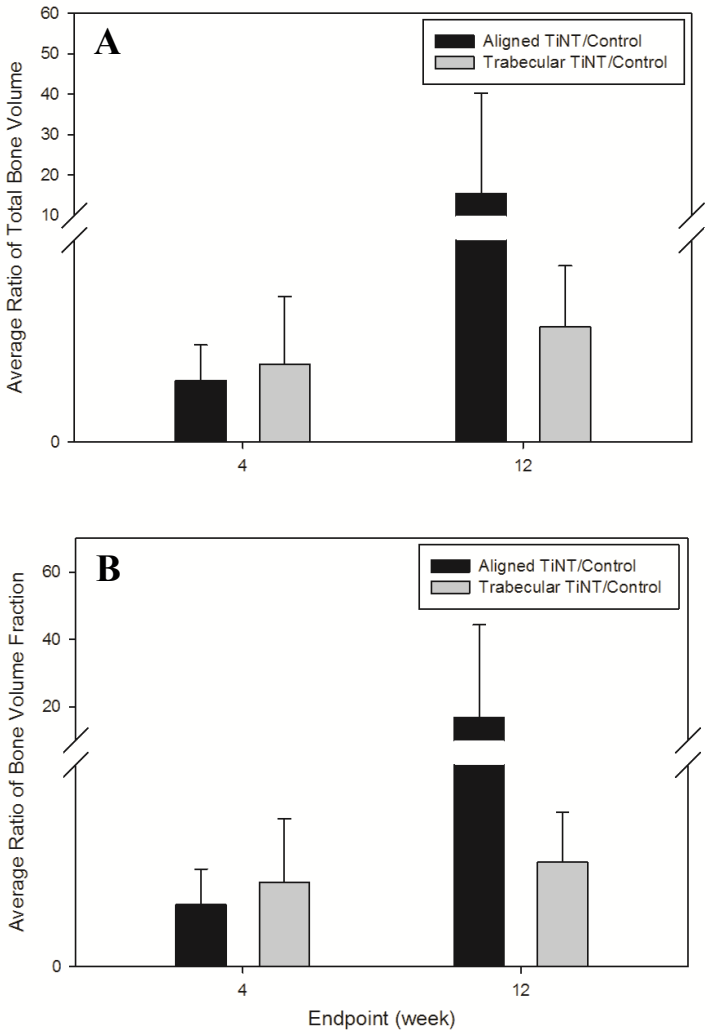

Figure 6.4. *Average total bone volume and bone volume fraction in the Midshaft volume of interest (VOI). Data was collected and processed via μCT. The (A) total bone volume and (B) bone volume fraction of the Midshaft volume of interest are presented as ratios between TiNT morphology and Control.*

Table 6.1. *Average histomorphometric parameters of femora. Data is presented as ratios of TiNT-implanted femora versus internal Controls in Distal and Midshaft volumes of interest. Data was collected and processed via μCT.**

Group	VOI	Endpoint (week)	Conn.D	SMI**	Tb.N	Tb.Th	Tb.Sp	VMD	BMD
Trabecular TiNT/ Control	Distal	4	1.24 (0.58)	1.18 (1.23)	0.97 (0.06)	1.00 (0.05)	1.23 (0.42)	0.97 (0.05)	1.00 (0.02)
		12	1.13 (0.51)	1.10 (0.71)	0.96 (0.05)	1.03 (0.11)	1.02 (0.01)	1.04 (0.16)	1.00 (0.02)
	Midshaft	4	1.27 (0.67)	1.02 (0.32)	0.84 (0.57)	0.98 (0.22)	1.73 (1.25)	0.90 (0.29)	0.99 (0.09)
		12	2.10 (1.44)	0.77 (0.08)	1.55 (0.22)	1.28 (0.04)	0.65 (0.07)	1.40 (0.24)	0.97 (0.02)
Aligned TiNT/ Control	Distal	4	1.51 (0.57)	17.53 (25.93)	1.08 (0.15)	1.05 (0.22)	0.89 (0.14)	1.09 (0.12)	1.01 (0.01)
		12	1.10 (0.43)	1.02 (1.44)	1.01 (0.10)	1.23 (0.42)	0.95 (0.20)	1.21 (0.33)	1.02 (0.04)
	Midshaft	4	1.44 (0.49)	0.85 (0.24)	1.19 (0.11)	1.07 (0.27)	0.85 (0.05)	1.03 (0.09)	0.95 (0.01)
		12	71.29 (120.88)	0.92 (0.69)	1.22 (0.28)	1.97 (1.33)	0.89 (0.18)	1.46 (0.38)	0.98 (0.07)

*Standard deviation listed in parentheses, **Absolute value of the SMI presented. Conn.D=connectivity density, SMI=structure model index, Tb.N=trabecular number, Tb.Th=trabecular thickness, Tb.Sp=trabecular separation, VMD=volume mineral density, BMD=bone mineral density

For BEI analysis of Distal and Midshaft regions of interest (ROI), images were imported into evaluation software. For the Distal ROI, the threshold minimum and maximum values were 29096 and 38555 pixels, while the threshold values for the Midshaft ROI were 28479 and 26883 pixels. Ratios between bone area and bone-implant contact fraction (average percentage of bone-implant contact) at each ROI were calculated (Figure 6.5 and Table 6.2, respectively). Line profiles showing the highly

variable differences in bone-implant contact between the TiNT-implanted and Controls were also plotted (Figures 6.6 and 6.7).

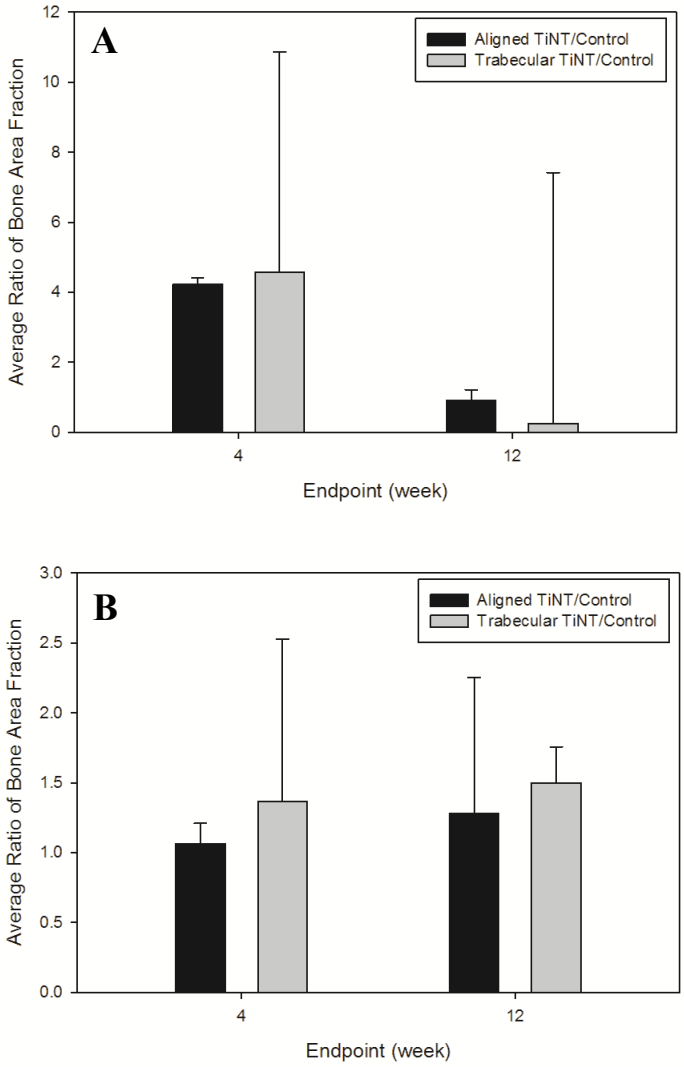

Figure 6.5. *Bone area fraction in the Midshaft and Distal regions of interest. Data is presented as ratios between TiNT-implanted femora and respective internal Controls in the (A) Midshaft and (B) Distal regions of interest at 4- and 12-week endpoints.*

Table 6.2. *Average bone-implant contact fraction ratios. Data is presented for the Distal and Midshaft regions of interest.**

Region of Interest	Endpoint (week)	Trabecular TiNT/Control	Aligned TiNT/Control
Midshaft	4	0.93 (0.19)	5.01 (8.65)
	12	0.21 (0.18)	0.90 (0.42)
Distal	4	1.68 (1.74)	1.06 (0.07)
	12	1.42 (0.12)	1.29 (1.02)

* Standard deviation listed in parentheses

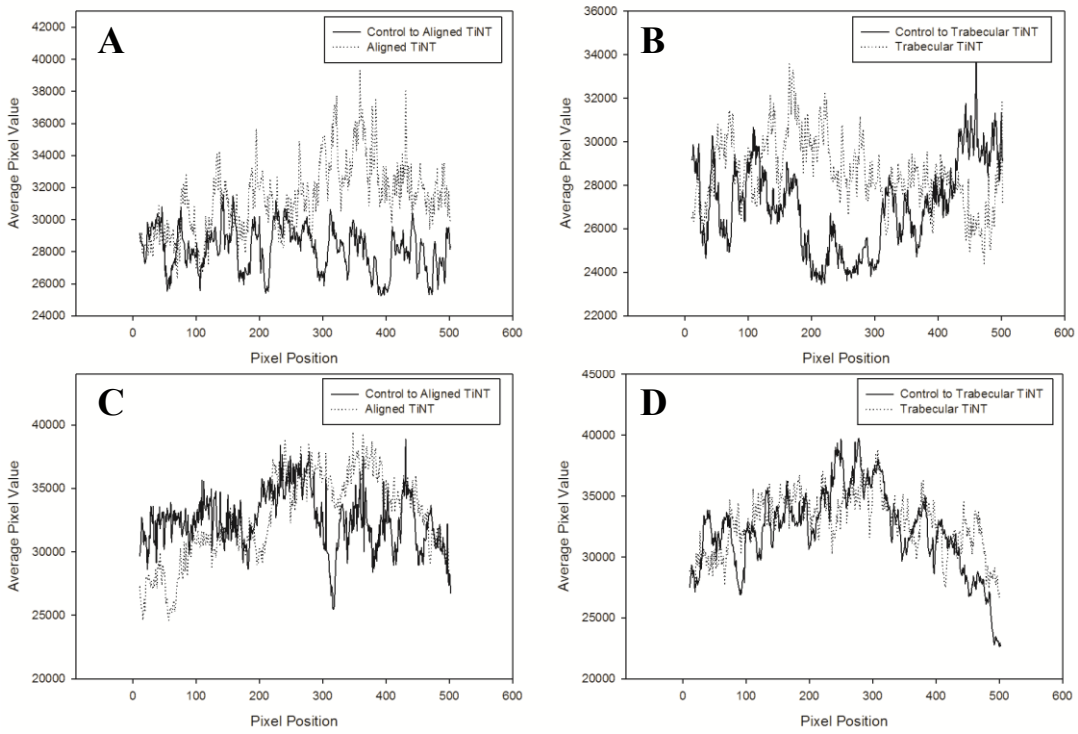

Figure 6.6. *Line profiles in the Midshaft region of interest. Profiles presented are internal Controls versus (A) Aligned TiNT at 4 weeks, (B) Trabecular TiNT at 4 weeks, (C) Aligned TiNT at 12 weeks, and (D) Trabecular TiNT at 12 weeks.*

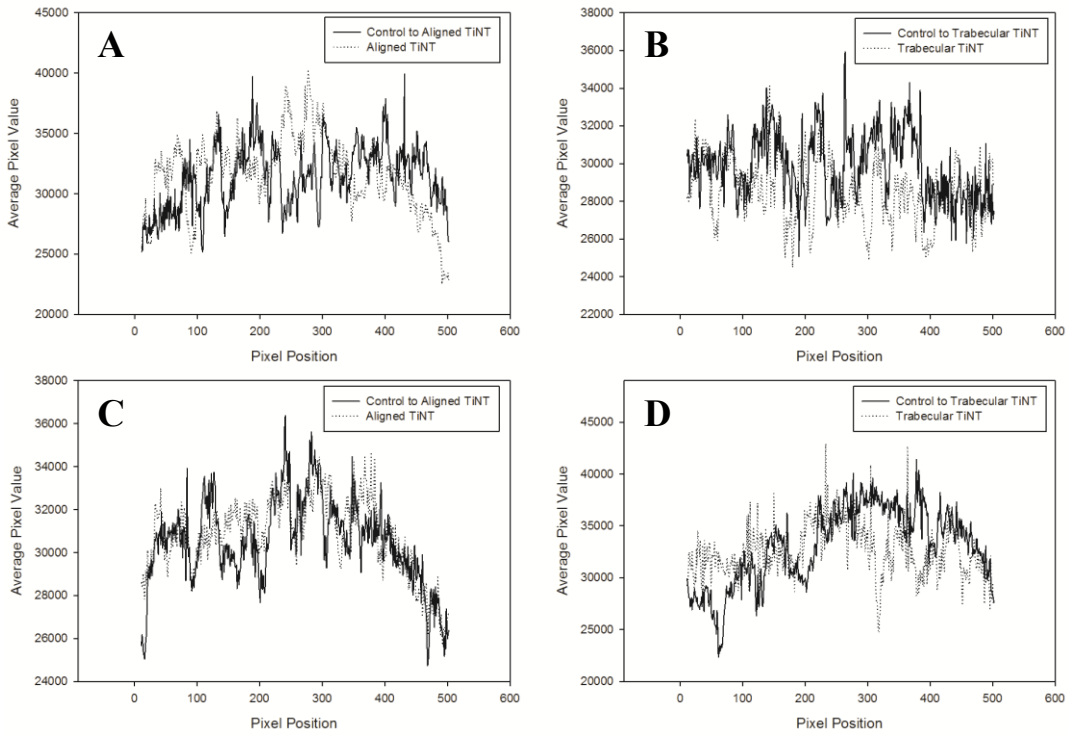

Figure 6.7. *Line profiles in the Distal region of interest. Profiles presented are internal Controls versus (A) Aligned TiNT at 4 weeks, (B) Trabecular TiNT at 4 weeks, (C) Aligned TiNT at 12 weeks, and (D) Trabecular TiNT at 12 weeks.*

Following BEI, each longitudinal section was stained with SBVG (Figures 6.8 and 6.9). Ratios of bone-implant contact between TiNT and Control femora were calculated, showing increased bone-implant contact in femora with TiNT implants (Table 6.3). At 12 weeks, both Aligned and Trabecular TiNT implants established approximately 1.5 times greater bone-implant contact than Control-implanted femora.

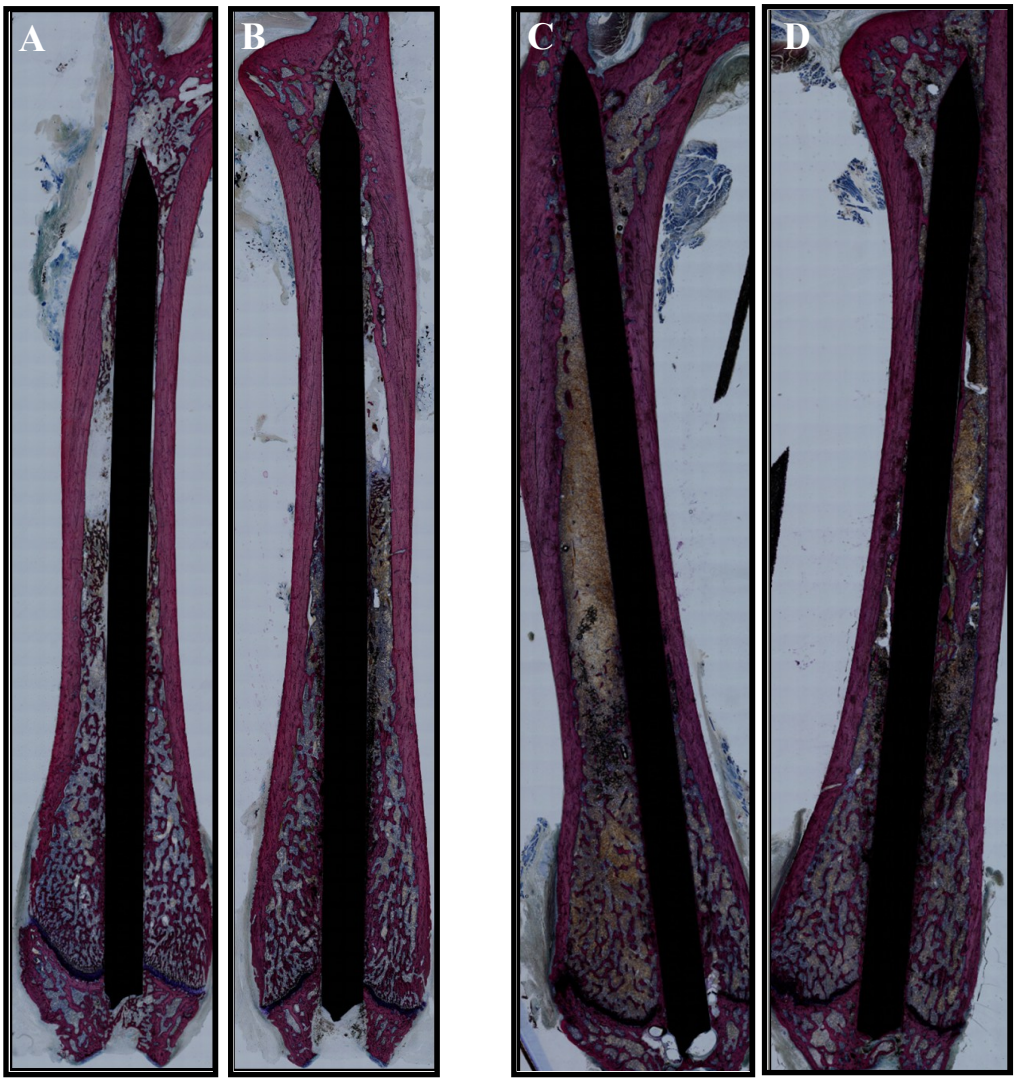

Figure 6.8. *Representative images of full-mount undecalcified histologic sections. Images shown are from (A) internal Control of Aligned TiNT, (B) Aligned TiNT, (C) internal Control of Trabecular TiNT, and (D) Trabecular TiNT. (SBVG; 20x magnification)*

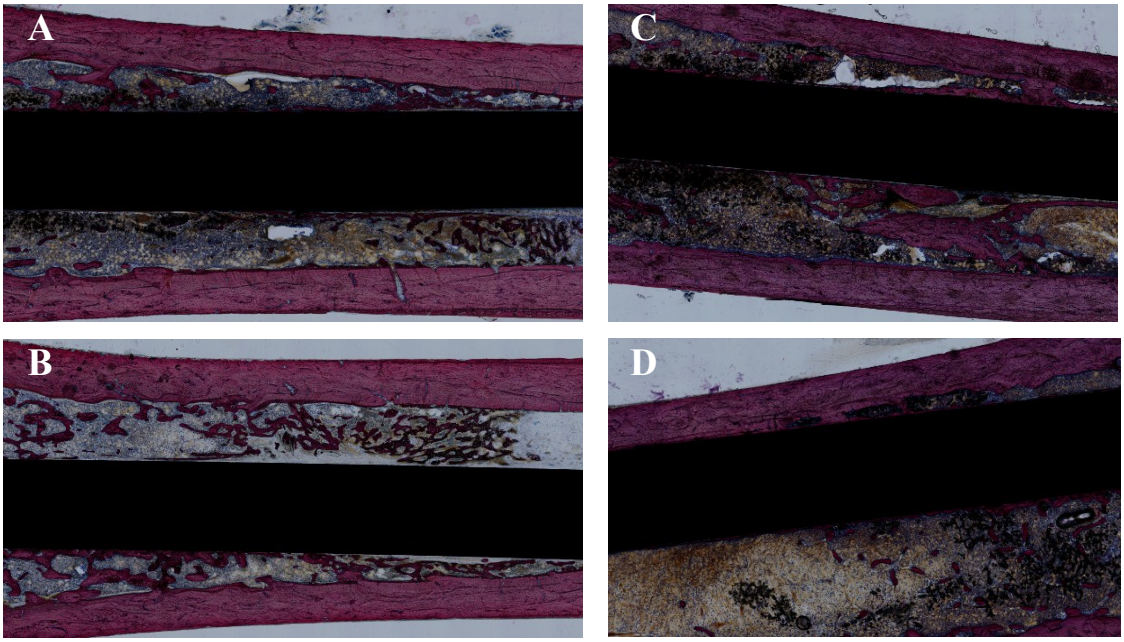

Figure 6.9. *Representative images of regions of interest from histologic sections. Images shown are from full-mount undecalcified histologic sections of (A) Aligned TiNT, (B) internal Control of Aligned TiNT, (C) Trabecular TiNT, and (D) internal Control of Trabecular TiNT. (SBVG; 50x magnification)*

Table 6.3. *Average bone-implant contact ratios. Bone-implant contact was measured on full-mount histologic sections at two endpoints.*

Group	Endpoint (week)	Average Ratio of Bone-Implant Contact (TiNT/Control)*
Aligned TiNT	4	2.95 (2.73)
	12	1.58 (0.24)
Trabecular TiNT	4	1.10 (0.67)
	12	1.50 (0.55)

* Standard deviation listed in parentheses

Each femora randomized to biomechanics testing was subjected to a tensile test to facilitate K-wire pull-out (Figure 6.10). Strength of fixation and maximum failure load

were then calculated for each femora, then averaged according to morphology and endpoint (Figure 6.11). However, at the 4-week Trabecular TiNT group, only three matched pairs were tested due to one failure at the time of femora preparation for testing (i.e. K-wire dislodged from femur) and one *in vivo* fracture discovered at endpoint dissection.

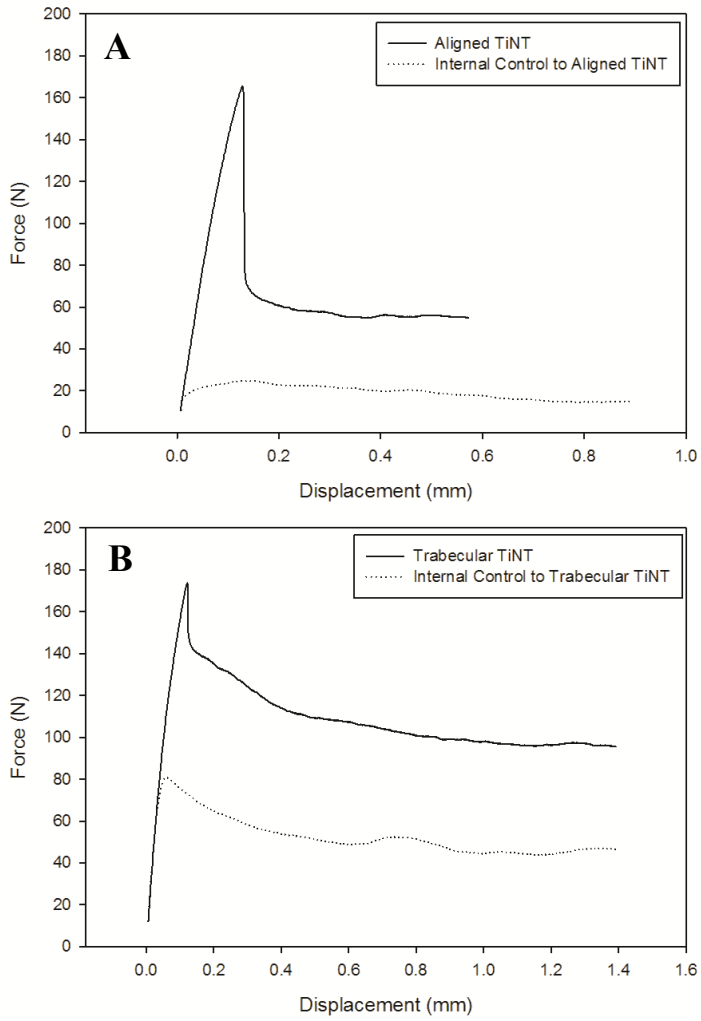

Figure 6.10. *Representative force-displacement curves obtained from biomechanical testing. Biomechanical testing was performed via wire pull-out. Force-displacement curves are shown for an (A) Aligned TiNT versus internal Control to Aligned TiNT (Rat 36) and a (B) Trabecular TiNT versus internal Control to Trabecular TiNT (Rat 26).*

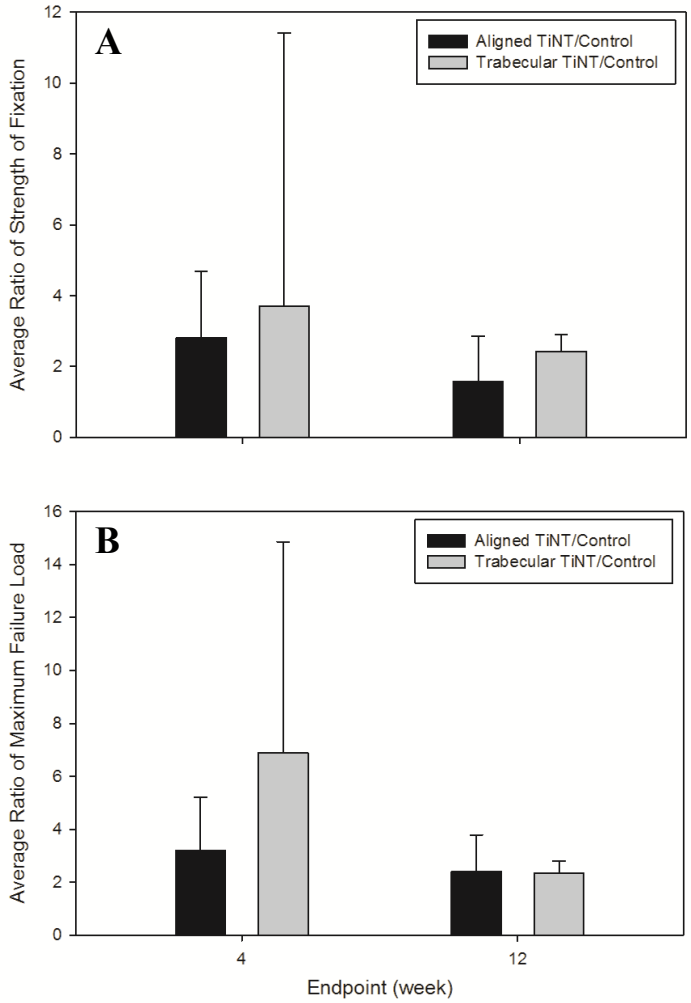

Figure 6.11. *Average maximum failure load and strength of fixation at two endpoints. The average (A) maximum failure load and (B) strength of fixation data are presented as ratios between TiNT morphology and Controls.*

At the 4-week endpoint, the average ultimate load of Aligned TiNT-implanted femora was 114 N (range, 59 to 165) and the Trabecular TiNT group was 148 N (range, 79 to 231), compared to the respective internal Controls 41 N (range, 23 to 65) and 38 N (range, 12 to 76). The difference in maximum failure load was significant for the Aligned TiNT versus internal Control groups ($p=0.016$) as well as the Trabecular TiNT versus internal Control groups ($p=0.025$) at 4 weeks. At 12 weeks, femora in the Aligned TiNT

and Trabecular TiNT groups achieved average maximum failure loads of 208 N (range, 152 to 263) and 179 N (range, 108 to 206), with comparative Controls demonstrating loads of 140 N (range, 23 to 218) and 139 N (range, 81 to 199), respectively.

The ratio of strength of fixation between experimental TiNT and internal Control femora was also calculated for each pair, then averaged by morphology and endpoint. The strength of fixation of the Trabecular TiNT group was 3.7 and 1.3 times greater than Control at 4 and 12 weeks, respectively. In the Aligned TiNT group, strength of fixation was 2.8 and 1.6 times greater than Control at 4 and 12 weeks, respectively. Strength of fixation was significantly greater for the Aligned TiNT group, compared to internal Controls, at the 4-week endpoint ($p=0.016$).

Several K-wires were imaged with SEM after biomechanical testing. Imaging showed several regions of the K-wires encased in bone after 4 weeks of implantation (Figure 6.12). One region imaged demonstrated mature bone cleaved from the cortical bone in the intramedullary canal during testing (Figure 6.12A), indicating that failure occurred at the bone-bone interface and not due to the nanotube surface disuniting from the implant. A second region showed the K-wire copiously coated in bone, with visible lacuna signifying organized bone tissue development (Figure 6.12B). Additionally, bony protrusions in this region were likely attached to the cortical bone prior to mechanical testing. A high magnification image of the second region shows the nanotube surface still coated in adsorbed protein after mechanical testing (Figure 6.12C).

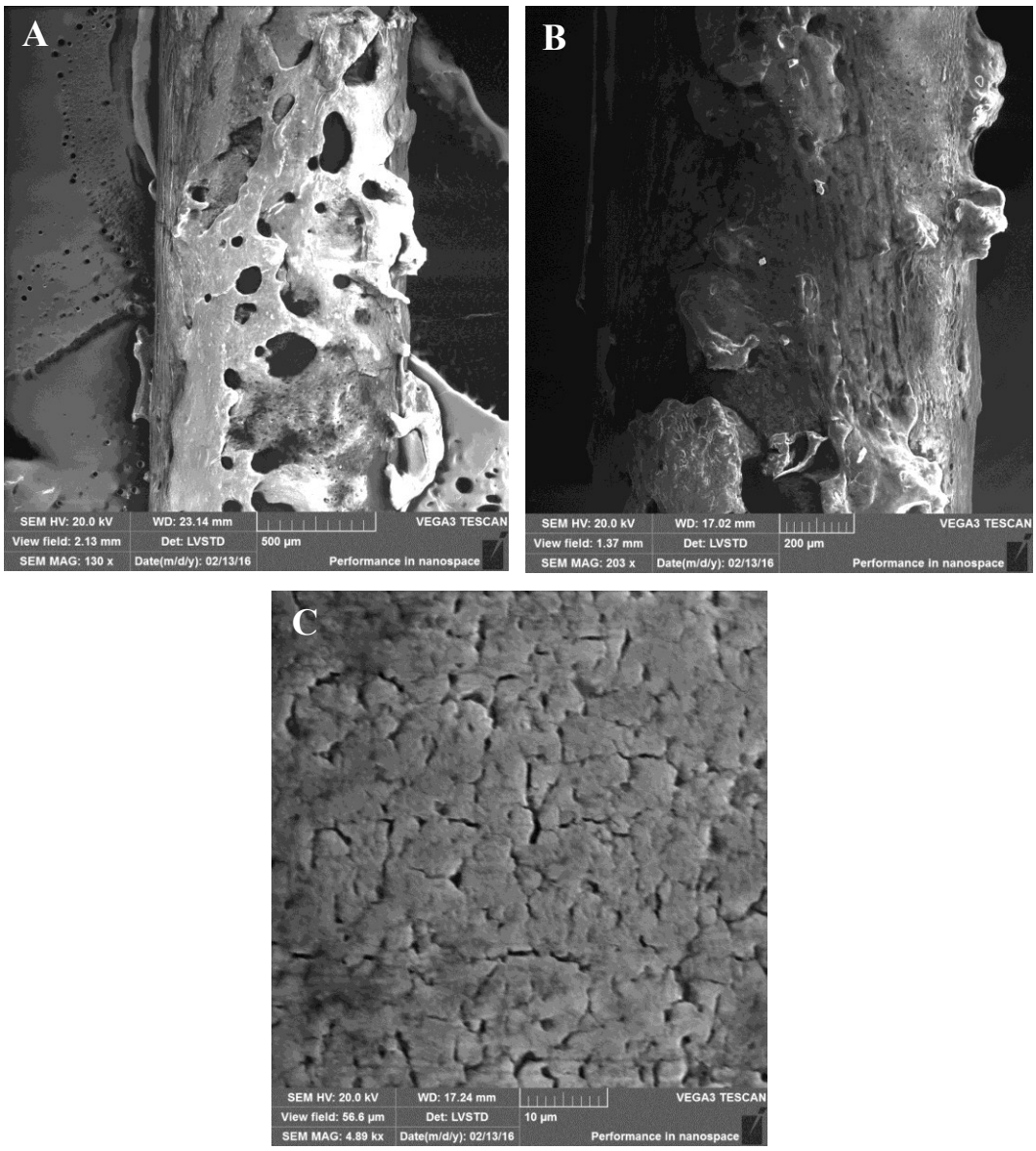

Figure 6.12. *Trabecular TiNT Kirschner wire imaged after biomechanical testing. These implants (pilot group) were implanted for 4 weeks. Scanning micrograph images show (A,B) implants coated in bone and (C) adsorbed protein.*

6.4 Discussion and Conclusions

In vivo osseointegration was evaluated via a rat intramedullary implant model, using biomechanics, undecalcified histology, microcomputed tomography (µCT) and backscattered electron imaging (BEI) techniques. These studies were designed to test our

hypotheses that TiNT surfaces would improve osseointegration at both early and late timepoints, due to increased osteoblast attachment and bone mineralization.

The model used in this work, intramedullary fixation in a rat, is a common model to assess osseointegration after different treatments (e.g. implant technologies, systemic or local applications of compounds).[97-99] All study animals tolerated the surgical procedure, gained weight, and were weight-bearing (immediately postoperative) through the respective 4- or 12-week postoperative period.

Various characterization methods were used to evaluate the osseointegrative properties of the implanted femora at early and late, 4- and 12-week, endpoints. Three matched pairs (TiNT and internal Control) femora were subjected to μCT, BEI, and histologic analyses. μCT evaluation showed both total bone volume and bone volume fraction of TiNT-implanted femora increased at greater rates than internal Controls from the 4- to 12-week endpoints in the Distal and Midshaft VOIs, on average. In the Distal VOI, Aligned TiNT implants demonstrated increased bone formation compared to Control, with a ratio of 1.3. Bone formation was nearly equivalent for Trabecular TiNT and Control surfaces. In the Midshaft VOI, the total bone volume and bone volume fraction ratios ranged from 1.5 (Aligned TiNT) to 2.1 (Trabecular TiNT) at the 4-week endpoint and 2.6 (Trabecular TiNT) to 16.8 (Aligned TiNT) at the 12-week endpoint, indicating enhanced bone formation in the midshaft for both TiNT surfaces. Aligned TiNT ratios at 12 weeks were skewed by a single matched pair, due to exceptional bone formation in the TiNT-implanted femora compared to the internal Control. Dang, *et al.* assessed differences between three types of screw implants: titania nanotube-etched (at 10 V and 40 V), titania nanotube + strontium-etched, and grit-blasted titanium (control),

which were implanted into the intercondylar notches of SD rats for 12 weeks. The average bone volume fraction of the titania nanotube-etched screws ranged from approximately 0.17 to 0.20 for the two sample types, compared to our results of 0.40 for Trabecular TiNT and 0.52 for Aligned TiNT implants in the Distal VOI at the 12-week endpoint.[115] Similarly, a study of implants fabricated via etching titania nanotubes onto resorbable blast media demonstrated significantly increased bone volume at 12 weeks versus controls (machined and titania nanotube-etched machined surfaces), after implantation into canine humeri.[116]

Regarding μCT-based histomorphometric data, Ban, *et al.* reported significantly increased BMD in the etched titania nanotubes on resorbable blast media samples.[116] Our study showed approximately equivalent BMD in both the Aligned TiNT and Trabecular TiNT implants, compared to Controls; however, the VMD of the Aligned TiNT and Trabecular TiNT groups was greater than Controls (range, 1.04 to 1.46 times) at the 12-week endpoint in both the Distal and Midshaft VOIs, indicating increased density of the bone tissue compared to Controls. At both endpoints and VOIs, Conn.D was greater in all TiNT femora compared to Controls (range, 1.13 to 71.29 times). In both TiNT and Control femora VOIs and endpoints, SMI suggested a more plate-like structure, as demonstrated by the SMI (range, 0.400 to 1.268). In the Distal VOIs, Tb.N remained approximately equivalent between both TiNT morphologies and Controls at both endpoints, but was greater than Controls in the Midshaft VOI and also increased from the 4-week to 12-week endpoint. At a 12-week endpoint, Dang, *et al.* reported a Tb.N value of approximately 4/mm in the distal femora of SD rats implanted with titania nanotube-etched implants, compared to 7.3/mm and 7.8/mm in our Trabecular TiNT and

Aligned TiNT groups, respectively.[115] Both TiNT groups and Controls had equivalent Tb.Th in both VOIs at the 4-week endpoint, and then all values increased to 1.03 to 1.97 times greater than Control at the 12-week endpoint. Specifically, Tb.Th at 12 weeks were 0.085 mm and 0.096 mm for Trabecular TiNT and Aligned TiNT groups, respectively, compared to values ranging between 0.04 and 0.05 μm in a similar study.[115] In general, Tb.Sp was greater than Controls in the Trabecular TiNT group and less than Controls in the Aligned TiNT group, at both endpoints and VOIs. Dang, *et al.* demonstrated less Tb.Sp, approximately 0.2 μm, while our data showed values of 0.147 mm in the Trabecular TiNT group and 0.143 mm in the Aligned TiNT group.[115]

BEI showed that the bone-implant contact fractions were 1.4 and 1.3 times greater in the Trabecular TiNT and Aligned TiNT implants than their internal Controls in the Distal ROI, respectively. However, BEI results were inconsistent in the midshaft, as only one longitudinal section was analyzed, compared to three-dimensional assessment capabilities around the entire implant in μCT analysis. Similar to our BEI findings in the distal region of interest, a study comparing titania nanotube-etched and titania grit-blasted screws in a rabbit model of distal femoral condyle implantation indicated titania nanotube implants had 1.1 times more *de novo* bone formation, on average, than grit-blasted samples at a six-week endpoint.[85] Histologic analysis assessed the bone-implant contact along the full length of the implant (except the unetched trocar tip) and approximately agreed with the BEI analysis of the distal region at the 12-week endpoint, with bone-implant contract ratios of approximately 1.5 for both TiNT implants versus internal Controls. Longitudinal sections from titania nanotube-etched implants exhibited a narrow curtain of bone (predominately mature), which extended along large sections of

the bone-implant interface, which was not observed in Control sections. Sul also observed a thin border of bone tissue surrounding titania nanotube-etched screws within the marrow cavity, yet, this border of bone tissue was not adjacent to grit-blasted implants.[85] von Wilmowsky, *et al.* also reported greater bone-implant contact of titania nanotube-etched rod-shaped implants versus unmodified, internal controls at 14-day and 90-day endpoints, in a pig model of frontal bone (skull) implantation.[88]

Five matched pairs of femora underwent biomechanical testing via a wire pull-out test to determine strength of fixation. In both TiNT morphology groups at both endpoints, the TiNT-etched implants demonstrated greater strength of fixation compared to internal Controls, between 1.3 and 3.7 times, on average. Also, the average strength of fixation increased for both TiNT groups, by 94 N for the Aligned TiNT group and 32 N for the Trabecular TiNT group, from the 4- to 12-week endpoints. At the 4-week endpoint, the maximum failure loads of the Aligned TiNT ($p=0.016$) and Trabecular TiNT ($p=0.025$) were significantly greater than internal Controls, respectively. Similarly, strength of fixation in the Aligned TiNT group was significantly greater than controls ($p=0.016$). Dang, *et al.* performed tensile testing to test the pull-out strength of the 12 mm long implants placed in the intercondylar notch of the femur for 12 weeks, which showed the two titania nanotube-etched groups had significantly greater failure loads than controls.[115] Using their reported load data and implant dimensions, the average strength of fixation for their nanotube-etched groups produced via 10 V and 40 V were approximately 0.32 MPa and 0.85 MPa, respectively. On average, the strength of fixation of the Trabecular TiNT and Aligned TiNT groups measured 1.87 MPa and 2.29 MPa at a 12-week endpoint. Several other *in vivo* studies reported greater failure loads in titania

nanotube-etched samples versus controls, however comparing their results to our study is complicated by implant treatments, implant location and/or animal type.[72, 86] SEM imaging demonstrated titania nanotube post-test survivability, as Friedrich, *et al.* and von Wilmowsky, *et al.* showed in simulated bone material (Sawbones) and porcine models.[88, 117]

Our study was limited primarily by sample size, with n=3 matched pairs in the "Imaging" group and n=5 matched pairs in the "Biomechanics" group. Although our results are unpowered, consistent trends were demonstrated throughout the characterization process, indicating the positive influence of the TiNT surfaces on osseointegrative properties.

We presented an *in vivo* study comparing two TiNT morphologies to an unmodified control. In a clinically-relevant model of femoral intramedullary fixation, characterization of harvested femora demonstrated greater bone formation and quality as well as strength of fixation in femora implanted with TiNT-etched implants versus control-implanted femora.

Chapter 7:

Future Work

7.1 Introduction

Our hope is that the previously described studies advance the research of titanium nanotube (TiNT) surfaces for biomedical applications. Certainly, there are numerous continuations of this work. In the sections below, planned and proposed research concepts are presented.

7.2 Proposed Concept 1: Local Delivery of SDF-1β via Titania Nanotube Surfaces

During primary or revision orthopaedic surgical procedures, the periprosthetic environment is exposed and primed for local delivery of pharmacologic agents and small molecules, which may modulate various biologic responses, including inflammation, foreign body response, and osteogenesis. Drug delivery localized to the affected tissues precludes deleterious effects of systemic drug delivery. For instance, systemic delivery of etidronic acid, a bisphosphonate used to reduce loss of bone mass and bone resorption by promoting osteoclast apoptosis, may cause fevers, transient hematologic changes, and irritative reactions (of skin, peritoneum, and pericardium) as well as uveitis, scleritis, and phlebitis.[118-120] The morphology of TiNT surfaces, with voids and hollow structures thereby increasing total surface area, is ideal for drug loading and delivery. Numerous groups have drug-loaded TiNT surfaces via immersion, film deposition, intercalation, or pipetting techniques.[121-126]

Our proposed research will evaluate the drug delivery potential of these two morphologies of titania nanotube surfaces prepared via functionalization of heparin binding domains. Our work will use a drug release kinetics experiment and *in vivo* (rat) model of femoral intramedullary fixation (simulated femoral stem or stemmed distal femoral condyle, as described in Chapters 5 and 6) with biomechanical, histologic, and μCT characterization to assess the influence of TiNT structure and drug delivery on *de novo* bone formation and bone-implant stability at a single (12-week) timepoint.

As described, our previous work has demonstrated promising osteogenic effects of both Aligned TiNT and Trabecular TiNT surfaces on marrow-derived cells. We subsequently translated these *in vitro* results to an *in vivo* study, where μCT scans performed at 4- and 12-week postoperative endpoints demonstrated increased bone formation in TiNT implants, compared to unmodified titanium implants. In the proposed research, we will use Aligned TiNT and Trabecular TiNT implants to deliver stromal cell-derived factor 1 (SDF-1β), which is highly chemotactic for mesenchymal stem cells.[127] We hypothesize that SDF-1β delivery will result in enhanced recruitment of stem cells and subsequent new bone formation by the recruited cells.

7.2.1 Specific Aims

In this study, we plan to first evaluate the drug loading and release potential of the protein SDF-1β from two morphologies of titania nanotube surfaces and as-received (unmodified) titanium. A surface chemistry-based approach to drug loading will be used in an effort to achieve sustained drug release. These results will then be translated into an

in vivo study to assess differences in bone formation between protein-loaded and unloaded Aligned TiNT- and Trabecular TiNT-etched implants.

Aim 1: Demonstrate extended release of SDF-1β from TiNT surfaces, prepared with Aligned TiNT and Trabecular TiNT morphologies and functionalized with heparin-binding domains.

Aim 2: Investigate the effect of heparin-mediated SDF-1β delivery from TiNT surfaces on *in vivo* bone formation, using microcomputed tomography (μCT), backscattered imaging, biomechanical testing and undecalcified histology.

7.2.2 Study Design

7.2.2.1 Aim 1: Heparin-Dopamine Functionalization of TiNT Implants and SDF-1β Release Kinetics

Work in Aim 1 will focus on functionalization of TiNT surfaces to bind SDF-1β as well as characterization of resultant release kinetics. Two TiNT surfaces, Aligned TiNT and Trabecular TiNT, will be compared to as-received (unmodified) titanium (Control). Samples (coupons and Kirschner wires) will be prepared as described in Chapter 3.

To promote the attachment of SDF-1β to the implant materials, all surfaces will be functionalized with a heparin-dopamine (Hep-DOPA) conjugate (5mg of heparin/mL solution). SDF-1β, like many cytokines and chemokines, possesses a heparin-binding domain. The dopamine component of the Hep-DOPA conjugate will anchor heparin

molecules to the metal-oxide surface, thus promoting the electrostatic deposition of SDF-1β.[128] The Hep-DOPA conjugation technique for heparin immobilization is well-established on metal and metal-oxide surfaces.[129, 130] Confirmation of Hep-DOPA conjugation will be confirmed via an established toluidine blue staining method as well as x-ray photoelectron spectroscopy (XPS).[131] Kim, *et al.* observed a decrease in nitrogen content when heparin was engrafted onto amine-treated titania surfaces.[132] In a separate study, Lui, *et al.* showed increased sulfur content when functionalizing surfaces with Hep-DOPA.[133]

To immobilize SDF-1β (positive charge) onto the surfaces, Hep-DOPA-functionalized TiNT samples will be immersed in 2-(N-morpholino)ethanesulfonic acid (MES)-buffered SDF1-β (1mg/mL) then shaken overnight, washed dried at 50°C. Prepared samples will then be immersed in individual wells filled with 1000μL of phosphate buffered saline and bovine serum albumin (PBS+BSA) solution at 37°C, in order to study the release kinetics of SDF-1β from Hep-DOPA-modified Aligned TiNT, Trabecular TiNT and as-received titanium specimens. Every 24 hours, 100μL of PBS+BSA will be removed and refreshed. At designated timepoints (24 hours…3, 5, 7, 14, 21, 28, 35, 49, 63, 77, and 91 days), 100μL of supernatant will be extracted for quantification of SDF-1β via ELISA (Rat Stromal Cell Derived Factor 1 ELISA Kit, MyBiosource, San Diego, CA). Our group has also developed a HPLC-based method for detection of chemokines in release media, which will be used if immunoenzymatic methods fail.

7.2.2.2 Aim 2: Comparison of In Vivo Osteogenicity of SDF-1β-functionalized TiNT Implants

Following confirmation of successful functionalization and release, we will begin *in vivo* testing detailed in Aim 2. Using titanium as well as stainless steel implants, our group has performed more than 100 implantations of intramedullary implants (Kirschner wires; K-wires) in rat femora, thereby optimizing both surgical technique as well as μCT- and histology-based characterization of periprosthetic bone formation in this challenging model. Ti-6Al-4V K-wires with a 1.25 mm diameter will be prepared with either an Aligned TiNT or Trabecular TiNT surface (Aim 1). Also, half of the implants will be loaded with SDF-1β using the Hep-DOPA conjugation technique (Aim 1). Following preparation of the implants, 16 Sprague Dawley rats will undergo a bilateral implantation procedure to insert K-wires into the intramedullary canal of the femur, as described in Chapters 5 and 6. This model is widely-used to assess periprosthetic bone formation around implants to be used as structural elements in total joint arthroplasty procedures.[48, 98, 99, 134] Rats will be randomized to receive either Aligned TiNT or Trabecular TiNT K-wires, with both femora receiving K-wires with the same morphology. Each femur will receive one SDF-1β-functionalized implant and one unloaded TiNT implant, which will also be randomized (Table 7.1).

Table 7.1. *Distribution of animals and limbs in each group. Planned characterization methods are also listed.*

Group	Number of Animals	Number of Limbs	μCT	Histology	Biomechanics
Aligned TiNT	8				
+ SDF-1β		8	8	3	5
- SDF-1β		8	8	3	5
Trabecular TiNT	8				
+ SDF-1β		8	8	3	5
- SDF-1β		8	8	3	5

Periprosthetic bone formation in all limbs will be characterized via serial μCT imaging at 3, 6 and 12 weeks postoperative. Resultant DICOM images will be analyzed via on-board software scripts to obtain histomorphometric properties of *de novo* bone, including total tissue volume (TV), total bone volume (BV), bone volume fraction (BV/TV) as well as volume and bone mineral density (VMD; BMD). At the 12 week endpoint, animals will be euthanized and femora excised. Limbs randomized to histologic characterization of bone formation will be prepared as described in Chapter 6. Backscattered electron imaging will be performed on all ground sections with an environmental scanning electron microscope, in order to quantify the degree of mineralization at the bone-implant interface as well as the bone-implant contact area. Following imaging, methyl-methacrylate-embedded specimens will undergo microtomy to yield thin, 5 mm sections which will be stained with Stevenel's Blue and von Gieson picrofuschin (SBVG). Stained sections will be digitally scanned at 40x magnification and resultant digital images will be analyzed by a blinded grader will be employed to quantify the number of osteoblasts and osteoclasts per high-powered field. Limbs randomized to biomechanical analysis will be wrapped in saline-soaked gauze and frozen at -20°C until analysis.[135] The strength of the bone-implant interface will be characterized via biomechanical pull-out testing performed on a materials loading frame, as described in Chapter 6.

7.2.3 Anticipated Outcomes

SDF-1β is a protein chemotactic to mesenchymal stem cells (MSCs). These proteins have not previously been loaded onto TiNT surfaces. We expect to generate data

showing that Hep-DOPA conjugation results in sustained versus burst delivery of SDF-1β from TiNT surfaces compared to unmodified control implants. Because of the increased surface area associated with Trabecular TiNT surfaces, we anticipate increased SDF-1β loading on Trabecular TiNT surfaces compared to Aligned TiNT surfaces. Similarly, we anticipate increased bone formation on Trabecular TiNT + SDF-1β surfaces *in vivo* due to the higher drug loading.

7.2.4 Study Status

This study has been funded by a Beaumont Health Seed Grant and is in progress. All pilot work has been completed, with toluidine blue staining and X-ray photoelectron spectroscopy (XPS, Kratos Axis Ultra, Kratos Analytical, Manchester, United Kingdom) confirming Hep-DOPA functionalization of TiNT surfaces (Figures 7.1 and 7.2).

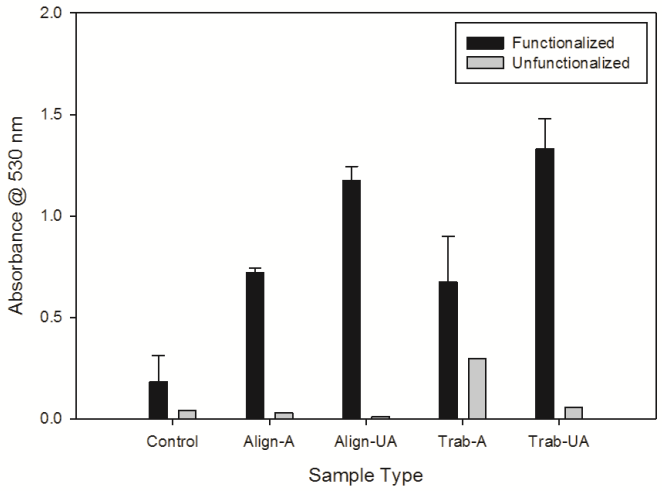

Figure 7.1. *Toluidine blue staining for heparin content on sample coupons. Staining showed greater heparin content on heparin-dopamine-functionalized coupons than unfunctionalized coupons. [Groups: Control, Annealed Aligned TiNT (Align-A), Unannealed Aligned TiNT (Align-UA), Annealed Trabecular TiNT (Trab-A), Unannealed Trabecular TiNT (Trab-UA)]. Values were corrected (i.e. baseline absorbance subtracted) based on calculated standards.*

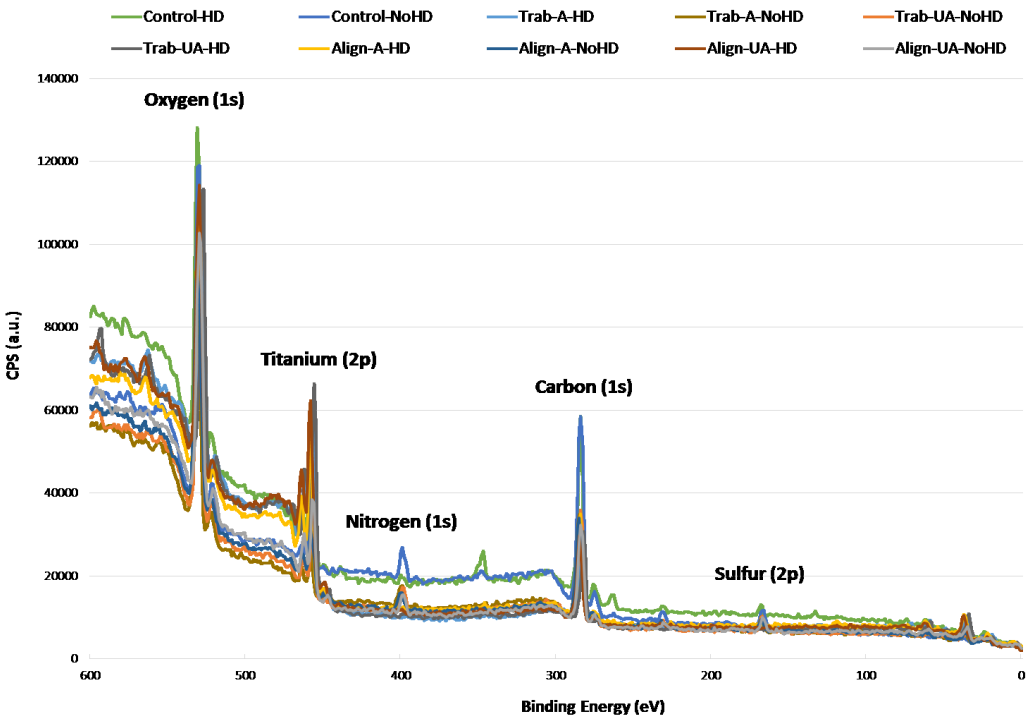

Figure 7.2. *Spectra obtained from X-ray photoelectron spectroscopy of sample coupons. Samples analyzed were heparin-dopamine-functionalized annealed, unannealed, and control titania and titania nanotube-etched surfaces. The spectra demonstrated a decrease in nitrogen and sulfur contents on heparin-dopamine-functionalized annealed, unannealed, and control titania and titania nanotube-etched surfaces.*

Toluidine blue staining showed greater heparin content on coupons functionalized with Hep-DOPA than on unfunctionalized coupons. On the functionalized surfaces, unannealed coupons contained a greater amount of bound heparin than annealed coupons. XPS demonstrated decreased nitrogen and sulfur contents on surfaces with bound heparin, further confirmation of effective Hep-DOPA functionalization. Based on these results, the remaining experiments will be conducted with unannealed titania nanotube surfaces.

A pilot experiment was performed to immobilize three dosages of SDF-1β onto functionalized K-wires, in order to establish attachment behavior (Table 7.2). Results

showed greater than 99% attachment of SDF-1β on all surfaces at all dosages at time zero.

Table 7.2. *SDF-1β attachment on Kirschner wires. Wires were prepared with unannealed titania nanotube and Control surfaces at three dosages.*

Group	Immobilized SDF-1β (ng)	SDF-1β Attachment (%)
Trabecular TiNT	50	99.9893
	100	99.9909
	500	99.9986
Aligned TiNT	50	99.9882
	100	99.9948
	500	99.9978
Control	50	99.9899
	100	99.9937
	500	99.9991

A pilot release experiment was conducted to trial the proposed methods. Again, three dosages were examined. Samples were immersed in a PBS+BSA solution, and the supernatant was analyzed at four timepoints (Figure 7.3). All samples showed similar release profiles, with total released quantity of SDF-1β averaging 0.0413 ng (range, 0.0365 to 0.0487) for all groups and dosages.

Next steps include finishing the drug release kinetics experiments, which began early June 2016, and K-wire implantation procedures, which will be performed in July 2016 (surgeries boarded: 7/5/16, 7/716, 7/12/16, 7/14/16). The final experimental endpoint is scheduled for September/October 2016.

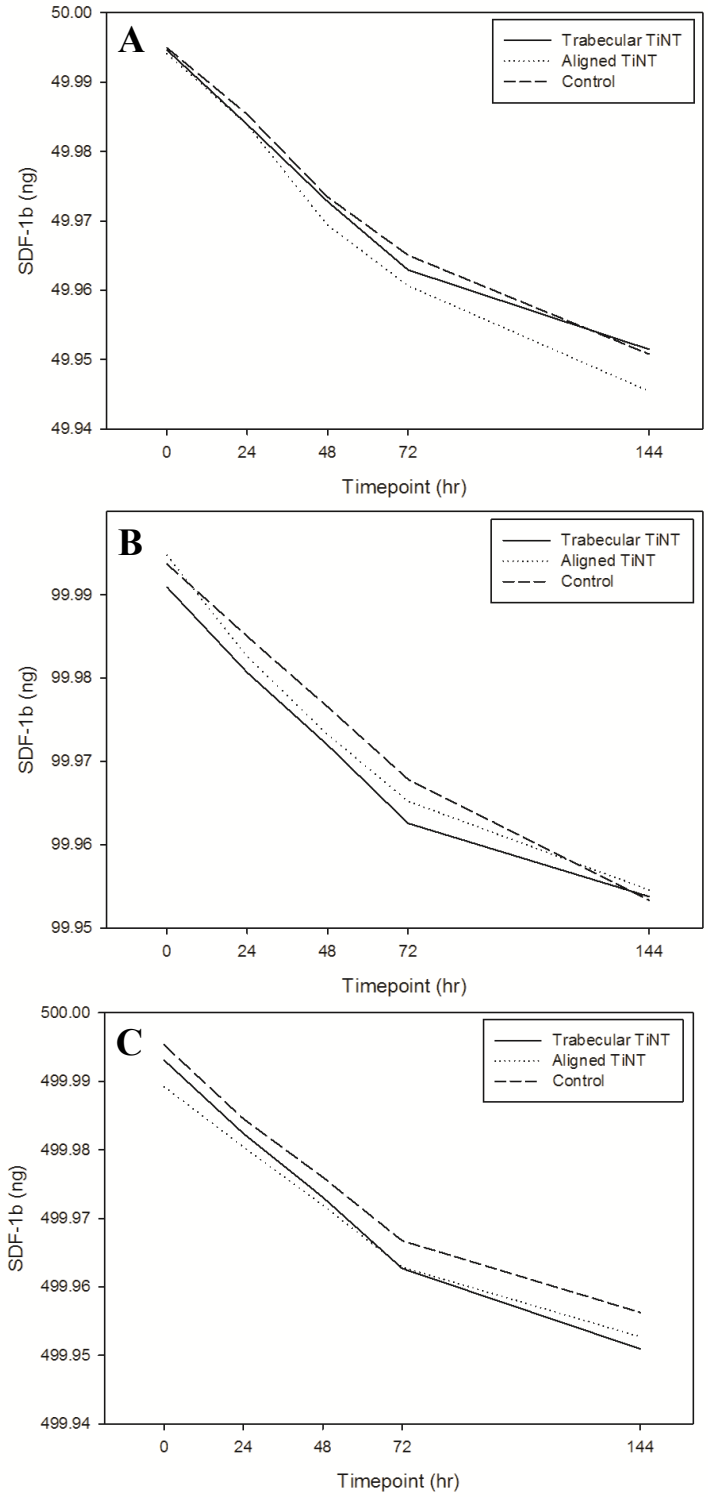

Figure 7.3. *Release profiles of SDF-1β from Kirschner wires. Wires were unannealed and functionalized with heparin-dopamine before attaching SDF-1β. Attachment was assayed at five timepoints: 0, 24, 48, 72, and 144 hours. Three dosages of SDF-1β were evaluated, including (A) 50ng, (B) 100ng, and (C) 500ng.*

7.3 Proposed Concept 2: Assessing Biocompatibility of Titania Nanotubes via Murine Air Pouch Model

A 2004 study by Ren, *et al*. first described an *in vivo* model of orthopaedic wear-debris associated osteolysis using ultra-high molecular weight polyethylene (UHMWPE) particles.[136] In the model, air pouches were produced on the backs of BALB/c mice (female, 8-10 weeks old) by sterile air injection. Six days after pouch formation, femora and calvaria from littermates were harvested to use as donor bone tissue. Either femora or calvaria tissue were placed into air pouches and sutured closed. The following day, UHMWPE particles were injected into the pouch to initiate the wear-debris induced inflammatory cascade leading to periprosthetic osteolysis [experimental groups: 5 mg of particles suspended in 0.5 mL of fetal bovine serum/phosphate buffered saline; control group: 0.5 mL of fetal bovine serum/phosphate buffered saline (FBS/PBS)] until experiment endpoints at 2, 7, and 14 days after particle injection. At endpoint, pouch membrane, bone tissue (femora or calvaria), and fluid from pouch were collected for analysis.

To assess the effect of UHMWPE particles on bone and surrounding (pouch) tissue, various characterization techniques were used. First, the thickness and total cell counts of the pouches were measured, showing differences between experimental and group groups. Tartrate-resistant acid phosphatase (TRAP) staining of implanted bone tissue for osteoclastic activity showed intense staining in both the pouch membranes and implanted calvaria. Clusters of osteoclasts were observed at the interface between tissue and UHMWPE particles. Polymerase chain reaction (PCR) analysis confirmed upregulation of capthesin K (CK) in tissues from experimental groups. Histologic

analysis also demonstrated differences between experimental and control groups. In UHMWPE-treated pouches, hematoxylin and eosin (H&E) staining showed bone erosion and Masson's trichrome staining showed bone collagen loss, compared to control pouches. The study indicated donor calvaria tissue implantation was more consistent than femora tissue, as the calvaria could be trimmed to 4 mm diameter and calvarial caps are associated with less affixed tissue.

The model continues to be used to test new materials and anti-inflammatory treatments of wear-debris induced osteolysis.[137-139] Gonçalves, *et al.* used a murine air pouch model to investigate the inflammatory response, specifically leukocyte infiltration, of titanium dioxide nanoparticles at early endpoints (3-24 hours after particle injection). In the study, nanoparticles (anatase, 90% sized 1-10 nm diameter) were purchased from a vendor as an aqueous solution stabilized by polyacrylate sodium. At the 3-, 6- and 9-hour timepoints, increased proportions of polymorphonuclear neutrophil cells (80 ± 2%, 91 ± 6%, 90 ± 6%, respectively) were observed in the nanoparticle-treated pouches versus control, before declining after the 9-hour timepoint.[140]

We propose a study of the wear debris generated from TiNT-etched surfaces and a follow-up *in vivo* study of TiNT wear particle injection, compared to particulate generated from unmodified (Control) surfaces. TiNT would be etched onto larger diameter rod stock, then sent for wear debris production at an experienced facility. Wear debris analysis would provide details regarding the particle sizing range and frequency and an endotoxin assay would be performed. Particles from each TiNT morphology (Aligned TiNT and Trabecular TiNT) and Control groups would be separately suspended, as described, and injected into murine air pouches implanted with calvaria bone tissue for

the prescribed endpoints. Pouch thickness and cell content would be measured at the prescribed endpoints of 2, 7, and 14 days. Additionally, TRAP, H&E, and Masson's trichrome staining would be performed on the calvaria tissue to assess osteoclastic activity and bone loss.

A potential follow-up study would include injecting wear debris into the intramedullary canal of mice femora to simulate *in vivo* wear debris production. In this model, particles could be labelled in order to track permeation and migration.[141, 142]

7.4. Proposed Concept 3: Bone Formation and Biocompatibility Studies in Higher Phylogenetic Order Species

The initial *in vivo* studies we conducted were in rat models of intramedullary fixation, in order to stimulate total joint arthroplasty. In order to move toward United States Food and Drug Administration approval of this technology, experiments must be performed using a higher phylogenic order species. We propose the use of a goat model of total hip arthroplasty.

Several studies have used this model.[143-146] In a series of three experiments, Harboe, *et al.* described the use of this model. All studies used a 6-month postoperative endpoint. In a 2012 study, the authors tested bone-implant interface strength of an innovative design of an uncemented femoral stem by pull-out testing, using a technique analogous to the wire pull-out method described in Chapter 6. Acetabular cups/liners and femoral heads developed for veterinary use in canines were substituted for the other total hip arthroplasty components.[144] The group's second study characterized both bony apposition and femoral stem pull-out testing on femoral stems coated with hydroxyapatite

and calcium phosphate. Following total hip arthroplasty, the gait of the goats was scored with a modified de Waal score.[147] At endpoint, the femoral stems were subjected to biomechanical pull-out testing and bone samples were harvested from the proximal collar of the stem. These bone samples were paraffin-embedded and imaged via light microscopy to assess bone structure as well as cellular activity indicative of an adverse reaction to the coatings.[145] Finally, bone samples were collected for histologic characterization. Samples were decalcified with ethylenediaminetetraacetic acid (EDTA) and stained with hematoxylin erythrosine saffron (HES), and then graded for bone apposition to the stem as well as necrosis. The presence or absence of cellular structures, including leukocytes and macrophages, was also evaluated.[146]

We propose a study replicating the characterization methods described in Chapter 6, using total hip arthroplasty components developed for use in the canine population (e.g. BioMedtrix Universal Hip CFX). Preoperatively, goats will be weighed and undergo load-bearing measurements of the operative limb, in order to obtain baseline data.[148, 149] Femoral stems would be etched with titania nanotubes on the implanted surface distal to the collar, then implanted using a defined surgical procedure.[144] Goats would be randomized to receive a Trabecular TiNT-etched, Aligned TiNT-etched, or Control implant. Each week, all postoperative goats will be weighed and assessed for load-bearing of the operative limb. At a single, 6-month endpoint, harvested femora would be randomized to either the biomechanical testing cohort or imaging/histologic analysis cohort. Femora randomized to biomechanical would undergo femoral stem pull-out testing, as described by Harboe, *et al.*[144-146] Femora in the imaging/histologic analysis cohort would be immersed in 10% neutral buffered formalin for 1 week to fix all

tissues, then rinsed with PBS and stored in ethanol. Femora would first be scanned with μCT (vivaCT-80, Scanco USA, Wayne, PA). Femora would then be sectioned in three regions, proximal, midshaft, and distal. After embedding each section, backscattered electron imaging would be performed on each section to assess bone-implant contact. Blocks would then be polished, and thin (5 μm), transverse sections would be cut from the proximal, midshaft, and distal regions (n=6 sections per region). Sections would be stained with SBVG (n=3) or H&E (n=3). SBVG-stained sections would be used both to assess bone-implant contact and overlay each matched μCT slice, in order to determine quantitative correlations between imaging and histologic analyses. H&E-stained section would be used for cellular analysis to assess biocompatibility, as described in Chapter 5.

Chapter 8:

Conclusions

The need for implant surfaces capable of both early and robust osseointegration will continue to rise as joint arthroplasty and other surgical procedures requiring bone ingrowth continue to increase annually. Over the term of implantation, wear debris is generated that can affect implant stability via wear debris-induced osteolysis. Development of materials that produce less wear debris or stimulate a decreased inflammatory response are desirable, in order to reduce the revision rates.

Titanium has historically been used as a material in orthopaedic surgery, due to its suitable mechanical and biocompatibility properties. Using a multifaceted approach, our study focused on translation between *in vitro* and *in vivo* experiments to assess the biocompatibility and osseointegrative potential of titania nanotube (TiNT) surfaces, etched from a clinically-relevant titanium alloy, were investigated.

In vitro testing centered on seeding rat-derived bone marrow cells (BMC; Sprague-Dawley strain) onto titania nanotube surfaces, in order to assess cell attachment, cell morphology, alkaline phosphatase (ALP) activity, osteocalcin expression as well as upregulation of specific genes. The BMC cells used in *in vitro* experiments are the same cell population in contact with implants in the subsequent *in vivo* experiments. Cell staining (Actin Green and DAPI) showed greater cell attachment and spreading, and indirectly cell viability, on TiNT surfaces at early timepoints. Cell nuclei staining (DAPI) indicated that smaller cell diameter and greater cell eccentricity on TiNT surfaces. Assays measured increased ALP activity and osteocalcin expression on TiNT surfaces at

multiple timepoints through 21 days, and indication that BMC differentiated toward an osteoblastic phenotype. Gene-level analysis showed upregulation of three genes related to bone formation, Col1a1, IGF-1, and osteonectin, through 21 days.

In vivo testing was performed in a clinically-relevant rat model of intramedullary fixation and focused on two themes, material-level biocompatibility and biologic response as well as osseointegration. An outbred rat strain, Sprague Dawley, was selected to approximate differences in osseointegrative potential analogous to the human population.

The *in vivo* biocompatibility study included animal general health assessments, specifically related to longitudinal weight again of animals, as well as remote organ weight, metal ion level (i.e. remote organs, whole blood), hematologic and undecalcified histologic analyses. No animals were flagged for problematic weight loss or systemic disease during the 12-week experiment. At two weekly weight assessments, 9 and 11 weeks postoperative, there were significant differences between animal weights, but the weights recovered by experiment endpoint. There were no significant differences in remote organ weights at endpoint. Metal ion analysis showed that Aligned TiNT and Trabecular TiNT had greater aluminum and vanadium content and lower titanium content, by wt%, compared to Control. The only significant finding from the metal ion analyses of remote organs and whole blood was elevated aluminum in lungs of the Trabecular TiNT-implanted group. Hematologic analysis, performed at endpoint, showed no significant differences between TiNT groups and Control. Significant differences in cell populations between the TiNT groups and Control were measured during undecalcified histologic analysis. In the TiNT-implanted femora, the periprosthetic tissue

demonstrated fewer inflammatory cellular activity, including fewer foreign body giant/multinucleated, eosinophil/basophil, and neutrophil cells, compared to Control. No significant differences were found in monocyte and lymphocyte activity between groups.

The *in vivo* osseointegration study used multiple characterization methods to assess bone ingrowth and ongrowth, including biomechanics, microcomputed tomography (μCT) undecalcified histology, and backscattered electron imaging (BEI) characterization. Wire pull-out testing demonstrated greater strength of fixation in the TiNT-implant femora than internal Controls, on average. The maximum failure loads and strength of fixation were significantly greater in the TiNT groups than internal Controls at the 4-week endpoint, and greater, on average, at the 12-week endpoint. μCT analysis indicated that total bone volume and bone volume fraction both increased more rapidly from the 4- to 12-week endpoints in TiNT-implanted femora, compared to internal Controls, in both the Distal and Midshaft volumes of interest (VOI). At the 12-week endpoint, Aligned TiNT implants demonstrated increased bone formation compared to internal Controls, with a ratio of 1.3, in the Distal VOI; however, bone formation was nearly equivalent between Trabecular TiNT and internal Controls. The Midshaft VOI demonstrated greater total bone volume and bone volume fraction ratios in both TiNT-implanted groups compared to internal Controls. Bone-implant contact measured on undecalcified histologic sections showed 1.5-fold increase in TiNT-implanted femora, compared to internal Controls, at 12 weeks. BEI analysis was approximately analogous to the undecalcified histology results in the distal femora region of interest. In the midshaft, the results were highly variable, as indicated by line profile plots.

In the chapter regarding future work, three proposals were presented. One concept, focusing on local delivery of SDF-1β from TiNT surfaces to increase stem cell recruitment and subsequent bone formation, is underway. Two additional concepts are continuations of the experiments presented in this document. A murine air pouch model of wear debris-induced osteolysis would provide more information regarding the biocompatibility of TiNT surfaces and biologic response to TiNT wear debris. To generate additional data regarding osseointegration, a model of total hip arthroplasty in a goat is proposed.

References

[1] Cherubino P, Ratti C, Fagetti A, Binda T. Total hip arthroplasty and bone fragility. Aging clinical and experimental research 2011;23:76-7.
[2] Harms S, Larson R, Sahmoun AE, Beal JR. Obesity increases the likelihood of total joint replacement surgery among younger adults. International orthopaedics 2007;31:23-6.
[3] Kurtz S, Ong K, Lau E, Mowat F, Halpern M. Projections of primary and revision hip and knee arthroplasty in the United States from 2005 to 2030. The Journal of bone and joint surgery American volume 2007;89:780-5.
[4] Production CfDCa. FastStats Inpatient Surgery (U.S. Data). 2013. p. Source: National Hospital Discharge Survey: 2010 Table. .
[5] Marieb E. Human Anatomy and Physiology. 5th ed. San Francisco: Benjamin Cummings; 2001.
[6] Gulson B, Taylor A, Eisman J. Bone remodeling during pregnancy and post-partum assessed by metal lead levels and isotopic concentrations. Bone 2016;89:40-51.
[7] Salles JP. Bone metabolism during pregnancy. Annales d'endocrinologie 2016;77:163-8.
[8] Sato S, Takeda S. [The regulation of various organs by osteoblasts]. Clinical calcium 2016;26:721-7.
[9] Regan JN, Waning DL, Guise TA. Skeletal muscle Ca(2+) mishandling: Another effect of bone-to-muscle signaling. Seminars in cell & developmental biology 2016;49:24-9.
[10] Miller JD MB, Alford AI, Hankenson KD, Goldstein SA, Abu-Amer Y, Clohisy JC. Orthopaedic Basic Science: Foundations of Clinical Practice. Third Edition ed. Rosemont, IL, USA: American Academy of Orthopaedic Surgeons (AAOS); 2007.
[11] Alberts B JA, Lewis J, et al. Molecular Biology of the Cell. 4th ed. New York: Garland Science; 2002.
[12] Kokabu S, Lowery JW, Jimi E. Cell Fate and Differentiation of Bone Marrow Mesenchymal Stem Cells. Stem cells international 2016;2016:3753581.
[13] Malecka A, Wang Q, Shah S, Sutavani RV, Spendlove I, Ramage JM, et al. Stromal fibroblasts support dendritic cells to maintain IL-23/Th17 responses after exposure to ionizing radiation. Journal of leukocyte biology 2016.
[14] Pontikoglou C, Deschaseaux F, Sensebe L, Papadaki HA. Bone marrow mesenchymal stem cells: biological properties and their role in hematopoiesis and hematopoietic stem cell transplantation. Stem cell reviews 2011;7:569-89.
[15] Jones EA, Giannoudis PV, Kouroupis D. Bone repair with skeletal stem cells: rationale, progress to date and clinical application. Therapeutic advances in musculoskeletal disease 2016;8:57-71.
[16] Friedrich C, Zausch E, Sugrue S, Gutierrez-Ramos J. Hematopoietic supportive functions of mouse bone marrow and fetal liver microenvironment: dissection of granulocyte, B-lymphocyte, and hematopoietic progenitor support at the stroma cell clone level. Blood 1996;87:4596-606.
[17] Chen Q, Shou P, Zheng C, Jiang M, Cao G, Yang Q, et al. Fate decision of mesenchymal stem cells: adipocytes or osteoblasts[quest]. Cell Death Differ 2016.

[18] Oursler M, et al. ASBMR Bone Curriculum. The American Society for Bone and Mineral Research; 2007.
[19] Bell NH. RANK ligand and the regulation of skeletal remodeling. Journal of Clinical Investigation 2003;111:1120-2.
[20] Boyce BF, Xing L. Functions of RANKL/RANK/OPG in bone modeling and remodeling. Archives of biochemistry and biophysics 2008;473:139-46.
[21] Cutler GB, Jr. The role of estrogen in bone growth and maturation during childhood and adolescence. The Journal of steroid biochemistry and molecular biology 1997;61:141-4.
[22] Mauras N, Rogol AD, Haymond MW, Veldhuis JD. Sex steroids, growth hormone, insulin-like growth factor-1: neuroendocrine and metabolic regulation in puberty. Hormone research 1996;45:74-80.
[23] Lombardi G, Di Somma C, Rubino M, Faggiano A, Vuolo L, Guerra E, et al. The roles of parathyroid hormone in bone remodeling: prospects for novel therapeutics. Journal of endocrinological investigation 2011;34:18-22.
[24] Carter PH, Schipani E. The roles of parathyroid hormone and calcitonin in bone remodeling: prospects for novel therapeutics. Endocrine, metabolic & immune disorders drug targets 2006;6:59-76.
[25] Kohli SS, Kohli VS. Role of RANKL–RANK/osteoprotegerin molecular complex in bone remodeling and its immunopathologic implications. Indian Journal of Endocrinology and Metabolism 2011;15:175-81.
[26] Ratner BD HA, Schoen FJ, Lemons JE. . Biomaterials Science: An Introduction to Materials in Medicine. 2nd ed. San Diego, CA, USA: Elsevier Academic Press; 2004.
[27] Albrektsson T, Brånemark PI, Hansson HA, Lindström J. Osseointegrated Titanium Implants: Requirements for Ensuring a Long-Lasting, Direct Bone-to-Implant Anchorage in Man. Acta Orthopaedica Scandinavica 1981;52:155-70.
[28] Adell R, Lekholm U, Rockler B, Branemark PI. A 15-year study of osseointegrated implants in the treatment of the edentulous jaw. International journal of oral surgery 1981;10:387-416.
[29] Branemark PI, Adell R, Albrektsson T, Lekholm U, Lundkvist S, Rockler B. Osseointegrated titanium fixtures in the treatment of edentulousness. Biomaterials 1983;4:25-8.
[30] Hallab NJ, Jacobs JJ. Biologic effects of implant debris. Bulletin of the NYU hospital for joint diseases 2009;67:182-8.
[31] Portan DV, Kroustalli AA, Deligianni DD, Papanicolaou GC. On the biocompatibility between TiO2 nanotubes layer and human osteoblasts. Journal of biomedical materials research Part A 2012;100:2546-53.
[32] Nemir S, West JL. Synthetic materials in the study of cell response to substrate rigidity. Annals of biomedical engineering 2010;38:2-20.
[33] Yeung T, Georges PC, Flanagan LA, Marg B, Ortiz M, Funaki M, et al. Effects of substrate stiffness on cell morphology, cytoskeletal structure, and adhesion. Cell motility and the cytoskeleton 2005;60:24-34.
[34] Chen JC, Jacobs CR. Mechanically induced osteogenic lineage commitment of stem cells. Stem cell research & therapy 2013;4:107.

[35] Takai E, Costa KD, Shaheen A, Hung CT, Guo XE. Osteoblast elastic modulus measured by atomic force microscopy is substrate dependent. Annals of biomedical engineering 2005;33:963-71.
[36] Minagar S, Wang J, Berndt CC, Ivanova EP, Wen C. Cell response of anodized nanotubes on titanium and titanium alloys. Journal of biomedical materials research Part A 2013;101:2726-39.
[37] Webster TJ, Ejiofor JU. Increased osteoblast adhesion on nanophase metals: Ti, Ti6Al4V, and CoCrMo. Biomaterials 2004;25:4731-9.
[38] Webster TJ, Ergun C, Doremus RH, Siegel RW, Bizios R. Enhanced functions of osteoblasts on nanophase ceramics. Biomaterials 2000;21:1803-10.
[39] Colon G, Ward BC, Webster TJ. Increased osteoblast and decreased Staphylococcus epidermidis functions on nanophase ZnO and TiO2. Journal of biomedical materials research Part A 2006;78:595-604.
[40] Ward BC, Webster TJ. The effect of nanotopography on calcium and phosphorus deposition on metallic materials in vitro. Biomaterials 2006;27:3064-74.
[41] Gutwein LG, Webster TJ. Increased viable osteoblast density in the presence of nanophase compared to conventional alumina and titania particles. Biomaterials 2004;25:4175-83.
[42] Wimmers Ferreira MR, Rodrigo Fernandes R, Freire Assis A, Dernowsek JA, Passos GA, Variola F, et al. Oxidative Nanopatterning of Titanium Surface Influences mRNA and MicroRNA Expression in Human Alveolar Bone Osteoblastic Cells. International journal of biomaterials 2016;2016:9169371.
[43] de Oliveira PT, Nanci A. Nanotexturing of titanium-based surfaces upregulates expression of bone sialoprotein and osteopontin by cultured osteogenic cells. Biomaterials 2004;25:403-13.
[44] Variola F, Yi JH, Richert L, Wuest JD, Rosei F, Nanci A. Tailoring the surface properties of Ti6Al4V by controlled chemical oxidation. Biomaterials 2008;29:1285-98.
[45] Su Y, Komasa S, Sekino T, Nishizaki H, Okazaki J. Nanostructured Ti6Al4V alloy fabricated using modified alkali-heat treatment: Characterization and cell adhesion. Materials science & engineering C, Materials for biological applications 2016;59:617-23.
[46] Palmquist A, Johansson A, Suska F, Branemark R, Thomsen P. Acute inflammatory response to laser-induced micro- and nano-sized titanium surface features. Clinical implant dentistry and related research 2013;15:96-104.
[47] Xing H, Komasa S, Taguchi Y, Sekino T, Okazaki J. Osteogenic activity of titanium surfaces with nanonetwork structures. International journal of nanomedicine 2014;9:1741-55.
[48] Rani VV, Vinoth-Kumar L, Anitha VC, Manzoor K, Deepthy M, Shantikumar VN. Osteointegration of titanium implant is sensitive to specific nanostructure morphology. Acta biomaterialia 2012;8:1976-89.
[49] Brammer KS, Frandsen CJ, Jin S. TiO2 nanotubes for bone regeneration. Trends in biotechnology 2012;30:315-22.
[50] Gong D, Grimes CA, Varghese OK, Hu W, Singh RS, Chen Z, et al. Titanium oxide nanotube arrays prepared by anodic oxidation. Journal of Materials Research 2001;16:3331-4.

[51] Sturgeon MR, Lai P, Hu MZ. A comparative study of anodized titania nanotube architectures in aqueous and nonaqueous solutions. Journal of Materials Research 2011;26:2612-23.
[52] Patel SB, Hamlekhan A, Royhman D, Butt A, Yuan J, Shokuhfar T, et al. Enhancing surface characteristics of Ti-6Al-4V for bio-implants using integrated anodization and thermal oxidation. Journal of Materials Chemistry B 2014;2:3597-608.
[53] Wang J, Lin Z. Anodic Formation of Ordered TiO2 Nanotube Arrays: Effects of Electrolyte Temperature and Anodization Potential. The Journal of Physical Chemistry C 2009;113:4026-30.
[54] Li X, Chen T, Hu J, Li S, Zou Q, Li Y, et al. Modified surface morphology of a novel Ti-24Nb-4Zr-7.9Sn titanium alloy via anodic oxidation for enhanced interfacial biocompatibility and osseointegration. Colloids and surfaces B, Biointerfaces 2016;144:265-75.
[55] Kim EJ, Jeong YH, Kang BA, Choe HC. Nanotubular Structure on the Ti-29Nb-5Zr Alloy by Scanning Transmission Electron Microscope. Journal of nanoscience and nanotechnology 2015;15:595-9.
[56] Verissimo NC, Geilich BM, Oliveira HG, Caram R, Webster TJ. Reducing Staphylococcus aureus growth on Ti alloy nanostructured surfaces through the addition of Sn. Journal of biomedical materials research Part A 2015;103:3757-63.
[57] Kim HJ, Choe HC. Electrochemical and sputtering deposition of hydroxyapatite film on nanotubular Ti-25Ta-xZr alloys. Journal of nanoscience and nanotechnology 2014;14:8405-10.
[58] Li B, Hao J, Min Y, Xin S, Guo L, He F, et al. Biological properties of nanostructured Ti incorporated with Ca, P and Ag by electrochemical method. Materials science & engineering C, Materials for biological applications 2015;51:80-6.
[59] Shokuhfar T, Sinha-Ray S, Sukotjo C, Yarin AL. Intercalation of anti-inflammatory drug molecules within TiO 2 nanotubes. RSC Advances 2013;3:17380-6.
[60] Mohan L, Anandan C, Rajendran N. Drug release characteristics of quercetin-loaded TiO nanotubes coated with chitosan. International journal of biological macromolecules 2016.
[61] Balasundaram G, Yao C, Webster TJ. TiO2 nanotubes functionalized with regions of bone morphogenetic protein-2 increases osteoblast adhesion. Journal of biomedical materials research Part A 2008;84:447-53.
[62] Cheng H, Li Y, Huo K, Gao B, Xiong W. Long-lasting in vivo and in vitro antibacterial ability of nanostructured titania coating incorporated with silver nanoparticles. Journal of biomedical materials research Part A 2014;102:3488-99.
[63] Vasilev K, Poh Z, Kant K, Chan J, Michelmore A, Losic D. Tailoring the surface functionalities of titania nanotube arrays. Biomaterials 2010;31:532-40.
[64] Park J, Bauer S, Schlegel KA, Neukam FW, von der Mark K, Schmuki P. TiO2 nanotube surfaces: 15 nm--an optimal length scale of surface topography for cell adhesion and differentiation. Small 2009;5:666-71.
[65] Park J, Bauer S, von der Mark K, Schmuki P. Nanosize and vitality: TiO2 nanotube diameter directs cell fate. Nano letters 2007;7:1686-91.

[66] Oh S, Brammer KS, Li YS, Teng D, Engler AJ, Chien S, et al. Stem cell fate dictated solely by altered nanotube dimension. Proceedings of the National Academy of Sciences of the United States of America 2009;106:2130-5.
[67] Ge J, Guo L, Wang S, Zhang Y, Cai T, Zhao RC, et al. The size of mesenchymal stem cells is a significant cause of vascular obstructions and stroke. Stem cell reviews 2014;10:295-303.
[68] Popat KC, Leoni L, Grimes CA, Desai TA. Influence of engineered titania nanotubular surfaces on bone cells. Biomaterials 2007;28:3188-97.
[69] Das K, Bose S, Bandyopadhyay A. TiO2 nanotubes on Ti: Influence of nanoscale morphology on bone cell-materials interaction. Journal of biomedical materials research Part A 2009;90:225-37.
[70] Yu WQ, Jiang XQ, Zhang FQ, Xu L. The effect of anatase TiO2 nanotube layers on MC3T3-E1 preosteoblast adhesion, proliferation, and differentiation. Journal of biomedical materials research Part A 2010;94:1012-22.
[71] Zhang R, Wu H, Ni J, Zhao C, Chen Y, Zheng C, et al. Guided proliferation and bone-forming functionality on highly ordered large diameter TiO2 nanotube arrays. Materials science & engineering C, Materials for biological applications 2015;53:272-9.
[72] Fan X, Feng B, Liu Z, Tan J, Zhi W, Lu X, et al. Fabrication of TiO2 nanotubes on porous titanium scaffold and biocompatibility evaluation in vitro and in vivo. Journal of biomedical materials research Part A 2012;100:3422-7.
[73] Shin DH, Shokuhfar T, Choi CK, Lee SH, Friedrich C. Wettability changes of TiO2 nanotube surfaces. Nanotechnology 2011;22:315704.
[74] Shokuhfar T, Hamlekhan A, Chang JY, Choi CK, Sukotjo C, Friedrich C. Biophysical evaluation of cells on nanotubular surfaces: the effects of atomic ordering and chemistry. International journal of nanomedicine 2014;9:3737-48.
[75] Hamlekhan A, Butt A, Patel S, Royhman D, Takoudis C, Sukotjo C, et al. Fabrication of anti-aging TiO2 nanotubes on biomedical Ti alloys. PloS one 2014;9:e96213.
[76] Oh S, Daraio C, Chen LH, Pisanic TR, Finones RR, Jin S. Significantly accelerated osteoblast cell growth on aligned TiO2 nanotubes. Journal of biomedical materials research Part A 2006;78:97-103.
[77] Oh S, Jin S. Titanium oxide nanotubes with controlled morphology for enhanced bone growth. Materials Science and Engineering: C 2006;26:1301-6.
[78] Brammer KS, Oh S, Cobb CJ, Bjursten LM, van der Heyde H, Jin S. Improved bone-forming functionality on diameter-controlled TiO(2) nanotube surface. Acta biomaterialia 2009;5:3215-23.
[79] Kim JH, Cho KP, Chung YS, Kim OS, Chung SS, Lee KK, et al. The effect of nanotubular titanium surfaces on osteoblast differentiation. Journal of nanoscience and nanotechnology 2010;10:3581-5.
[80] Yang JS, Vang MS, Uhm SW, Chung YS, Lee KK, Lee DJ, et al. Response of fetal rat calvarial cells to nanotubular titanium oxide surface. Journal of nanoscience and nanotechnology 2011;11:1807-10.
[81] Zhao L, Mei S, Chu PK, Zhang Y, Wu Z. The influence of hierarchical hybrid micro/nano-textured titanium surface with titania nanotubes on osteoblast functions. Biomaterials 2010;31:5072-82.

[82] Filova E, Fojt J, Kryslova M, Moravec H, Joska L, Bacakova L. The diameter of nanotubes formed on Ti-6Al-4V alloy controls the adhesion and differentiation of Saos-2 cells. International journal of nanomedicine 2015;10:7145-63.
[83] Pozio A, Palmieri A, Girardi A, Cura F, Carinci F. Titanium nanotubes activate genes related to bone formation in vitro. Dental research journal 2012;9:S164-8.
[84] Ercan B, Taylor E, Alpaslan E, Webster TJ. Diameter of titanium nanotubes influences anti-bacterial efficacy. Nanotechnology 2011;22:295102.
[85] Sul YT. Electrochemical growth behavior, surface properties, and enhanced in vivo bone response of TiO2 nanotubes on microstructured surfaces of blasted, screw-shaped titanium implants. International journal of nanomedicine 2010;5:87-100.
[86] Bjursten LM, Rasmusson L, Oh S, Smith GC, Brammer KS, Jin S. Titanium dioxide nanotubes enhance bone bonding in vivo. Journal of biomedical materials research Part A 2010;92:1218-24.
[87] Wang N, Li H, Lu W, Li J, Wang J, Zhang Z, et al. Effects of TiO2 nanotubes with different diameters on gene expression and osseointegration of implants in minipigs. Biomaterials 2011;32:6900-11.
[88] von Wilmowsky C, Bauer S, Lutz R, Meisel M, Neukam FW, Toyoshima T, et al. In vivo evaluation of anodic TiO2 nanotubes: an experimental study in the pig. Journal of biomedical materials research Part B, Applied biomaterials 2009;89:165-71.
[89] von Wilmowsky C, Bauer S, Roedl S, Neukam FW, Schmuki P, Schlegel KA. The diameter of anodic TiO2 nanotubes affects bone formation and correlates with the bone morphogenetic protein-2 expression in vivo. Clinical oral implants research 2012;23:359-66.
[90] Fadeeva E SS, Koch J, Chichkov BN. Surface and Interfacial Aspects of Cell Adhesion. Boca Raton, FL, USA: CRC Press, Taylor & Fracis Group; 2010.
[91] Lehnert D, Wehrle-Haller B, David C, Weiland U, Ballestrem C, Imhof BA, et al. Cell behaviour on micropatterned substrata: limits of extracellular matrix geometry for spreading and adhesion. Journal of cell science 2004;117:41-52.
[92] Livak KJ, Schmittgen TD. Analysis of relative gene expression data using real-time quantitative PCR and the 2(-Delta Delta C(T)) Method. Methods (San Diego, Calif) 2001;25:402-8.
[93] El-Amin SF, Lu HH, Khan Y, Burems J, Mitchell J, Tuan RS, et al. Extracellular matrix production by human osteoblasts cultured on biodegradable polymers applicable for tissue engineering. Biomaterials 2003;24:1213-21.
[94] Liu X, Zhou X, Li S, Lai R, Zhou Z, Zhang Y, et al. Effects of titania nanotubes with or without bovine serum albumin loaded on human gingival fibroblasts. International journal of nanomedicine 2014;9:1185-98.
[95] Pozio A, Palmieri A, Girardi A, Cura F, Carinci F. Titanium nanotubes stimulate osteoblast differentiation of stem cells from pulp and adipose tissue. Dental research journal 2012;9:S169-74.
[96] Gupta A, Liberati TA, Verhulst SJ, Main BJ, Roberts MH, Potty AG, et al. Biocompatibility of single-walled carbon nanotube composites for bone regeneration. Bone & joint research 2015;4:70-7.

[97] Pauly S, Back DA, Kaeppler K, Haas NP, Schmidmaier G, Wildemann B. Influence of statins locally applied from orthopedic implants on osseous integration. BMC musculoskeletal disorders 2012;13:208.
[98] Virdi AS, Irish J, Sena K, Liu M, Ke HZ, McNulty MA, et al. Sclerostin antibody treatment improves implant fixation in a model of severe osteoporosis. The Journal of bone and joint surgery American volume 2015;97:133-40.
[99] Back DA, Pauly S, Rommel L, Haas NP, Schmidmaier G, Wildemann B, et al. Effect of local zoledronate on implant osseointegration in a rat model. BMC musculoskeletal disorders 2012;13:42.
[100] Betoni W, Jr., Queiroz TP, Luvizuto ER, Valentini-Neto R, Garcia-Junior IR, Bernabe PF. Evaluation of centrifuged bone marrow on bone regeneration around implants in rabbit tibia. Implant dentistry 2012;21:481-5.
[101] Freire AR, Rossi AC, Queiroz TP, Gulinelli JL, Souza FA, Margonar R, et al. Histometric analysis of bone repair in bone-implant interface using a polylactic/polyglycolic acid copolymer associated with implants in rabbit tibia. The Journal of oral implantology 2012;38 Spec No:449-57.
[102] Nich C, Marchadier A, Sedel L, Petite H, Vidal C, Hamadouche M. Decrease in particle-induced osteolysis in ovariectomized mice. Journal of orthopaedic research : official publication of the Orthopaedic Research Society 2010;28:178-83.
[103] Wang JX, Fan YB, Gao Y, Hu QH, Wang TC. TiO2 nanoparticles translocation and potential toxicological effect in rats after intraarticular injection. Biomaterials 2009;30:4590-600.
[104] Bayat N, Lopes VR, Scholermann J, Jensen LD, Cristobal S. Vascular toxicity of ultra-small TiO2 nanoparticles and single walled carbon nanotubes in vitro and in vivo. Biomaterials 2015;63:1-13.
[105] Ames BN, Lee FD, Durston WE. An improved bacterial test system for the detection and classification of mutagens and carcinogens. Proceedings of the National Academy of Sciences of the United States of America 1973;70:782-6.
[106] Naya M, Kobayashi N, Ema M, Kasamoto S, Fukumuro M, Takami S, et al. In vivo genotoxicity study of titanium dioxide nanoparticles using comet assay following intratracheal instillation in rats. Regulatory toxicology and pharmacology : RTP 2012;62:1-6.
[107] Neacsu P, Mazare A, Cimpean A, Park J, Costache M, Schmuki P, et al. Reduced inflammatory activity of RAW 264.7 macrophages on titania nanotube modified Ti surface. The international journal of biochemistry & cell biology 2014;55:187-95.
[108] Ostberg AK, Dahlgren U, Sul YT, Johansson CB. Inflammatory cytokine release is affected by surface morphology and chemistry of titanium implants. Journal of materials science Materials in medicine 2015;26:155.
[109] Smith BS, Yoriya S, Grissom L, Grimes CA, Popat KC. Hemocompatibility of titania nanotube arrays. Journal of biomedical materials research Part A 2010;95:350-60.
[110] Bouxsein ML, Boyd SK, Christiansen BA, Guldberg RE, Jepsen KJ, Muller R. Guidelines for assessment of bone microstructure in rodents using micro-computed tomography. Journal of bone and mineral research : the official journal of the American Society for Bone and Mineral Research 2010;25:1468-86.

[111] Choi D, Yoon YS, Hwang D. Evaluation of sleeved implant fixation using a rat model. Medical engineering & physics 2011;33:310-4.
[112] Liu S, Broucek J, Virdi AS, Sumner DR. Limitations of using micro-computed tomography to predict bone-implant contact and mechanical fixation. Journal of microscopy 2012;245:34-42.
[113] Pauwels R, Jacobs R, Singer SR, Mupparapu M. CBCT-based bone quality assessment: are Hounsfield units applicable? Dentomaxillofacial Radiology 2015;44:20140238.
[114] Fajardo RJ, Cory E, Patel ND, Nazarian A, Laib A, Manoharan RK, et al. Specimen size and porosity can introduce error into microCT-based tissue mineral density measurements. Bone 2009;44:176-84.
[115] Dang Y, Zhang L, Song W, Chang B, Han T, Zhang Y, et al. In vivo osseointegration of Ti implants with a strontium-containing nanotubular coating. International journal of nanomedicine 2016;11:1003-11.
[116] Ban J, Kang S, Kim J, Lee K, Hyunpil L, Vang M, et al. MicroCT Analysis of Micro-Nano Titanium Implant Surface on the Osseointegration. Journal of nanoscience and nanotechnology 2015;15:172-5.
[117] Friedrich CR, Kolati M, Moser T, Sukotjo C, Shokuhfar T. Survivability of TiO2 nanotubes on the surface of bone screws. Surface Innovations 2014;2:60-8.
[118] Adami S, Zamberlan N. Adverse effects of bisphosphonates. A comparative review. Drug safety 1996;14:158-70.
[119] Kennel KA, Drake MT. Adverse Effects of Bisphosphonates: Implications for Osteoporosis Management. Mayo Clinic Proceedings 2009;84:632-8.
[120] Weinstein RS, Roberson PK, Manolagas SC. Giant Osteoclast Formation and Long-Term Oral Bisphosphonate Therapy. The New England journal of medicine 2009;360:53-62.
[121] Kumeria T, Mon H, Aw MS, Gulati K, Santos A, Griesser HJ, et al. Advanced biopolymer-coated drug-releasing titania nanotubes (TNTs) implants with simultaneously enhanced osteoblast adhesion and antibacterial properties. Colloids and surfaces B, Biointerfaces 2015;130:255-63.
[122] Gu YX, Du J, Zhao JM, Si MS, Mo JJ, Lai HC. Characterization and preosteoblastic behavior of hydroxyapatite-deposited nanotube surface of titanium prepared by anodization coupled with alternative immersion method. Journal of biomedical materials research Part B, Applied biomaterials 2012;100:2122-30.
[123] Gulati K, Aw MS, Losic D. Drug-eluting Ti wires with titania nanotube arrays for bone fixation and reduced bone infection. Nanoscale research letters 2011;6:571.
[124] Shokuhfar T, Sinha-Ray S, Sukotjo C, Yarin AL. Intercalation of anti-inflammatory drug molecules within TiO2 nanotubes. RSC Advances 2013;3:17380-6.
[125] Popat KC, Eltgroth M, LaTempa TJ, Grimes CA, Desai TA. Titania Nanotubes: A Novel Platform for Drug-Eluting Coatings for Medical Implants? Small 2007;3:1878-81.
[126] Hamlekhan A, Sinha-Ray S, Takoudis C, Mathew MT, Sukotjo C, Yarin AL, et al. Fabrication of drug eluting implants: study of drug release mechanism from titanium dioxide nanotubes. Journal of Physics D: Applied Physics 2015;48:275401.
[127] Jin Q, Giannobile WV. SDF-1 enhances wound healing of critical-sized calvarial defects beyond self-repair capacity. PloS one 2014;9:e97035.

[128] Sadir R, Baleux F, Grosdidier A, Imberty A, Lortat-Jacob H. Characterization of the stromal cell-derived factor-1alpha-heparin complex. The Journal of biological chemistry 2001;276:8288-96.
[129] Lee DW, Yun YP, Park K, Kim SE. Gentamicin and bone morphogenic protein-2 (BMP-2)-delivering heparinized-titanium implant with enhanced antibacterial activity and osteointegration. Bone 2012;50:974-82.
[130] Kim TH, Yun YP, Park YE, Lee SH, Yong W, Kundu J, et al. In vitro and in vivo evaluation of bone formation using solid freeform fabrication-based bone morphogenic protein-2 releasing PCL/PLGA scaffolds. Biomedical materials (Bristol, England) 2014;9:025008.
[131] Dick B, Schmidt KG, Eisenmann D, Pfeiffer N. A new method for direct detection of heparin on surface-modified intraocular lenses. A modification of Jaques' toluidine blue staining method. Ophthalmologica Journal international d'ophtalmologie International journal of ophthalmology Zeitschrift fur Augenheilkunde 1997;211:75-8.
[132] Kim SE, Song SH, Yun YP, Choi BJ, Kwon IK, Bae MS, et al. The effect of immobilization of heparin and bone morphogenic protein-2 (BMP-2) to titanium surfaces on inflammation and osteoblast function. Biomaterials 2011;32:366-73.
[133] Liu Y, Luo R, Shen F, Tang L, Wang J, Huang N. Construction of mussel-inspired coating via the direct reaction of catechol and polyethyleneimine for efficient heparin immobilization. Applied Surface Science 2015;328:163-9.
[134] Chen B, Li Y, Yang X, Xu H, Xie D. Zoledronic acid enhances bone-implant osseointegration more than alendronate and strontium ranelate in ovariectomized rats. Osteoporosis international : a journal established as result of cooperation between the European Foundation for Osteoporosis and the National Osteoporosis Foundation of the USA 2013;24:2115-21.
[135] Diefenbeck M, Muckley T, Zankovych S, Bossert J, Jandt KD, Schrader C, et al. Freezing of rat tibiae at -20 degrees c does not affect the mechanical properties of intramedullary bone/implant-interface: brief report. The open orthopaedics journal 2011;5:219-22.
[136] Ren W, Yang SY, Wooley PH. A novel murine model of orthopaedic wear-debris associated osteolysis. Scandinavian journal of rheumatology 2004;33:349-57.
[137] Zhao YP, Wei JL, Tian QY, Liu AT, Yi YS, Einhorn TA, et al. Progranulin suppresses titanium particle induced inflammatory osteolysis by targeting TNFalpha signaling. Scientific reports 2016;6:20909.
[138] Li N, Xu Z, Wooley PH, Zhang J, Yang SY. Therapeutic potentials of naringin on polymethylmethacrylate induced osteoclastogenesis and osteolysis, in vitro and in vivo assessments. Drug design, development and therapy 2014;8:1-11.
[139] Mao X, Pan X, Zhao S, Peng X, Cheng T, Zhang X. Protection against titanium particle-induced inflammatory osteolysis by the proteasome inhibitor bortezomib in vivo. Inflammation 2012;35:1378-91.
[140] Goncalves DM, Girard D. Titanium dioxide (TiO2) nanoparticles induce neutrophil influx and local production of several pro-inflammatory mediators in vivo. International immunopharmacology 2011;11:1109-15.

[141] Ma T, Ortiz SG, Huang Z, Ren P, Smith RL, Goodman SB. In vivo murine model of continuous intramedullary infusion of particles--a preliminary study. Journal of biomedical materials research Part B, Applied biomaterials 2009;88:250-3.
[142] Ma T, Huang Z, Ren PG, McCally R, Lindsey D, Smith RL, et al. An in vivo murine model of continuous intramedullary infusion of polyethylene particles. Biomaterials 2008;29:3738-42.
[143] Khalily C, Malkani AL, Hellman E, Voor MJ. Arthroplasty in the goat hip. Journal of investigative surgery : the official journal of the Academy of Surgical Research 1997;10:119-23.
[144] Harboe K, Enoksen CH, Gjerdet NR, Sudmann E. Development of a femoral stem providing strong anchorage and facilitated removal. An experimental study in goats. Veterinary and comparative orthopaedics and traumatology : VCOT 2012;25:95-101.
[145] Harboe K, Gjerdet NR, Sudmann E, Indrekvam K, Soreide K. Assessment of retention force and bone apposition in two differently coated femoral stems after 6 months of loading in a goat model. Journal of orthopaedic surgery and research 2014;9:69.
[146] Harboe K, Ellingsen CL, Sudmann E, Gjerdet NR, Soreide K, Indrekvam K. Can bone apposition predict the retention force of a femoral stem? An experimental weight-bearing hip-implant model in goats. BMC musculoskeletal disorders 2015;16:102.
[147] MJ dW. Early Features of the Bone-Implant Interface in Hip Arthroplasty. A Comparative Study in the Proximal Femur of the Goat after Implantation of a Cemented versus an Uncemented Endoprosthesis.: Catholic University of Nijmegen; 1988.
[148] Roszek B, Weinans H, van Loon P, Huiskes R. In vivo measurements of the loading conditions on the tibia of the goat. Acta anatomica 1993;146:188-92.
[149] Weinans H, Blankevoort L. Reconstruction of bone loading conditions from in vivo strain measurements. Journal of biomechanics 1995;28:739-44.